UNIVERSIDADE ESTADUAL DE CAMPINAS
Instituto de Física “Gleb Wataghin”

Paulo Felipe Jarschel de Siqueira

Erbium-Doped Aluminum-Oxide Films for Integrated Photonics

Filmes de Óxido de Alumínio dopados com Érbio para Fotônica Integrada

Campinas
2018

Paulo Felipe Jarschel de Siqueira

Erbium-Doped Aluminum-Oxide Films for Integrated Photonics

Filmes de Óxido de Alumínio dopados com Érbio para Fotônica Integrada

Thesis presented to the
Institute of Physics Gleb Wataghin
of the University of Campinas
in partial fulfillment of the requirements
for the degree of Doctor in sciences

Tese apresentada ao
Instituto de Física Gleb Wataghin
da Universidade Estadual de Campinas
como parte dos requisitos exigidos para a
obtenção do título de Doutor em ciências

Supervisor (Orientador): Newton Cesario Frateschi

ESTE EXEMPLAR CORRESPONDE À VERSÃO FINAL DA TESE DEFENDIDA PELO ALUNO PAULO FELIPE JARSCHEL DE SIQUEIRA E ORIENTADA PELO PROF. DR. NEWTON CESARIO FRATESCHI.

Campinas
2018

Agência(s) de fomento e nº(s) de processo(s): CNPq, 143212/2009-5
ORCID: http://orcid.org/0000-0001-9926-5284

Ficha catalográfica
Universidade Estadual de Campinas
Biblioteca do Instituto de Física Gleb Wataghin
Lucimeire de Oliveira Silva da Rocha - CRB 8/9174

J296e

Jarschel, Paulo Felipe, 1985-
Erbium-doped aluminum-oxide films for integrated photonics / Paulo Felipe Jarschel de Siqueira. – Campinas, SP : [s.n.], 2018.

Orientador: Newton Cesário Frateschi.
Tese (doutorado) – Universidade Estadual de Campinas, Instituto de Física Gleb Wataghin.

1. Fotônica. 2. Silício. 3. Érbio. 4. Microressonadores (Optoeletrônica). 5. Lasers. I. Frateschi, Newton Cesário, 1962-. II. Universidade Estadual de Campinas. Instituto de Física Gleb Wataghin. III. Título.

Informações para Biblioteca Digital

Título em outro idioma: Filmes de óxido de alumínio dopados com érbio para fotônica integrada
Palavras-chave em inglês:
Photonics
Silicon
Erbium
Microresonators (Optoelectronics)
Lasers
Área de concentração: Física
Titulação: Doutor em Ciências
Banca examinadora:
Newton Cesário Frateschi [Orientador]
Lucas Heitzmann Gabrielli
Leandro Russovski Tessler
Eric Alberto de Mello Fagotto
Ivan Aritz Aldaya Garde
Data de defesa: 28-09-2018
Programa de Pós-Graduação: Física

MEMBROS DA COMISSÃO JULGADORA DA TESE DE DOUTORADO DE **PAULO FELIPE JARSCHEL DE SIQUEIRA** RA: **024821** APRESENTADA E APROVADA AO INSTITUTO DE FÍSICA "GLEB WATAGHIN", DA UNIVERSIDADE ESTADUAL DE CAMPINAS, EM 28/09/2018.

COMISSÃO JULGADORA:

- Prof. Dr. Newton Cesario Frateschi - (Orientador) - IFGW/UNICAMP

- Prof. Dr. Lucas Heitzmann Gabrielli – FEEC/UNICAMP

- Prof. Dr. Leandro Russovski Tessler - IFGW/UNICAMP

- Prof. Dr. Eric Alberto de Mello Fagotto - PUC-CAMPINAS

- Prof. Dr. Ivan Aritz Aldaya Garde – UNESP – CÂMPUS SÃO JOÃO DA BOA VISTA

A Ata de Defesa, assinada pelos membros da Comissão Examinadora, consta no processo de vida acadêmica do aluno.

CAMPINAS

2018

"I stand in the sacred human presence. As I do now, so should you stand someday. I pray to your presence that this be so. The future remains uncertain and so it should, for it is the canvas upon which we paint our desires. Thus always the human condition faces a beautifully empty canvas. We possess only this moment in which to dedicate ourselves continuously to the sacred presence which we share and create."

> *– Jessica Atreides (Bene Gesserit Benediction), in "Children of Dune", by Frank Herbert (1976)*

Acknowledgements

First of all, I not only thank my family, but dedicate this thesis to them, who always supported me in an uncountable number of ways. During my first years in college, it was their (not only financial) support that kept me going and led me to where I stand today.

Going back to the past, I also want to thank Pedro Wiens, the principal of my high school back in 2000-2002. When I was accepted at both my hometown's Federal University (UFPR) and UNICAMP, he went to my house to congratulate me, and help me decide to which one I should go. He only asked me this: "Do you want to work as a teacher or a researcher?". And that was enough to make up my mind. I can't say my education would be any different if I stayed there, but that question was crucial for my decision.

Of course, I have to thank all my friends, especially the ones that I worked or shared a house with as well. All the adventures and odd situations (on which C_2H_6O may or may not have been involved) certainly created memories worthy of telling my future grandchildren about. But not only that, they always provided support when I needed, and inspiration when I didn't know I could use it. There are also those dear friends who were always there for me when I needed the most, that never let me give up when I thought I should, and always believed in me when I didn't think I could do something. You people know who you are, and to you, a very special "thank you" from the bottom of my heart!

On this same note, special thanks to my advisor for all of my academic life, Newton Frateschi, who also never stopped believing in me even after all of these years, and always supported me in so many ways! And also, special thanks to Antônio Augusto "Totó" von Zuben for the mentoring and help with the fabrication procedures during my early clean-room days. And also thank you both for, above all, being friends.

Yet another special acknowledgement to Hugo Fragnito and Paulo Dainese, who were always very understanding bosses, and from whom I learned a lot by working with.

FAPESP and CNPq have my gratitude for financing this work by providing funds for equipments, instruments and components purchasing, and also encouraging the participation on international conferences. This study was also financed in part by the Coordenação de Aperfeiçoamento de Pessoal de Nível Superior - Brasil (CAPES) - Finance Code 001, and Conselho Nacional de Desenvolvimento Científico e Tecnológico (CNPq), process number 143212-2009-05.

In short, to the many people who contributed directly and indirectly to this work, both staff from the university, professors, and also other students, my sincere gratitude!

Last, but not least, I want to thank Babi, Meg, Syd and Kiko, the cats who sometimes wake me up at night when fighting on the neighborhood rooftops.

Abstract

Aluminum Oxide (Al_2O_3), or alumina, is a material that possesses a very high potential for light amplification, due to the strong Erbium solubility. This work presents the study of applications of this material in integrated photonics, where optical amplification is an important research subject.

With a focus on silicon photonics, one of the building blocks currently used in integrated optical devices development, the ring resonator, presents two properties that encourage the investigation of optical amplification applied to it: an intrinsic trade-off between its quality factor and optical attenuation, and the resonant behavior, which could be equivalent to a longer amplifier. Differently from most approaches, the idea is to employ an Er-doped Al_2O_3 film as the top cladding of Si ring resonators fabricated at SOI Foundries with CMOS-compatible processes. To study this possibility, we begin with a review of the motivation for this research, and the basic theory needed to develop a model of the proposal. The next step is to develop a reliable fabrication procedure for the films, with a complete optical and surface characterization, including photoluminescence and atomic force microscopy measurements. When the films are applied to Si ring resonator samples, signal enhancement up to 2.6 dB and quality factor improvement of 25% have been measured, and the estimated loss reduction was higher than 3 dB. These results show that with this technique, high-Q and compact devices can be obtained, opening new application possibilities on Si photonics where several ring resonators can be concatenated with a greatly reduced net loss.

An additional study regarding the application of these films on III-V materials is also presented, where the compatibility between InGaAs/GaAs Quantum Well lasers and the fabrication procedures involved on the film fabrication is investigated. The obtained results show that the thermal annealing necessary for the Er emission optimization is in fact harmful for the epitaxial structure of III-V devices, but the damage

can be prevented by the application of a thermally resistant protective film. The developed Al_2O_3 film was found to be an excellent material for this end, enabling erbium-doped waveguides applications on III-V integrated photonics.

Resumo

O óxido de Alumínio (Al_2O_3), ou alumina, é um material que possui um grande potencial para amplificação óptica, devido à alta solubilidade do Érbio nesse meio. Este trabalho apresenta o estudo de aplicações desse material em fotônica integrada, onde amplificação óptica é um tópico de pesquisa importante.

Concentrando em Fotônica de Silício, um dos componentes atualmente utilizados no desenvolvimento de dispositivos ópticos integrados, o ressonador em anel, apresenta duas propriedades que encorajam a investigação da amplificação óptica aplicada no mesmo: a relação de troca intrínsica entre o seu fator de qualidade e atenuação óptica, e o comportamento ressonante, que poderia ser equivalente a um amplificador mais longo. Diferentemente da maioria das abordagens, a ideia é empregar um filme de Al_2O_3 dopado com Er como o revestimento superior de anéis ressonadores de Si fabricados em SOI Foundries. Para estudar essa possibilidade, começamos com uma revisão da motivação para esta pesquisa e da teoria básica necessária para o desenvolvimento de um modelo que descreva a proposta. O próximo passo é o desenvolvimento de um método confiável de fabricação para os filmes, com caracterizações ópticas e da superfície completas, incluindo medidas de fotoluminescência e microscopia de força atômica. Quando aplicados em amostras de anéis ressonadores de Si, aumentos de 2.6 dB nos sinais e 25% nos fatores de qualidades foram medidos, e a redução da perda óptica foi estimada como mais de 3 dB. Estes resultados mostram que com essa técnica, altos fatores de qualidade e dispositivos compactos podem ser obtidos, abrindo novas possibilidades de aplicações em fotônica de Si, onde vários anéis ressonadores podem ser concatenados com uma perda total bastante reduzida.

Um estudo adicional com respeito à aplicação destes filmes em materiais III-V também é apresentado, onde a compatibilidade entre lasers de poço quântico de InGaAs/GaAs e os processos de fabricação envolvidos na obtenção do filme são

investigados. Os resultados obtidos mostram que o tratamento térmico necessário para a optimização da emissão do Er é de fato prejudicial para a estrutura epitaxial de dispositivos III-V, mas o dano pode se prevenido através da aplicação de um filme protetor resistente à temperatura. Foi concluído que o filme de Al_2O_3 desenvolvido é um excelente candidato para este fim, o que habilita aplicações de guias de onda dopados a érbio em fotônica integrada de materiais III-V.

Table of Contents

1. Introduction 14

1.1 Optical Communications 14

1.2 Domain Conversions and Integrated Photonics 18

1.3 Signal Amplification 21

1.4 Proposal 23

1.5 Thesis Organization 26

2. Theory 28

2.1 Erbium 28

2.2 Waveguides 31

2.3 Optical Amplification 41

2.4 Micro-resonators 45

2.5 Resonant Amplification 54

2.6 Chapter Summary 58

3. Erbium-Doped Al_2O_3 Films 59

3.1 Film Deposition and Characterization 59

3.2 Optical Characterization and Thermal Annealing 61

3.3 Chapter Summary 67

4. Silicon Ring Resonators with Er-Doped Al_2O_3 Cladding 68

4.1 Fabrication Process 68

4.2 Characterization 76

4.3 Loss Compensation 80

4.4 Designing Low-Loss Compact High-Q Devices 94

4.5 Chapter Summary 98

5. Er-doped Al2O3 Films for III-V integrated Photonics 100

5.1 Concept 100

5.2 Basic Semiconductor Laser Theory 102

5.3 Laser Design and Fabrication 107

5.4 Laser characterization 111

5.5 Chapter Summary 118

6. Conclusion 119

Publications 121

References 123

1. Introduction

This thesis presents the development of a novel method to reduce losses in integrated photonic devices, with direct benefits to telecommunications and optical data processing. Within this context, it is important to provide a brief background on this topic, to justify the motivation of the work from a broader perspective.

1.1 Optical Communications

Since the beginning of human history, civilizations searched for ways of communicating with other civilizations from great distances. From drums and smoke signals in early history, to light signals and the optical semaphore in the 17th century, it was only in the 18th century that a reliable long-distance communication system independent of weather and geography was created: The telegraph. This eventually led to the invention of the telephone by Alexander Graham Bell in 1876 [1]. While these two major inventions in telecommunications use electrical signals to transmit messages, there was another less known invention by Bell that uses light to not only send messages, but to also enable voice conversations: The Photophone. Light from the sun reaches a reflective membrane that vibrates according to the user's voice, turning it into a concave or convex mirror (Fig. 1.1a). This vibration modulates the light intensity that travels to a receiver where it is absorbed by a selenium cell, changing its electrical resistance (Fig. 1.1b). When electrical current passes through the device, it "inherits" the same information the light had, and can then induce an earphone to reproduce the sound.

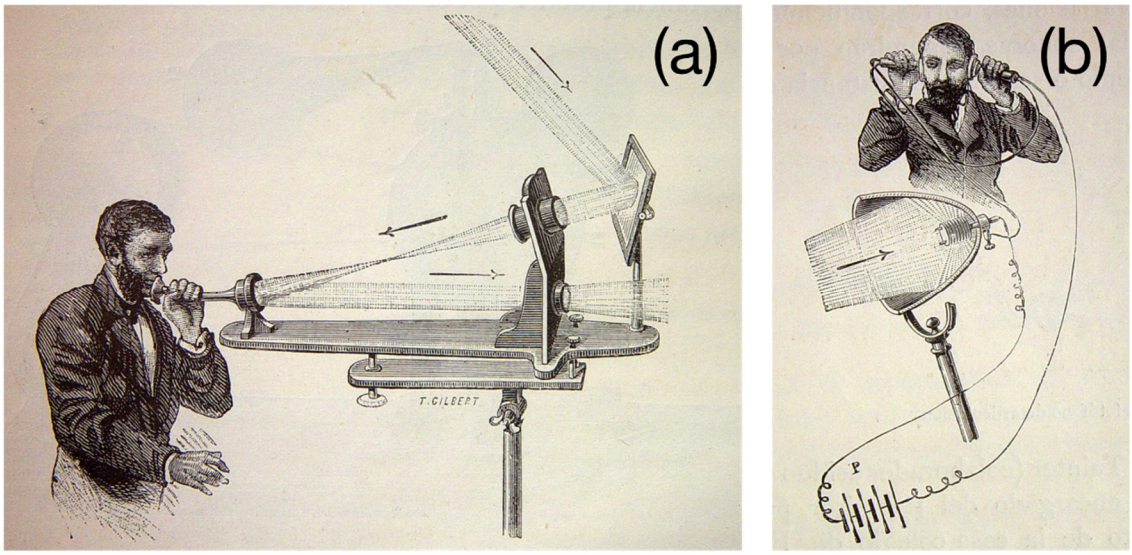

Image source: WikiMedia Commons/Public Domain

Fig. 1.1: Schematic of a Photophone transmitter (a) and receiver (b).

The Photophone was the first successful use of light and optics to transmit information to a long distance (219 m on the first tests, 11 km with further developments), creating the field of optical communications [2].

In the early 1840s, Daniel Colladon first demonstrated the concept of light being guided inside a curved medium, with his "Light Fountain". In 1870, John Tyndall described the phenomenon as caused by total internal reflection due to the refraction of light [3]. The concept was scarcely applied to imaging using glass rods, until in 1954 Harold Hopkins and Narinder Singh Kapany were able to transmit images in a bundle of 10000 optical fibers, over 75 cm [4]. The first use of optical fibers for data transmission was proposed by Manfred Borner in 1965, and, separately, Charles K. Kao and George A. Hockham envisioned that if the attenuation of the fibers could be reduced to less than 20 dB/km, the concept could be used for long-range communications [5]. From that point, development was constant and today optical fibers have a typical loss of 0.2 dB/km at the C-Band (1530 nm – 1560 nm), composing a communications network across the entire globe [6], as shown in Fig. 1.2.

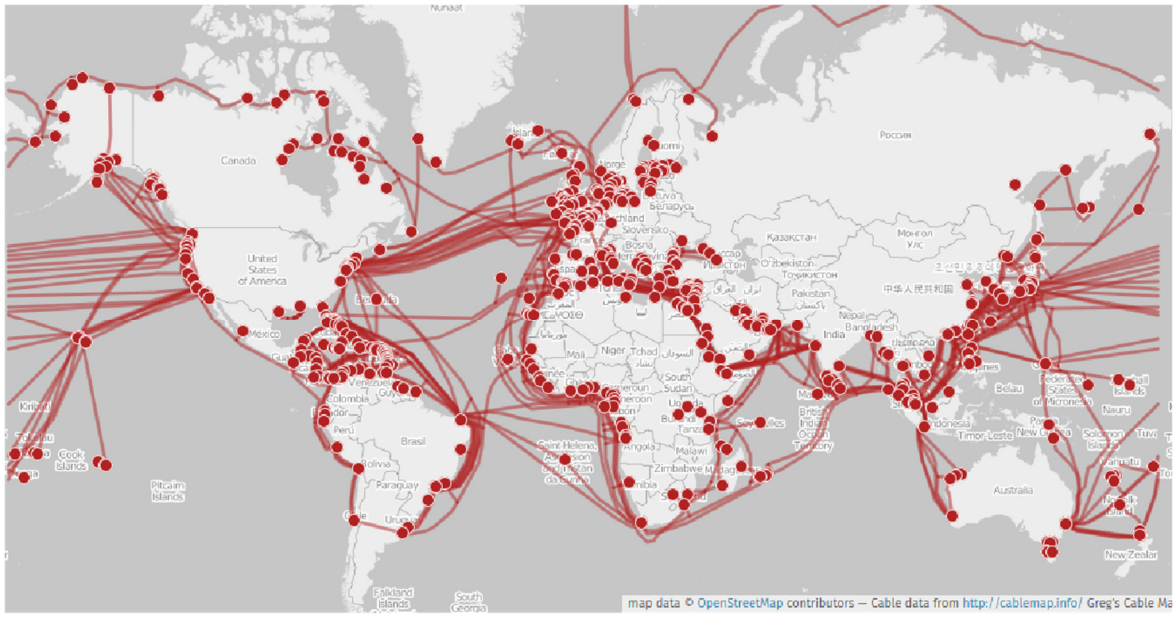

Fig. 1.2: Global Submarine Optical Fiber Network in 2015.

As technology evolved, with improvements ranging from the optical fiber fabrication techniques to data transmission protocols, so did the demand for fast communication networks. Fig. 1.3 shows a qualitative indication of internet demand versus the evolution of content, compared with the increase in infrastructure [7].

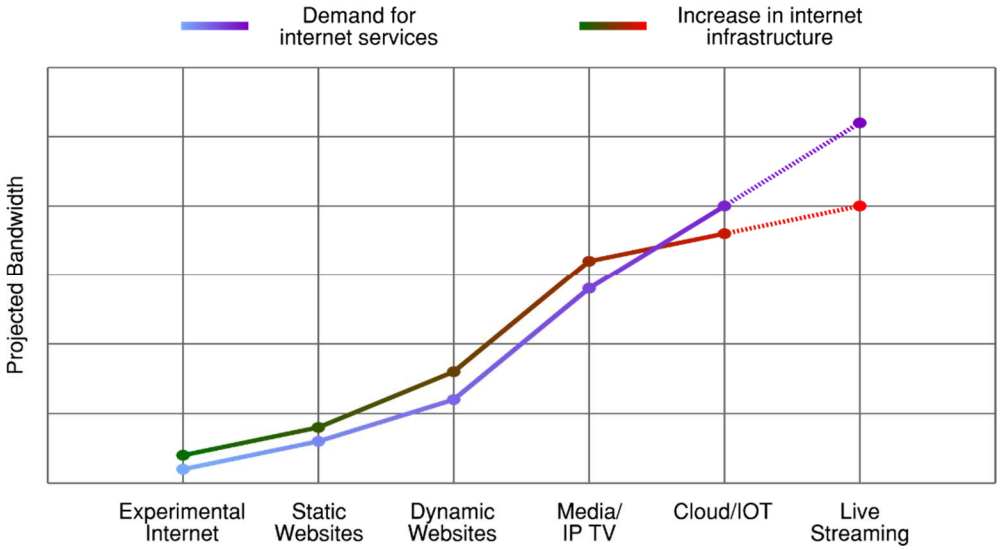

Fig. 1.3: Internet demand and infrastructure according to the type of content, derived from [7].

We can see that as internet content progressively uses more data and increases in size (bytes), the demand for faster connections also increases, causing the need for constant infrastructure improvement. With the recent advent of the “Internet of Things”,

multiple devices can be connected to the web in a single household, such as computers, smartphones, tablets, smartwatches, and appliances. Another recently created demand is the livestreaming, where people share live videos to possibly millions of subscribers. These new requirements can lead to a point where the increase in demand will surpass the infrastructure capability. So far, new technologies have been able to push this point further in time, as seen in Fig. 1.4 [8], which illustrates the evolution of the transmission capacity of optical systems in the last decades. One of these breakthroughs of particular interest to this work is the Erbium Doped Fiber Amplifier (EDFA), and section 1.3 details its importance and development.

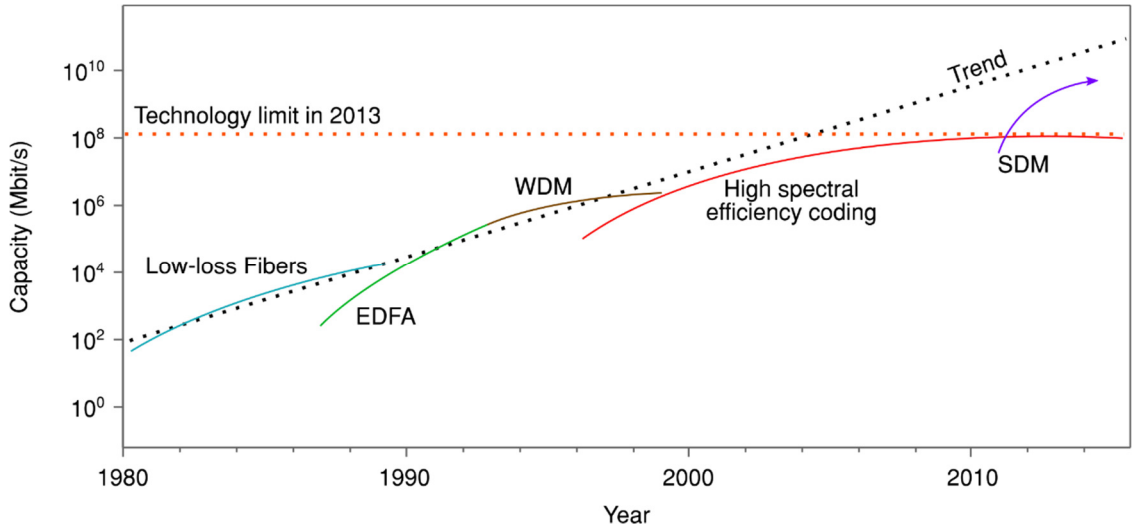

Fig. 1.4: Evolution of optical networks transmission capacity in time. New technologies are indicated, data from [8].

Similar to Moore's Law [9], where the number of transistors per square inch on an integrated circuit doubles every year, the optical network transmission capacity (per fiber) tends to increase tenfold every 4 years. To maintain this trend, the saturation in network capacity was always averted by new technologies, and we are currently reaching the point where innovations are not only desirable, but crucially necessary. Several research fields investigate this problem, and some of the most notable candidates for commercial applications are Spatial Division Multiplexing (SDM), in which multiple fiber propagation modes are used as different channels [8]; Hollow-Core Photonic

Bandgap Fibers, where light propagates in air instead of glass, mitigating undesirable nonlinear effects and reducing latency [10]; Multi-Core Fibers [11]; among others.

These methods to increase the single fiber transmission capacity have tremendous importance but are out of the scope of this work. Our contribution to the field of Optical Communications originates from another aspect of the problem.

1.2 Domain Conversions and Integrated Photonics

While optical fibers have been employed for longer-range data transmission, there are still many operations that are performed electronically on each "node" of the network. Routing, channel switching, and signal processing in general are examples of these operations. Also, in shorter-range data transmission, such as in large datacenters, this electronic processing is responsible for large energy consumption and harmful delays. Thus, methods of performing the same operations passively or actively in all-optical devices are desirable. One example where the benefit of avoiding domain conversions and electronic processing of signals was tremendous and unquestionable, was the adoption of Erbium Doped Fiber Amplifiers (EDFAs) in long-distance optical communication. Before the EDFAs, signal regeneration was performed at approximately every 100 km by converting the signal to the electronic domain, amplifying it electronically, and then converting it back to the optical domain. Besides being a very high-cost process (energy and equipment wise), it took a relatively long time and each wavelength channel had to be regenerated separately, limiting the bit rate at which data could be transferred to long distances. With the EDFA, it became possible to amplify light without the need for domain transductions. This not only reduced the cost of a high-speed link, but also allowed parallel processing of many channels at higher bit rate. One may say that this made modern Internet possible.

Within this context, aiming to reduce the number of optical/electronic domain conversions and taking advantage of the very mature CMOS technology,

particularly the silicon-on-insulator (SOI) device fabrication methods, the so-called Silicon Photonics field started to attract the interest of many scientists and engineers, and continues to evolve to this day [12]. Essentially, silicon photonics uses CMOS compatible processes to create structures for light confinement and guiding using silicon and silica, the latter being obtained by either oxidation or by a deposition process. Several integrated photonic devices have been proposed for optical processing, routing, and interconnections. Besides providing a platform for photonic data operation, this technology has also been employed to optically connect multiple cores of one microprocessor [13], minimizing power consumption, delay on data transfer and maximizing parallel computing potential. Essentially optical interconnection is moving towards shorter links. With the demand clearly growing, specialized silicon photonic foundries, using the same manufacturing techniques of standard Si chips, started to offer fabrication services, accelerating the development and reducing research costs.

One of the challenges in creating complete photonic circuits on a single chip is developing a telecommunication wavelength light source on Si, due to its indirect bandgap. Nevertheless, several possibilities have been demonstrated, such as III-V/Si wafer bonding, in which a III-V component is physically bonded to the Si substrate [14], and Er-doped silicon waveguides [15]. Also, it is important to observe that silicon and silica need to be transparent at the wavelength for which the photonic circuits are designed, at least for small power. Therefore, for a complete system one needs a different material for light detection or monitoring. The integration of germanium structures on Si has been widely used for this end. Its high compatibility with CMOS processes, the possibility of using wafer bonding, and the addition of Schottky metal-silicon (MS) structures contributed to a well-developed state of this technique [16].

To effectively create optical processing circuits on silicon, the first step is to develop its building blocks. Functional logical gates have already been reported with impressive performance (contrast of 20 dB, up to 40 Gb/s) based on photonic crystals

(PCs) [17] [18]. The problem with this approach is that PCs occupy large areas on the chip. Other possibilities, such as four-wave mixing in amorphous Si waveguides have been demonstrated at the cost of bitrate, reaching 1.25 Gb/s [19]. Another important development is light modulation on Si. From the first completely CMOS compatible Mach-Zehnder based intensity modulator with 6.5 dB of extinction ratio at 40 Gb/s [20], to current high-efficiency hybrid III-V/Si modulators with a contrast of more than 10 dB [21] [22], considerable progress has been made.

Structures based on ring resonators are versatile and relevant building blocks [23] [24]. It is a natural candidate for optical modulators [25] [26], and yet with many more other potential applications such as optical logical circuits, buffers, high-order filters, and weight banks for photonic neuromorphic computing [27] [28] [29] [30]. Ring resonators consist of a ring-shaped and a regular "bus" waveguide. Both are coupled via evanescent field, and due to the optical interference between light entering and exiting the ring, certain wavelengths remain "trapped" inside the ring, causing an immense increase in energy density and a characteristic notch transmission at each resonance, as seen in Fig. 1.5a and Fig. 1.5b (a detailed and quantitative description is given in section 2.4). If a second bus waveguide is placed on the other side of the ring, we obtain add/drop ports, that is, ports where a channel can be added or extracted from the main signal. This enables several applications, such as filters, switches and routers [24], as depicted in Fig. 1.5c. One difficulty in using this method to route signals on a chip is that a minimum insertion loss and attenuation will always be present. The problem exists due to a trade-off between the resonance sharpness (Q Factor) and the output power [31] [32]. This leads us to a typical problem present in optical communications: attenuation/loss.

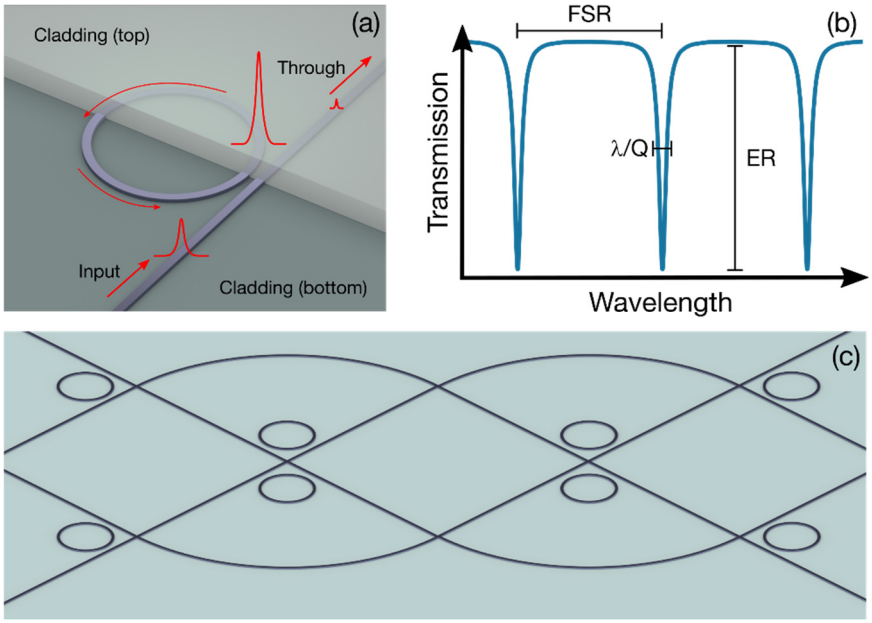

Fig. 1.5: (a) Schematic of a Ring Resonator and (b) its transmission spectrum. (c) Example of an optical switch based on ring resonators (c).

1.3 Signal Amplification

As light travels in a waveguide, the optical power decays due to absorption by the waveguide material, scattering, or poor confinement. In the previous section we mentioned that in the early days of the internet, an optical signal had to be electronically regenerated after a certain maximum length in a link. This regeneration consisted of channel separation, conversion to the electronic domain, subsequent amplification, reshaping, and modulation of a new laser source. This entire operation consumed a relatively high amount of energy, and the need of repeating the complete system for each channel raised the overall cost of network infrastructure [6].

In 1987, Mears *et al.* reported the first experimental high-gain EDFA, with 28 dB of gain over 3m of doped fiber, covering a bandwidth of 300 GHz [33]. Today, 30 years later, there are commercial fiber amplifiers with more than 40 dB of gain and, although the bandwidth of a single amplifier hasn't increased from 300GHz, it is possible to "tune" it to the C-Band (1530 nm - 1565 nm) or L-Band (1565 nm – 1625 nm),

spanning the entire optical communications range. It is possible to cover more bands by changing the doping element to Thulium, for example, to reach the 2 µm band [34].

The basic principle of the EDFA is stimulated emission by using optical pump to excite Erbium ions distributed within a SMF core. As the signal travels through the doped fiber, excited Er^{3+} ions decay to the fundamental state, emitting a photon with the same phase and polarization as one of the incoming photons. This is only possible due to the matching between Er^{3+} energy level differences and the usual C/L bands used for optical telecommunications. More on this subject can be found on sections 2.1 and 2.3. Considering the broadband nature of EDFA amplification, this device had a major role in overcoming the attenuation in optical networks, due to its relative lower cost compared to previous regeneration systems, and the possibility of amplifying multiple channels at once.

On the chip-level, it is not possible to use doped fibers to perform amplification. One natural idea would be to use semiconductor optical amplifiers (SOAs), due to its small footprint and the use of semiconductor materials. The main problem with this, however, is the small lifetime of the excited carriers which distorts pulses, and the high spontaneous emission rate which increases the noise. Both effects lead to loss of information. Even though this issue has been mitigated with recent improvements, it is still not suitable for optical communications in general [35].

Another, more interesting approach is to try and mimic the EDFA benefits on the chip. To that end, Erbium Doped Waveguide Amplifiers (EDWAs) have been proposed and demonstrated, reaching gains as high as 20 dB, along only 12.9 cm [36] [37] [38]. This particular example is schematized in Fig. 1.6. The most commonly used material as the waveguide core in this application is aluminum oxide (Al_2O_3, also referred to as alumina), due to the relatively high refractive index and high Er^{3+} solubility [39]. However, there are many developments using different materials, such as organic composites, silicon sub-oxides (SiO_x), silicon nitride (Si_3N_4), among others [40] [41].

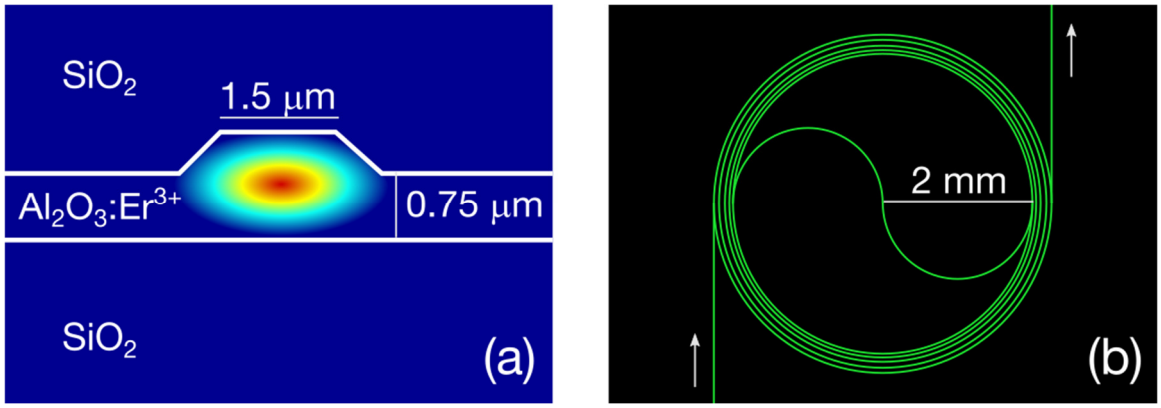

Fig. 1.6: Example of EDWA, with 20 dB of gain in 12.9 cm [38]. (a) Schematic of the waveguide geometry, with the fundamental mode of propagation shown. (b) Spiral amplifier illustration.

One challenge faced by EDWAs is that the core material tends to be different from Silicon. Therefore, these EDWAs do not benefit from the well-established CMOS processes, and several postprocessing steps are required to fabricate amplifiers on standard Si chips [42], increasing chip design time and often reducing yield. A different technique to achieve similar results, is to use the waveguide top cladding as the gain media by depositing the doped material on top of the chip. Amplifiers and lasers have been proposed with this method, using electrically pumped Erbium-doped SiO_2 as cladding of a slot waveguide [43] [44]. Organic materials can also be used for lasing in Si in this manner, using a Bragg cavity and dyes instead of Erbium [45].

In this context, the main subject of this thesis is the study and demonstration of a novel method of loss reduction, using the concept of creating a gain media in the cladding.

1.4 Proposal

Since Al_2O_3 has a strong potential for amplification and lasing applications in integrated photonics, we are going to study and demonstrate the implementation of such materials on photonic chips in two distinct fronts. First, we propose, model, and experimentally demonstrate a novel type of loss reduction in silicon photonics devices based on ring resonators. Second, we investigate the possibility of using alumina in

conjunction with III-V materials, with the goal of developing an integrated monolithic EDWA. This study is presented as an appendix.

In silicon photonics, one of the main building blocks is the ring resonator. However, when used for filtering or routing, the trade-off between filtering/routing capability (Q Factor) and insertion loss can limit the applications [31] [32]. A ring resonator schematic and a qualitative illustration of this trade-off are shown in Fig. 1.7. Typical attenuations of 0.5 dB may not be seen as cause for concern, but when several of these devices need to be concatenated, as shown in Fig. 1.5c, the output signal may be weak enough to warrant the need for amplification.

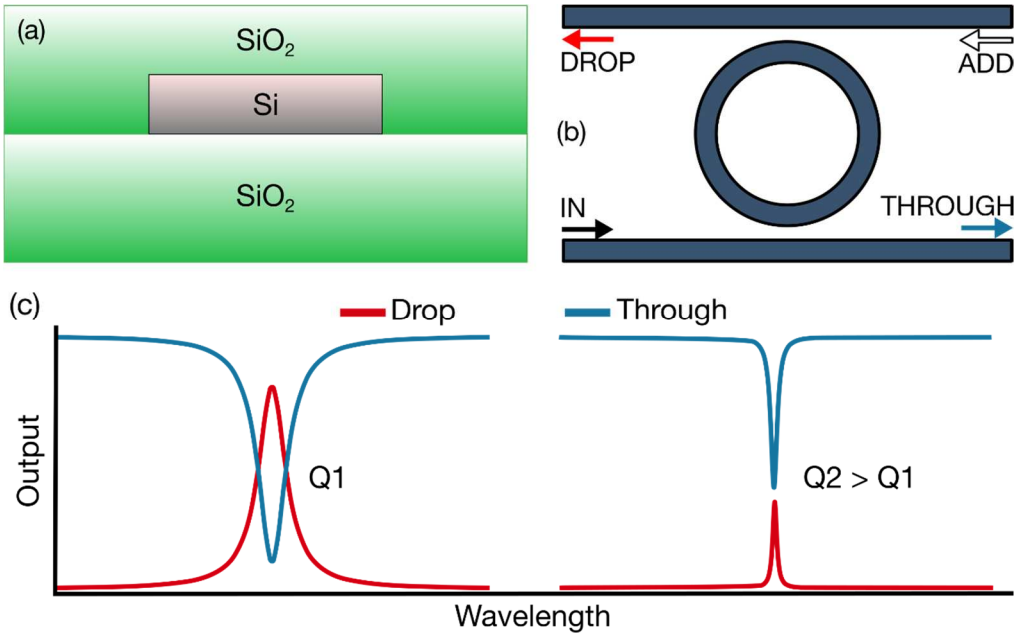

Fig. 1.7: (a) Layers composing a standard ring resonator waveguide. (b) Schematic of a ring resonator with all ports indicated. (c) Illustration of the trade-off between Q factor and drop port power.

On one hand, relying on external devices to restore the signal can be costly and impractical, and depending on the application, impossible. On the other hand, although standard EDWAs are relatively small, the required chip area may not be available in an integrated photonic circuit. Eliminating this small loss from each of these components would then be the ideal solution. Higher quality fabrication processes are currently available [46], that could minimize the scattering losses of the waveguide, but

at the same time would increase the cost and reduce the potential for production scalability. However, if we combine the concept of Erbium-doped claddings with the resonant nature of a ring resonator, the result will be a compact CMOS-compatible gain medium coexisting with the filtering/routing element, with no additional chip area required. It will be demonstrated that this proposed method, depicted in Fig. 1.8, has the potential to eliminate insertion losses of ring resonator-based devices, and under optimal conditions, the complete device can be employed as an integrated amplifier.

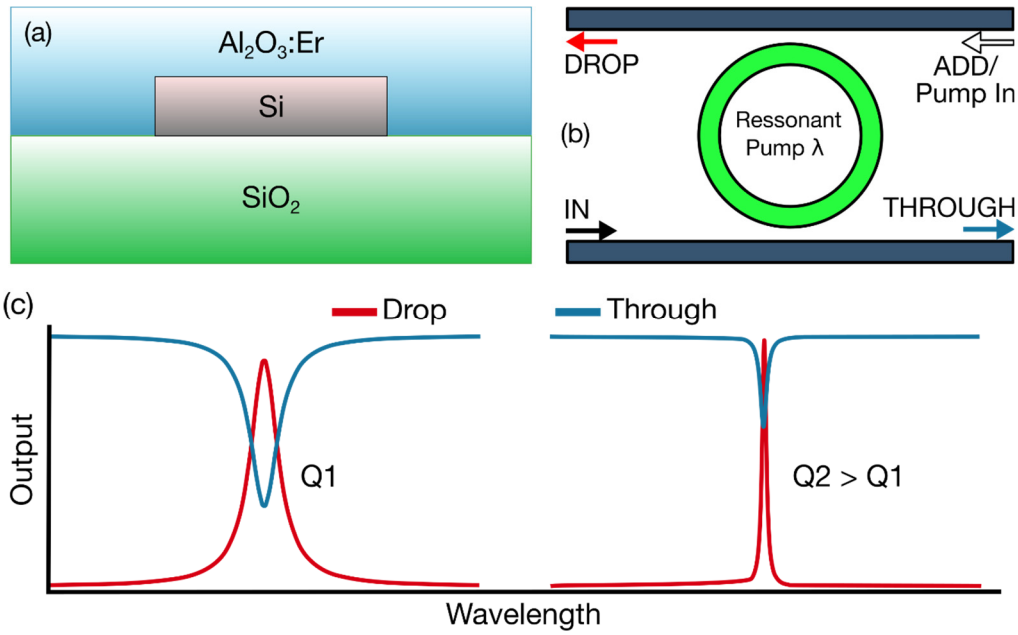

Fig. 1.8: (a) Layers composing the proposed ring waveguide. (b) Schematic of the device with all ports indicated. The ring is shown as green to illustrate that the pump laser is ressonant and confined within. (c) Qualitative illustration of the effect of the gain medium on drop and through ports power.

On a slightly different topic, an additional proposal involves III-V materials. Since they are widely used in lasers, in particular pump lasers for erbium excitation, an interesting idea would be the development of a complete optical amplifier on the same chip, from the doped waveguide to the pump laser. Erbium doped Al_2O_3 films can be used simultaneously as the waveguide core and insulating layer between the lasers. However, some processes employed in obtaining the film involve temperatures above 800 ^{o}C (see section 3.2). The maximum temperature involved in a laser fabrication is 420 ^{o}C, when annealing the electrical contacts, and can reach 800 ^{o}C only during the epitaxial

growth, causing concern that damages to the delicate structure, especially to the quantum well (QW), may occur. According to what we concluded from the study of lasers fabricated using Al_2O_3 films as insulating layers, these potential issues are present but can be prevented, enabling the development of III-V integrated photonics.

1.5 Thesis Organization

The full description of the work developed will be divided in 4 chapters. Chapter 2 will detail the theoretical aspects and modelling of the problem, starting with a brief review of how erbium has acquired so much importance, how its energy levels associated are used to provide amplification and lasing, and how the doped material can influence the absorption and emission cross-sections. Following that, a summary of the mathematics needed to describe a waveguide will be given, with simulations for the cases of interest, especially with a doped cladding. Our goal in this chapter is the development of a model for the proposed loss reduction method, with the expected results for realistic cases and for an optimal design. Before that, however, we need to review the theory behind optical amplification and ring resonators, to finally being able to combine them in one single model.

Chapter 3 begins with a description of the different techniques to obtain erbium-doped alumina films, giving special emphasis to the procedure we used, and reporting the optimization of the resulting film characteristics. Next, the experimental setup for the optical characterization of the film will be presented, along with the thermal annealing process needed to optimize the erbium luminescence. The final results will correspond to the optimal fabrication conditions, where high luminescence and uniformity are required. This has been presented in the LAOP 2012 Conference and SBMicro 2013 [47] [48].

In Chapter 4, the fabrication of components based on coupled ring resonators will be detailed, including the design, foundry process, and the postprocessing required

before depositing the Er-Doped cladding responsible for the loss reduction. The subsequent section will explain how to characterize these devices and show the experimental setup used, with the respective results. Finally, the procedure to measure the loss compensation will be described, and the analysis will confirm the benefits of the proposed method, as presented in CLEO 2017 [49], and published on IEEE Photonics Journal [50].

Chapter 5 focus on the second study we performed on Erbium-Doped Al_2O_3 films, which is the possibility of application on III-V integrated photonics chips. The first section describes in more detail a conceptual compact and monolithic optical amplifier in which such films could be employed, followed by the difficulties present, and the proposed experiment to study and develop a method to overcome the challenges. This experiment involves the design and fabrication of typical lasers used to pump Er-doped materials, which will also be detailed in this chapter. The measurements needed to characterize the effects of the alumina film and the high-temperature processes involved will be explained, and the results will show how we were able to overcome them. This work has been presented in SBMicro 2014 [51], where it received the Best Paper Award.

2. Theory

To accurately develop a model to describe the phenomena involved in this work, explain the experimental results, and to predict the effects of changes in certain parameters, it is necessary to study the theory behind key subjects. This chapter will cover this study and the linking of all topics, resulting in a complete model for the loss compensating method applied to ring resonators.

2.1 Erbium

With the development of high-quality and low-loss optical fibers, mainly developed by Corning [52], it became clear that the optimal wavelength range at which optical communications could be implemented was the optical C and L bands, that is, between 1530 and 1625 nm. The reason for that is that it is the span at which attenuation is minimal, as seen in Fig. 2.1a [53]. Coincidentally, having its energy spectrum thoroughly studied in the beginning of the 20th Century [54], erbium possesses transitions corresponding to this same range, as illustrated by Fig. 2.1b [55]. Thus, when the necessity for a different type of signal regeneration became more pressing, this element was the obvious candidate to be employed in optical fiber amplifiers.

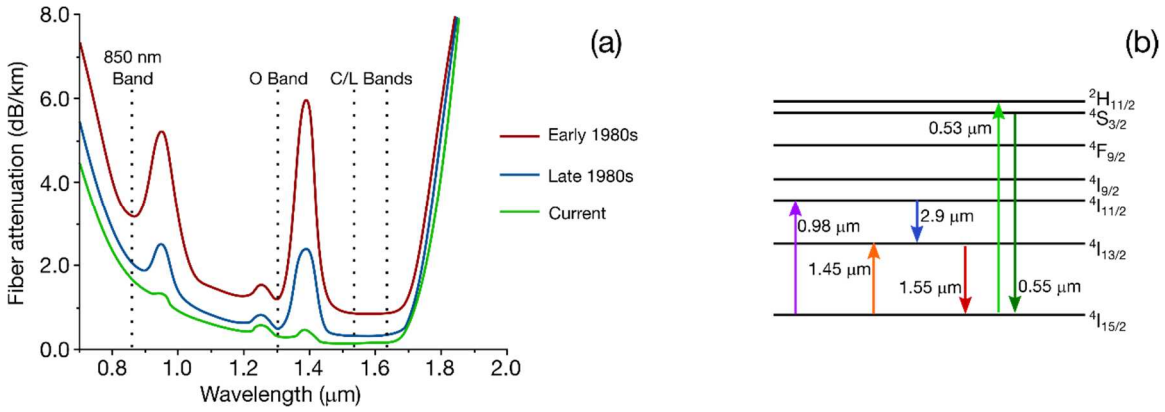

Fig. 2.1: (a) SiO_2 optical fibers attenuation spectra evolution [53]. (b) Erbium energy levels transitions [55].

One property of the lanthanides, crucial to this type of application, is the neutral electronic configuration of the form $[Xe]4f^N5d6s^2$, where N is the number of the *f* orbital electrons shielded by the $5s$ and $5p$ orbitals [56]. These N electrons are fundamental to the definition of the optical and magnetic properties of the material, but do not influence bonding and chemical characteristics in general. Consequently, when incorporated in other neutral materials matrices, erbium retains the same optical absorption and emission behavior, while adopting the +3 oxidation state. In this state, Er^{3+} has 11 electrons at $4f$, and due to Coulomb and spin-orbit interactions, several degeneracies are created, as seen in Fig. 2.2a. This leads to many 4f energy levels, and each one of them is in fact composed by Stark level manifolds [57]. In other words, each level consists on many sub-levels with energies depending on local electric fields, as illustrated in Fig. 2.2b.

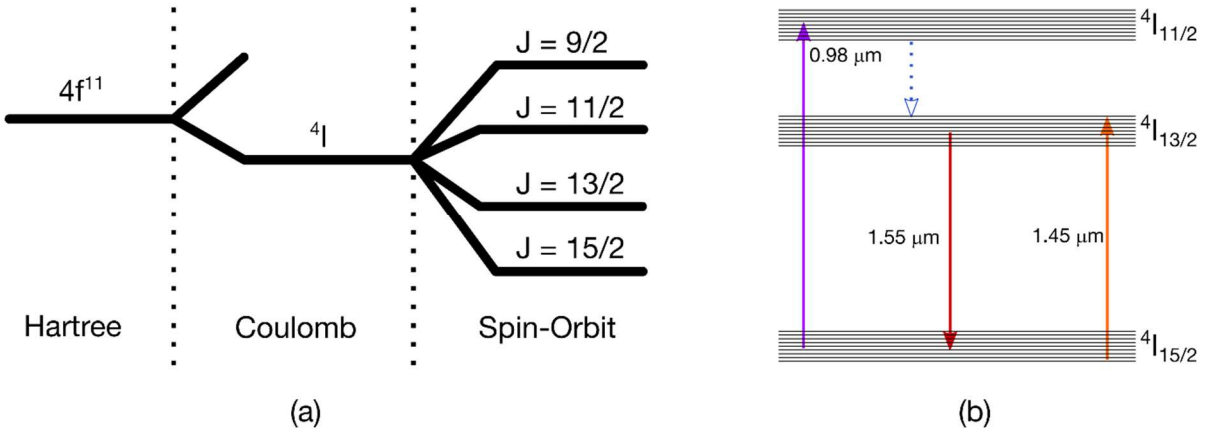

Fig. 2.2: (a) Degeneracies created in erbium. (b) Corresponding energy transitions of interest to this work.

Of particular interest to optical amplification are the $^4I_{15/2} \rightarrow {}^4I_{11/2}$ and $^4I_{13/2} \longleftrightarrow {}^4I_{15/2}$ transitions, with 980 nm and 1550 nm as the associated wavelengths, respectively. When a 980 nm laser is used to pump an EDFA, Er^{3+} ions absorb the photons and are promoted to the $^4I_{11/2}$ state, eventually decaying to the $^4I_{13/2}$ state, non-radiatively (~1 μs). The $^4I_{13/2} \rightarrow {}^4I_{15/2}$ transition, in turn, is radiative, but with a relatively long lifetime, in the order of 8 ms (spontaneous emission). It is this transition that is

responsible for the amplification at telecommunications wavelengths, via stimulated emission. The difference between these two types of emissions is that the former occurs spontaneously when no external perturbation exists, and the photon is emitted on a random direction, while the latter is caused by an external perturbation, usually an incoming photon. The emitted light possesses the same direction, phase, polarization, and frequency as the first photon [58]. Stimulated emission occurs on a limited bandwidth around the energy transition, and on the erbium-doped optical amplifier case, the resulting device bandwidth is increased due to the Stark manifolds, since different ions can be at different sublevels.

Another way of exciting an ion to the $^4I_{13/2}$ level is using 1480 nm as the pump wavelength. Normally, a direct pumping scheme such as this would not be effective, because the pump would cause stimulated emission at the same time as it excites the ions. Since there are Stark level manifolds, however, the ion can be promoted to a more energetic sublevel. Due to thermal effects, this ion quickly (~ps) decays to a lower sublevel, and a lower energy photon is necessary to stimulate the emission [59].

The overall effect the Stark sublevels have on the absorption and emission characteristics of Er^{3+} ions can be summarized as cross-sections spectra. The absorption or emission cross-section, denoted as σ, is defined as the probability that an ion absorbs or emits a photon, and is related to the rate of these events, by:

$$R_{a,e}(\lambda) = \sigma_{a,e}(\lambda)\frac{P\lambda}{E_{ph}} = \sigma_{a,e}(\lambda)\frac{P\lambda}{hc}. \tag{2.1}$$

In this equation, R is the rate, P the input optical power, E_{ph} the photon energy, λ and c the wavelength and the speed of light in vacuum, and h Planck's constant. The subscripts a and e refer to absorption and emission, respectively. Typical erbium absorption and emission cross-sections spectra are plotted in Fig. 2.3 [55] [60]. We can clearly see a peak at 1535 nm with a bandwidth of nearly 40 nm, covering the C and

most of the L bands, which demonstrates the importance of erbium in optical communications.

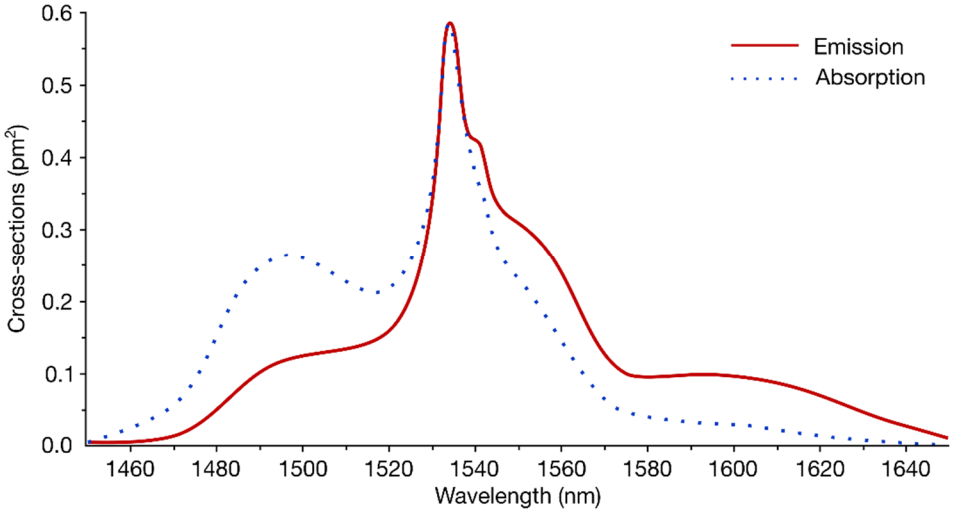

Fig. 2.3: Typical Erbium absorption and emission cross-sections spectra [55].

2.2 Waveguides

Optical fibers have been mentioned since the beginning of this document, but the main concept responsible for the ability to guide light was only briefly explained: reflection. This section will cover the principles involved in this guiding in more detail.

In summary, waveguides are objects consisting of inhomogeneous materials, capable of guiding light through an almost arbitrary path. While reflection (or total internal reflection, for dielectrics) is a good approximation to explain the principle of a waveguide for some cases, it considers the geometric nature of light waves, and when used to describe situations where small cores or small refractive index contrasts are present, the model loses accuracy. In 1893, Oliver Heaviside was the first to study the guided wave phenomenon, concluding that on hollow metallic tubes it was not possible [61]. However, at the same time J. J. Thomson reported the existence of allowed normal modes depending on the radius of a finite tube, and shortly after that J. Larmor published his study of resonant coaxial metallic cylinders. [62] [63]. It was not long before Lord Rayleigh solved the boundary-value problem of electromagnetic waves travelling in a

hollow conducting cylinder [64]. He found that this was only possible for a set of normal modes, one with the longitudinal component being electric only, and another with the longitudinal component being magnetic only.

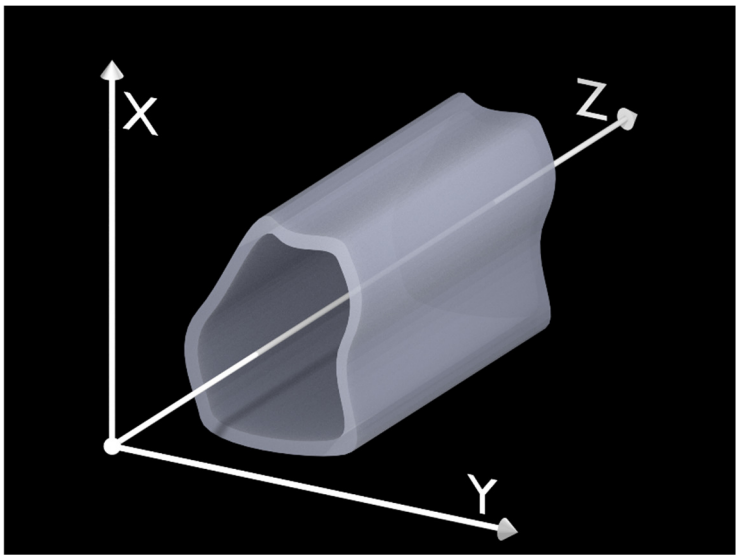

Fig. 2.4: Hollow cylindrical waveguide with arbitrary-shaped cross-section. The wave propagates in the z direction.

To reach this conclusion ourselves, we begin by considering a hollow cylindrical waveguide with an arbitrary-shaped cross-section, as seen in Fig. 2.4. Since the waveguide is composed of a conductive material, we assume that the electric (E) and magnetic (B) fields inside the material are null, so we have the boundary conditions:

$$\begin{array}{ll} (i) & \vec{E}^{\parallel} = 0 \\ (ii) & \vec{B}^{\perp} = 0 \end{array}. \tag{2.2}$$

As the waves propagate in the z direction, they will have the form:

$$\begin{array}{ll} (i) & \vec{E}(x,y,x,t) = \vec{E}_0(x,y)e^{i(kz-\omega t)} \\ (ii) & \vec{B}(x,y,x,t) = \vec{B}_0(x,y)e^{i(kz-\omega t)} \end{array}, \tag{2.3}$$

where k is the propagation constant, ω the angular frequency, and t represents time. These waves must satisfy Maxwell's equations when all charges and currents are null (because the waveguide is hollow):

$$\begin{aligned} &(i)\quad \vec{\nabla}\cdot\vec{E}=0 \\ &(ii)\quad \vec{\nabla}\cdot\vec{B}=0 \\ &(iii)\quad \vec{\nabla}\times\vec{E}=-\frac{\partial\vec{B}}{\partial t} \\ &(iv)\quad \vec{\nabla}\times\vec{B}=\frac{1}{c^2}\frac{\partial\vec{E}}{\partial t} \end{aligned} \qquad (2.4)$$

We can separate the electric and magnetic fields into their spatial components, and inserting them in (2.4 *iii*) and (2.4 *iv*), after some manipulation, yields:

$$\begin{aligned} &(i)\quad E_x=\frac{1}{(\omega/c)^2-k^2}\left(k\frac{\partial E_z}{\partial x}+\omega\frac{\partial B_z}{\partial y}\right) \\ &(ii)\quad E_y=\frac{1}{(\omega/c)^2-k^2}\left(k\frac{\partial E_z}{\partial y}-\omega\frac{\partial B_z}{\partial x}\right) \\ &(iii)\quad B_x=\frac{1}{(\omega/c)^2-k^2}\left(k\frac{\partial B_z}{\partial x}-\frac{\omega}{c^2}\frac{\partial E_z}{\partial y}\right) \\ &(iv)\quad B_y=\frac{1}{(\omega/c)^2-k^2}\left(k\frac{\partial B_z}{\partial y}+\frac{\omega}{c^2}\frac{\partial E_z}{\partial x}\right) \end{aligned} \qquad (2.5)$$

It is easy to notice that if we have only the z components, all others can be easily found. If we now insert (2.5) in (2.4 *i*) and (2.4 *ii*), we finally obtain:

$$\begin{aligned} &(i)\quad \left[\frac{\partial^2}{\partial x^2}+\frac{\partial^2}{\partial y^2}+\left(\frac{\omega}{c}\right)^2-k^2\right]E_z=0 \\ &(ii)\quad \left[\frac{\partial^2}{\partial x^2}+\frac{\partial^2}{\partial y^2}+\left(\frac{\omega}{c}\right)^2-k^2\right]B_z=0 \end{aligned} \qquad (2.6)$$

The trivial solutions to (2.6), when $E_z=0$ and $B_z=0$, are called TE and TM modes respectively, which are the same allowed modes found by Lord Rayleigh. Returning to (2.5), we obtain the description of the waves travelling over the waveguide [65].

There are several applications for devices that originated from these studies, from microwave ovens, to cable TV and integrated circuits. However, the most relevant waveguides to this work are different from these former examples, since they are not metallic or conductors in general, but dielectrics. Only in 1910 these structures became well-understood, when Hondros and Debye obtained the solutions for a wave propagating on a cylindrical dielectric waveguide [66].

The simplest case to study in detail is the slab waveguide, illustrated in Fig. 2.5. It consists of 3 layers with infinite length and width (z and x directions, respectively), but finite height (h, y direction). The middle layer has a higher refractive index, which we will assume are equal, so that $n_2 > n_1$.

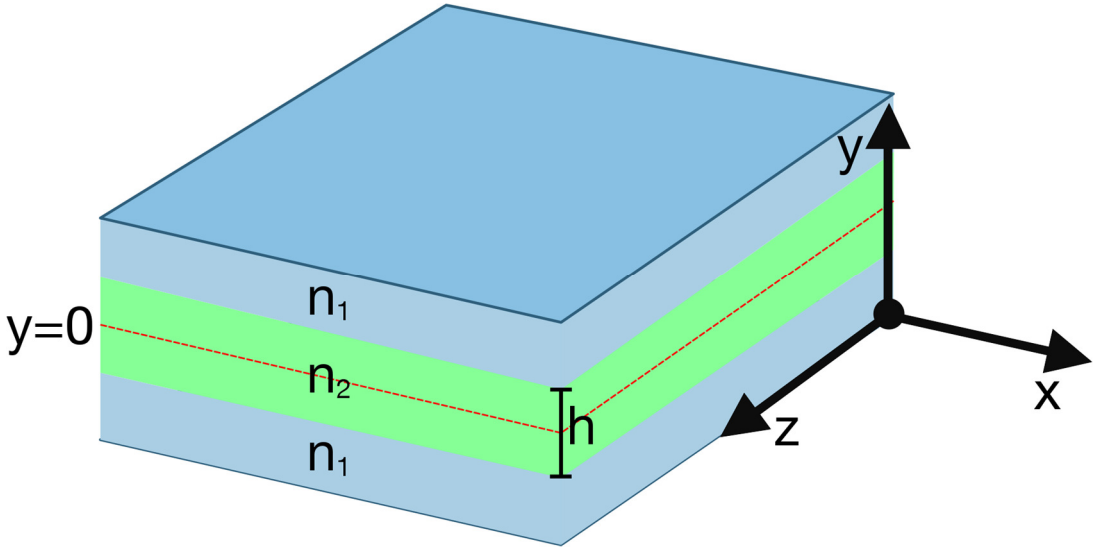

Fig. 2.5: Schematic of a slab waveguide. The wave propagates in the z direction.

As in the case discussed above, in this type of waveguide the TE and TM propagation modes are also present. If we follow a similar procedure, but considering Maxwell's equations in matter and continuity boundary conditions, we obtain:

$$\begin{aligned}
&(i) \quad \left[\frac{\partial^2}{\partial x^2}+\frac{\partial^2}{\partial y^2}-\delta^2\right]E_{z1}=0 \\
&(ii) \quad \left[\frac{\partial^2}{\partial x^2}+\frac{\partial^2}{\partial y^2}-\delta^2\right]B_{z1}=0 \qquad (v) \quad \delta^2=k^2-\left(\frac{n_1\omega}{c}\right)^2 \\
&(iii) \quad \left[\frac{\partial^2}{\partial x^2}+\frac{\partial^2}{\partial y^2}+\kappa^2\right]E_{z2}=0 \qquad (vi) \quad \kappa=\left(\frac{n_2\omega}{c}\right)^2-k^2 \\
&(iv) \quad \left[\frac{\partial^2}{\partial x^2}+\frac{\partial^2}{\partial y^2}+\kappa^2\right]B_{z2}=0
\end{aligned} \qquad (2.7)$$

These equations are equivalent to (2.6), with the only difference being that we now have to worry about the waves outside the waveguide core, denoted by the 1 subscript. For the waves inside the core, we use the subscript 2. Since k must be equal in all the waveguide regions, we can combine (2.7 v) and (2.7 vi):

$$\kappa^2 + \delta^2 = (n_2^2 - n_1^2)\left(\frac{\omega}{c}\right)^2 . \tag{2.8}$$

For the TE mode inside the waveguide, we then obtain:

$$\begin{aligned} E_{x2} &= \frac{i\omega}{\kappa^2 c}\frac{\partial B_{z2}}{\delta y} \\ B_{y2} &= \frac{ik}{\kappa^2}\frac{\partial B_{z2}}{\delta y} \end{aligned} . \tag{2.9}$$

Now the magnetic field must be obtained. We can suggest solutions where the waves are oscillatory inside the core, and decay exponentially outside. Combining this with the continuity boundary conditions, we now have our final set of equations for this case:

$$\begin{aligned} &(i) \quad \vec{B}_2\left(h/2\right) = \vec{B}_1\left(h/2\right) \\ &(ii) \quad \frac{1}{\kappa^2}\frac{\partial \vec{B}_2}{\partial y}\bigg|_{\frac{h}{2}} = \frac{1}{\delta^2}\frac{\partial \vec{B}_1}{\partial y}\bigg|_{\frac{h}{2}} \\ &(iii) \quad \vec{B}_2 = Ae^{i\gamma y} + Be^{-i\gamma y}, |y| \le h/2 \\ &(iv) \quad \vec{B}_1 = Ce^{-\beta y}, |y| \ge h/2 \end{aligned} , \tag{2.10}$$

where A, B and C are constants, and β and γ are the imaginary and real propagation constants, respectively. From the z-component of the Poynting vector:

$$S_z = \frac{k\omega}{8\pi\mu_0\kappa^4}\left|\frac{\partial B_z}{\partial y}\right|^2 . \tag{2.11}$$

Since the transversal profile depends on the derivative of the magnetic field, it is convenient to separate the problem in even and odds solutions. For the even-TE case, $A = -B$, so:

$$\vec{B}_2 = A\left(e^{i\gamma y} - e^{-i\gamma y}\right) = \tilde{A}\,sin(\gamma y) . \tag{2.12}$$

With this, we can rewrite (2.10) equations as:

$$\begin{aligned} &(i) \quad \xi\,tan(\xi) = \eta && \xi^2 \equiv \frac{\gamma h}{2} \\ &(ii) \quad \xi^2 + \eta^2 = (n_2^2 - n_1^2)\left(\frac{\omega h}{2c}\right)^2 && \eta^2 \equiv \frac{\beta h}{2} \end{aligned} . \tag{2.13}$$

This results in a transcendental equation, and by plotting each side as a different curve, the solutions are the intersections between them. Fig. 2.6 illustrates the solution for different cases.

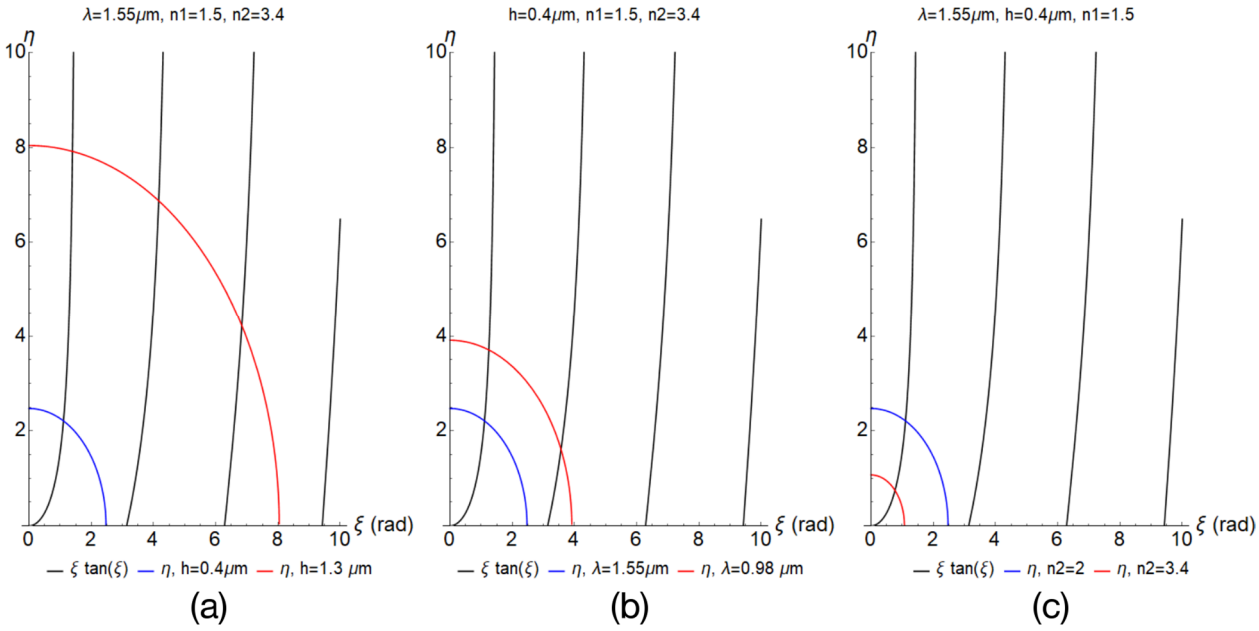

Fig. 2.6: Solutions to the waveguide even-TE transcendental equation in different situations, varying the waveguide core height (a), wavelength (b), and core refractive index (c).

We can see that the solutions vary dramatically when different parameters are changed. For a fixed wavelength of 1.55 μm, $n_1 = 1.5$, $n_2 = 3.4$, and waveguide core height of 0.4 μm there is only one solution. If the height is increased to 1.3 μm, there are now 3 solutions. Each of these solutions is a valid propagation mode. If we change the wavelength to 0.98 μm, again, we go from what is called single-mode, to multi-mode. By decreasing n_2 to 2, the confinement weakens, and the waveguide remains single-mode.

For the other special cases (odd-TE and TM modes) the analysis is very similar, and Fig. 2.7 shows all results for a wavelength of 1.55 μm, $n_1 = 1.5$, $n_2 = 3.4$, and waveguide core height of 1.3 μm.

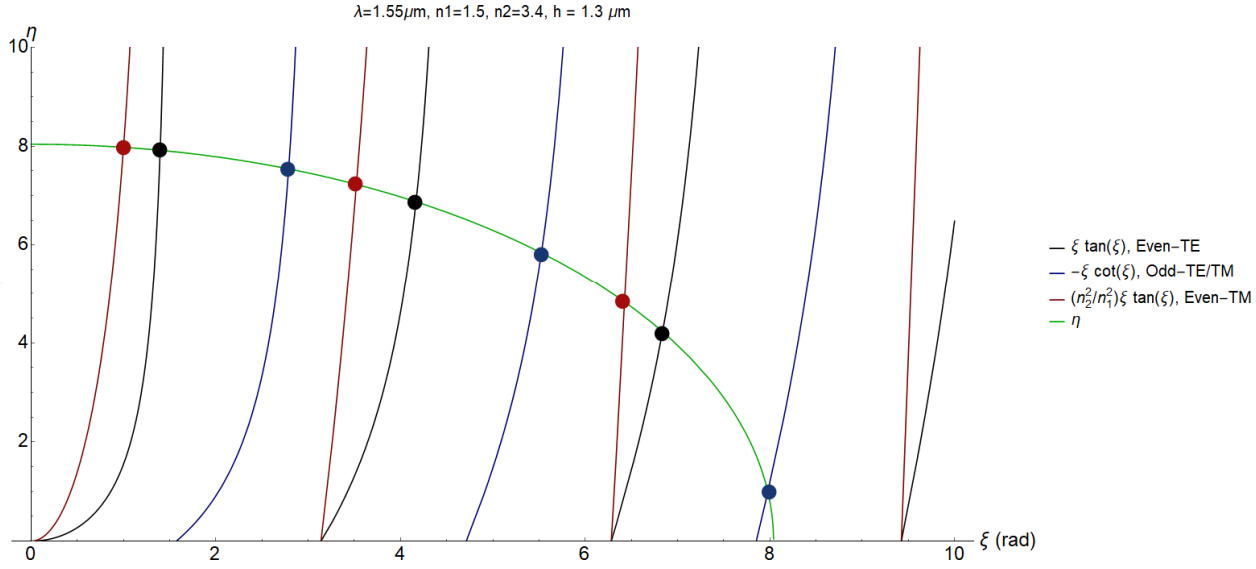

Fig. 2.7: General solution for a slab waveguide, for all special cases.

On the image above, the black, blue and red colors correspond to each special case, and the colored circles are the respective solutions. It is important to notice that the odd-TE and odd-TM modes are always degenerate, while for the even cases there is a small difference. For a waveguide to be single-mode, it is sufficient that $\xi < {}^{\pi}/_{2}$, since below this value there is only one tangent curve, so only one solution exists. However, it is not possible to have only TE or TM modes. The maximum waveguide height for single-mode operation therefore is:

$$h = \frac{\lambda}{\sqrt{4(n_2^2 - n_1^2)}}. \tag{2.14}$$

This analysis is important to develop the sense of how a waveguide works, both physically and mathematically. The only problem is that practical waveguides are always finite, so we cannot directly apply the same results to real cases. We can, however, consider a rectangular waveguide, ignore its width, and then solve for a slab waveguide of the same height, resulting in a certain propagation constant (β) from (2.13). From this value, we define an effective refractive Index:

$$n_{eff} = \frac{\beta}{k_0}. \tag{2.15}$$

Returning to the rectangular waveguide, we can now ignore its height and solve the resultant slab waveguide that has the same width, but infinite height. The only detail here, is that instead of using the refractive index for the core, we use the calculated effective index from (2.15). With that, we obtain the final propagation constant and effective index of the modes. This process, called the Effective Index Method [67], is illustrated in Fig. 2.8.

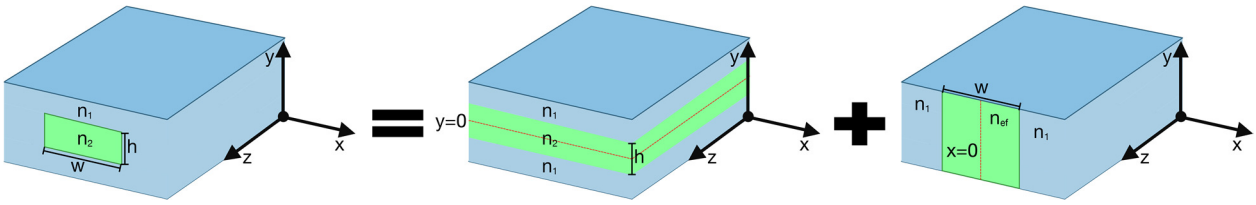

Fig. 2.8: Schematic of the Effective Index Method. A rectangular waveguide can be decomposed in two planar slab waveguides.

Remembering the total internal reflection explanation for the guiding of a wave, we can interpret the effective index as a quantity related to the angle of incidence of a light ray. Since the higher the index, the slower light travels, this is equivalent to more reflections per unit length for a higher effective index.

Although this method is only an approximation, it provides a good starting point for quickly evaluating the modal characteristics of a waveguide, as long as the aspect ratio is at least 3. For more accurate studies, it is necessary to use numerical methods, such as finite-difference time-domain (FDTD), finite element method (FEM), or beam propagation method (BPM). We'll now show FEM results (from Comsol Multiphysics) to illustrate the fundamental modes of certain waveguide structures.

For an example waveguide consisting of Al_2O_3 ($n = 1.7$) clad by SiO_2 ($n = 1.5$), we obtain the results in Fig. 2.9.

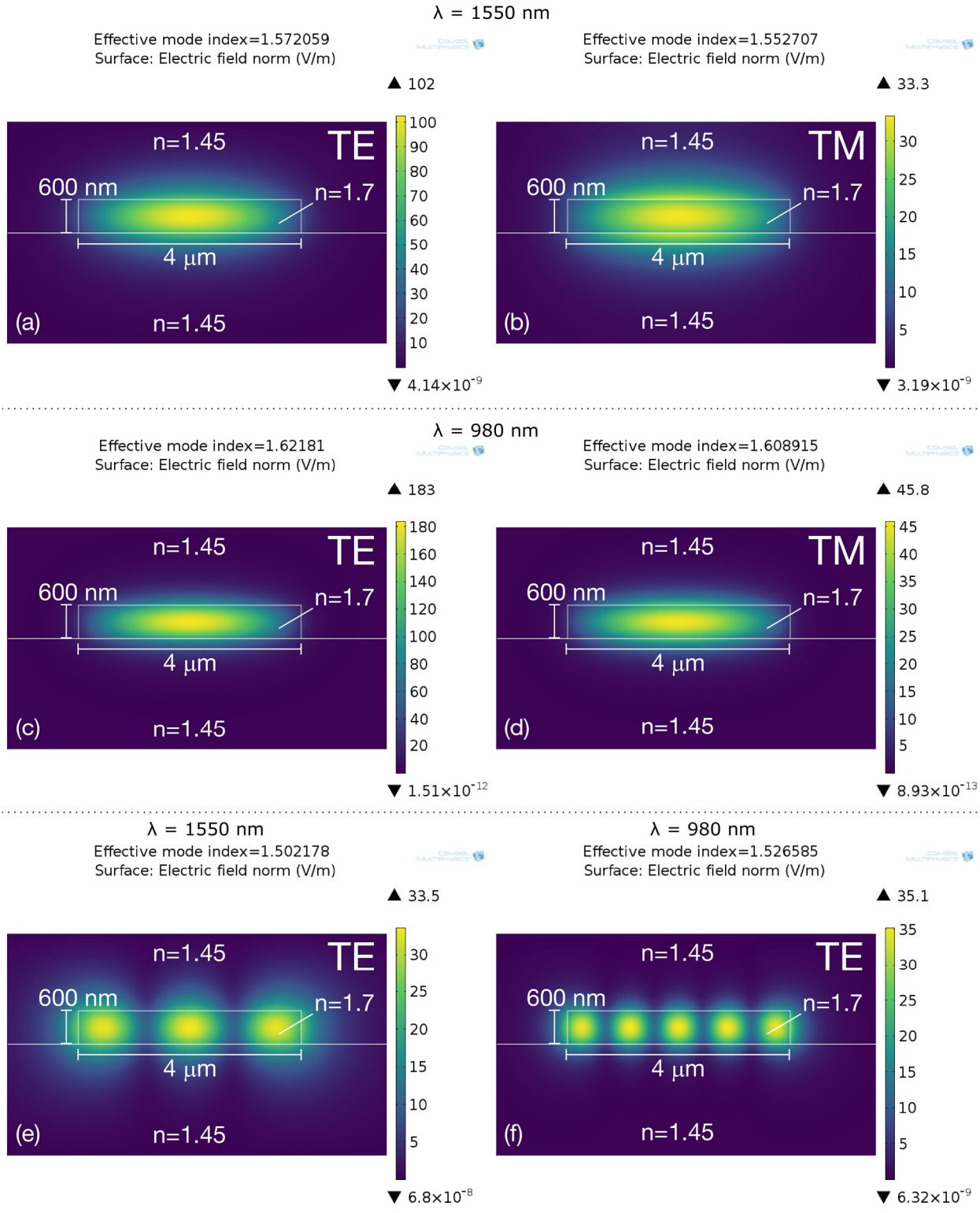

Fig. 2.9: TE and TM modes for an example waveguide comprised of Al_2O_3 and SiO_2, for a wavelength of 1550 nm (a, b), and 980 nm (c, d). This waveguide is multimode, supporting up to 3 intensity lobes for 1550 nm and 5 for 980 nm (d, e). These images were obtained via the Comsol Multiphysics software.

We see that the main difference between the TE and TM modes intensity profiles is that a discontinuity exists on the lateral (side) walls for TE, and vertical walls

(top/bottom) for TM. This arises from the continuity boundary conditions, demonstrating that for TE modes the Electric field is in the x direction, and in the y direction for TM modes. If the wavelength is decreased from 1550 nm to 980 nm, it's clear that the wave is more strongly confined. We can define a confinement factor Γ as the ratio between the energy inside the core and the total energy. Considering only the fundamental TE mode, for 1550 nm this value is $\Gamma = 0.43$, and for 980 nm, $\Gamma = 0.65$. This waveguide is clearly multimode, and it's possible to see that if 980 nm is used, more intensity lobes are supported (5, as opposed to 3 for 1550 nm).

One design of interest to our work is an asymmetrical waveguide comprised of Si as the core material, SiO_2 as the bottom cladding, and Al_2O_3 as the top cladding. For this case, the results are shown in Fig. 2.10.

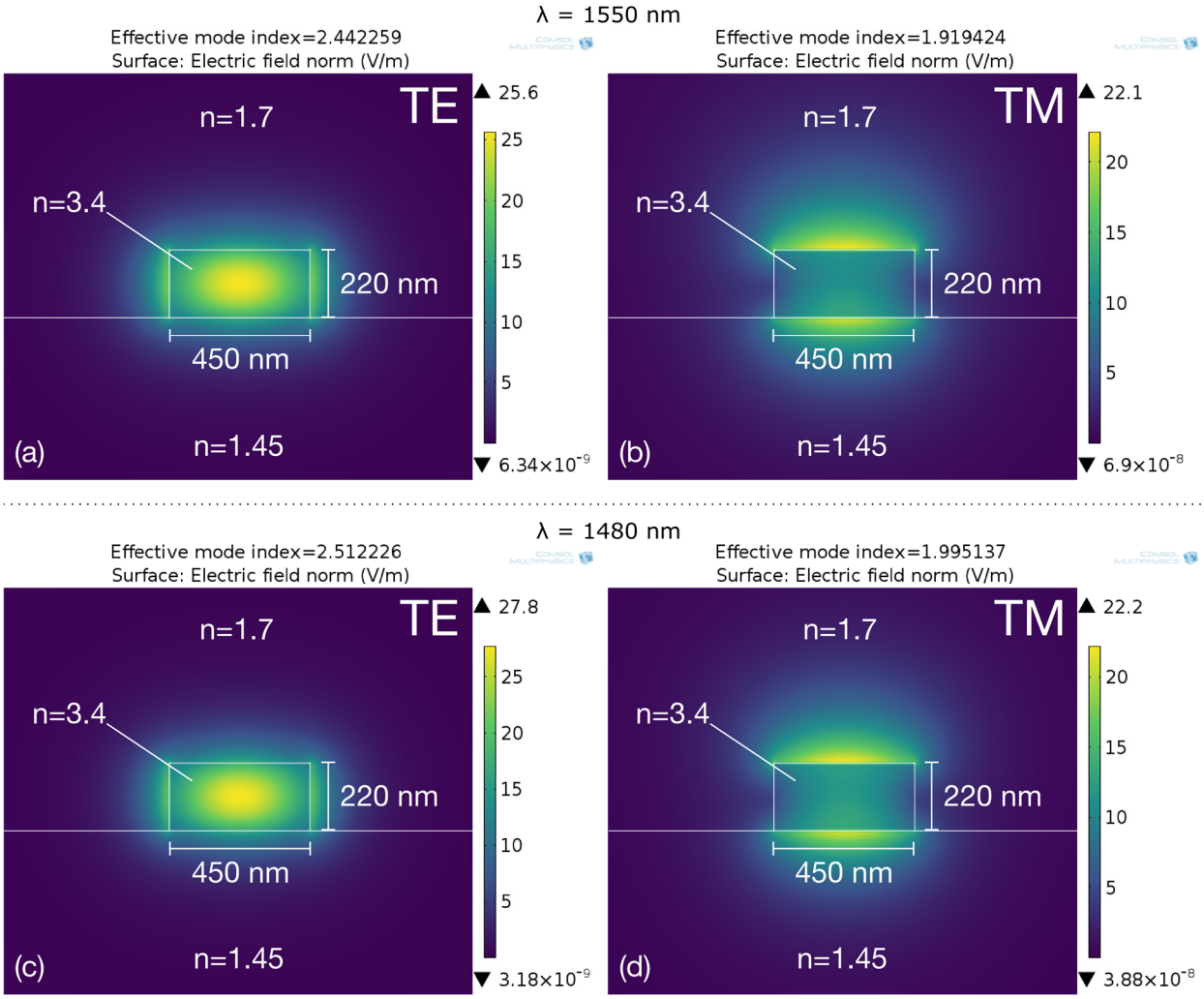

Fig. 2.10: TE and TM modes for a waveguide comprised of a Si core, Al_2O_3 as the top cladding, and SiO_2 as the bottom cladding, for a wavelength of 1550 nm (a, b), and 1480 nm (c, d).

This waveguide is single-mode, supporting only the fundamental TE and TM modes. This final result, for both 1550 nm and 1480 nm, will be very important for the development of the models in the subsequent sections of this chapter.

2.3 Optical Amplification

Erbium-doped optical amplifiers rely on the stimulated emission from excited-state Er^{3+} ions, as discussed in section 2.1. We begin our mathematical modelling of an amplifier by constructing a rate equation for this phenomenon, using a two-state system approximation. If there is a number N_T of dopant ions per unit length, N_1 of these at the fundamental state, and N_2 at the excited state of interest, so $N_T = N_1 + N_2$, there are three factors that influence the variation of N_2 in time. The first is the increase by photons absorbed by fundamental state ions (either pump or signal), and the remaining two are the decrease by stimulated and spontaneous emission. Let's say that spontaneous emission occurs at a certain rate r_{sp}, and both the photon absorption and stimulated emission have a certain probability $\rho_{a,e}(\lambda)$ of happening. For $N_{Ph}(\lambda)$ incident photons per unit time, we can intuitively write:

$$\frac{dN_2}{dt} = \rho_a(\lambda_p)N_{Ph}(\lambda_p)N_1 + \rho_a(\lambda_s)N_{Ph}(\lambda_s)N_1 - \rho_e(\lambda_s)N_{Ph}(\lambda_s)N_2 - r_{sp}N_2. \qquad (2.16)$$

The p and s subscripts refer to pump and signal, respectively. The number of photons can be obtaining by:

$$N_{Ph}(\lambda) = \frac{P\lambda}{hc}. \qquad (2.17)$$

Substituting 2.17 in 2.16, we obtain terms that are each very similar to (2.1). The probability of a photon being absorbed or being emitted via stimulation is defined by the absorption or emission cross-sections. The optical power in the waveguide does not completely overlap with the doped area, as can be seen by the propagation modes

from Fig. 2.9 and Fig. 2.10. We can obtain an overlap factor Γ as the ratio between the energy being carried in the doped area and the total energy in the waveguide. Thus, we can finally rewrite 2.16 as the final rate equation for optical amplification for a waveguide of transversal area A:

$$\frac{dN_2}{dt} = \left(\Gamma_p \frac{\sigma_a(\lambda_p)}{A}\frac{P_p\lambda_p}{hc} + \Gamma_s \frac{\sigma_a(\lambda_s)}{A}\frac{P_s\lambda_s}{hc}\right)N_1 - \Gamma_e \frac{\sigma_e(\lambda_s)}{A}\frac{P_s\lambda_s}{hc}N_2 - \frac{N_2}{\tau}. \tag{2.18}$$

Here, τ is the lifetime of the excited state, or the average time before decaying spontaneously, and for erbium it is approximately 8 ms. If we now consider the steady state ($dN_2/dt = 0$), we can easily solve the rate equation and obtain, for a certain z position:

$$N_2(z) = \frac{\Gamma_p\sigma_a(\lambda_p)P_p\lambda_p + \Gamma_s\sigma_a(\lambda_s)P_s\lambda_s}{\Gamma_p\sigma_a(\lambda_p)P_p\lambda_p + \Gamma_sP_s\lambda_s\big(\sigma_a(\lambda_s) + \sigma_e(\lambda_s)\big) + {hc\,A}/{\tau}}N_T. \tag{2.19}$$

Typically, the signal will be amplified and the pump attenuated when travelling through the amplifier waveguide. So, we can define gain (g) and depletion (η) functions as:

$$\begin{array}{ll}(i) & g(z,\lambda_s) = \Gamma_s[\sigma_e(\lambda_s)N_2(z) - \sigma_a(\lambda_s)N_1(z)] \\ (i) & \eta\big(z,\lambda_p\big) = \Gamma_p\big[\sigma_e(\lambda_p)N_2(z) - \sigma_a(\lambda_p)N_1(z)\big]\end{array}. \tag{2.20}$$

The power variation along the direction of travelling for the signal and pump will then be:

$$\begin{array}{ll}(i) & \dfrac{dP_s(z)}{dz} = (g(z,\lambda_s) - \alpha)P_s(z) \\ (ii) & \dfrac{dP_p(z)}{dz} = \big(\eta\big(z,\lambda_p\big) - \alpha\big)P_p(z)\end{array}. \tag{2.21}$$

Here, α represents intrinsic attenuation. If we consider the example waveguide from Fig. 2.9 (Al_2O_3 with SiO_2 cladding) to be 20 cm long, the confinement factors previously mentioned (area of 2.4 μm^2), 1 dB/cm of loss, the erbium cross-sections from Fig. 2.3 and concentration of 2 x 10^{20} cm^{-1}, solving (2.19), (2.20) and (2.21) yields:

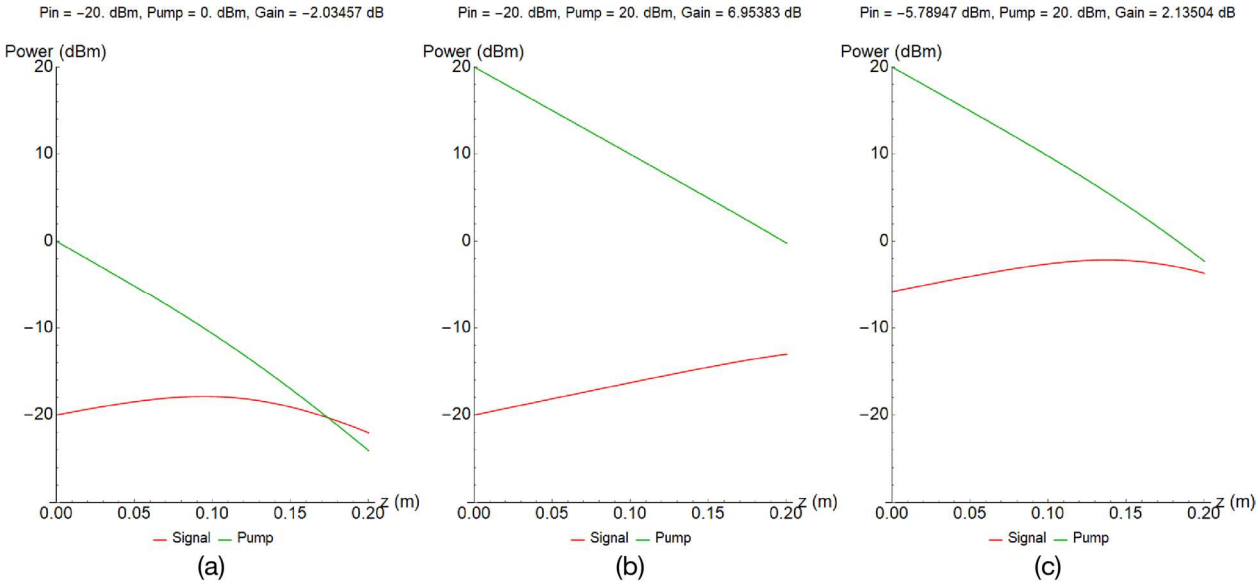

Fig. 2.11: Example of amplification for a Al_2O_3 waveguide, for different pump and signal conditions.

The graphs on Fig. 2.11 show the pump and signal power along the waveguide for different initial conditions. If the pump power is 0 dBm, the signal starts to be amplified, but there is a point in which not enough Er^{3+} ions are excited. So, not only is the signal more absorbed by fundamental state ions, but also the natural waveguide loss contributes to a decrease in power, resulting in a net loss of 2 dB at the end of the amplifier (Fig. 2.11a). If the pump level is increased to 20 dBm, for example, enough ions are excited to provide stimulated emission and the result is a net gain of almost 7 dB (Fig. 2.11b). As the signal input power is increased, we slowly return to the first situation. When the input goes from -20 dBm to -6 dBm, we still have gain, but it is decreased to 2 dB (Fig. 2.11c).

To provide a more general explanation, density and 3D plots of the gain and output power are shown in Fig. 2.12.

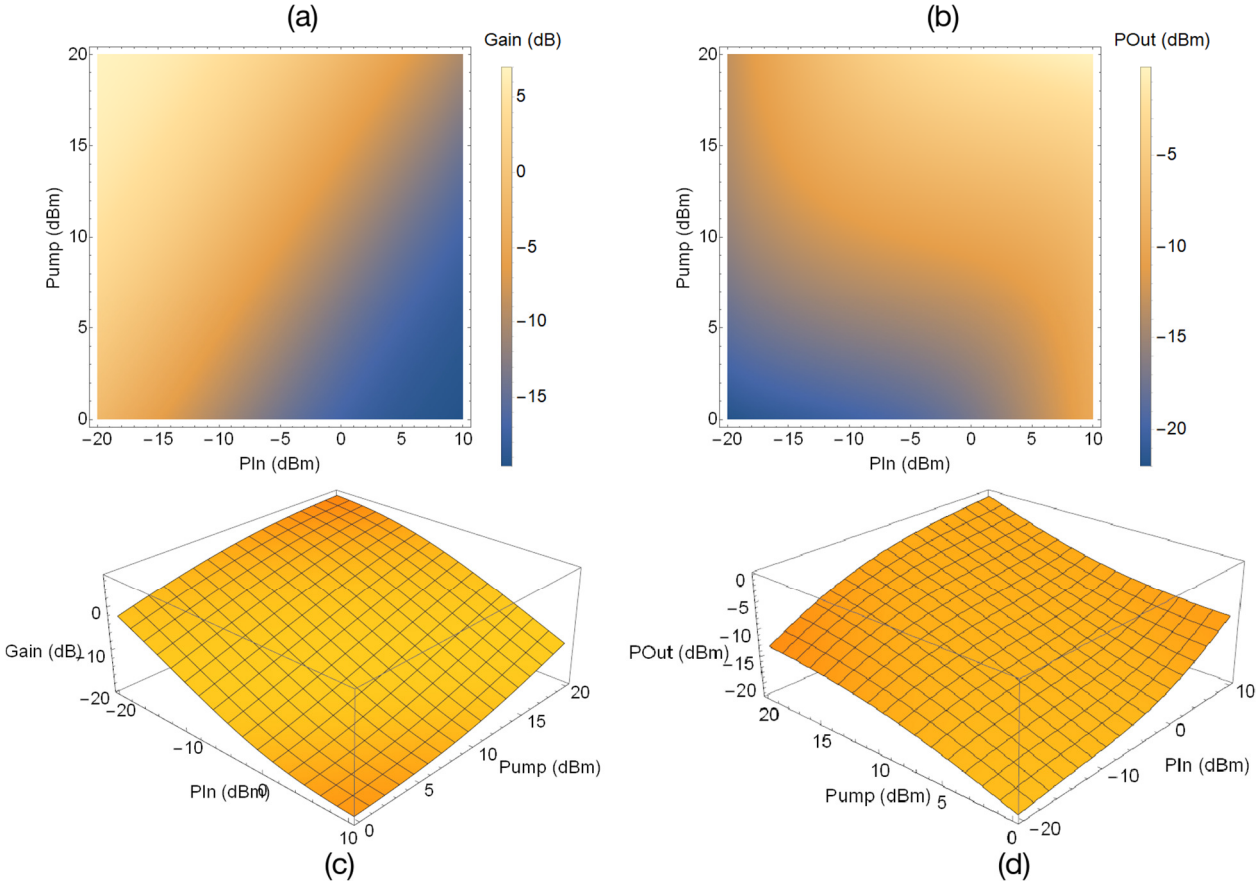

Fig. 2.12: Density (a, b) and 3D (c, d) plots of gain x input power x pump power, and output power x input power x pump power, for the example waveguide.

From this data we observe that as the pump power increases, the gain and output power follows, but if the input signal power is increased, the gain tends to decrease, while the output power depends on the pump condition. There is a minimum pump power/input power ratio that needs to be achieved if amplification is the goal. When this ratio is achieved, $N_2 > N_1$, which is referred to as population inversion. It is also worth mentioning the condition where the gain starts to saturate, and thus the output power is the same for a certain range of input power. This is an important operation point for erbium doped amplifiers, making sure the output signal in different conditions is always the same, increasing the system predictability.

One last quantity that will be very useful later on is the exponential gain coefficient. As dBm is a logarithmic scale, from Fig. 2.11b we see that the signal and pump power change exponentially, so we can write:

$$I(z) = I_0 e^{2\xi z}, \tag{2.22}$$

where I is the intensity, and ξ is the increase/decrease coefficient. By solving the rate equations and taking the output and input power, we have:

$$\frac{P_{out}(z)}{P_{in}} = \frac{I(z)}{I_0} = \frac{|E(z)|^2}{|E_0|^2} = e^{2\xi z}. \tag{2.23}$$

Rearranging the terms, we obtain:

$$\xi = \frac{1}{z} ln\left(\frac{|E(z)|}{|E_0|}\right) = \frac{1}{2z} ln\left(\frac{I(z)}{I_0}\right) = \frac{1}{2z} ln\left(\frac{P_{out}(z)}{P_{in}}\right). \tag{2.24}$$

This coefficient will be necessary in section 2.5, as the bridge between optical amplification and resonator response.

2.4 Micro-resonators

As mentioned in Chapter 1, ring resonators are building blocks used for many studies and applications in silicon photonics. By approximating the bus waveguide to the ring, light is coupled via evanescent field, which occurs when the interaction between the electric and magnetic fields from two waveguides is strong enough, and induced surface charges and currents cause the exchange of energy between them. We can begin to model this coupling by describing the superposition of the individual modes of propagation of each waveguide as one collective mode [68]. In the case of single-mode waveguides, there will be symmetric and anti-symmetric solutions. Since each of them propagates with a different constant, the intensity profile will be different as the waves travel, as illustrated in Fig. 2.13. The length at which the power has been completely transferred from one waveguide to the other is called the beat length, and it increases with the separation distance.

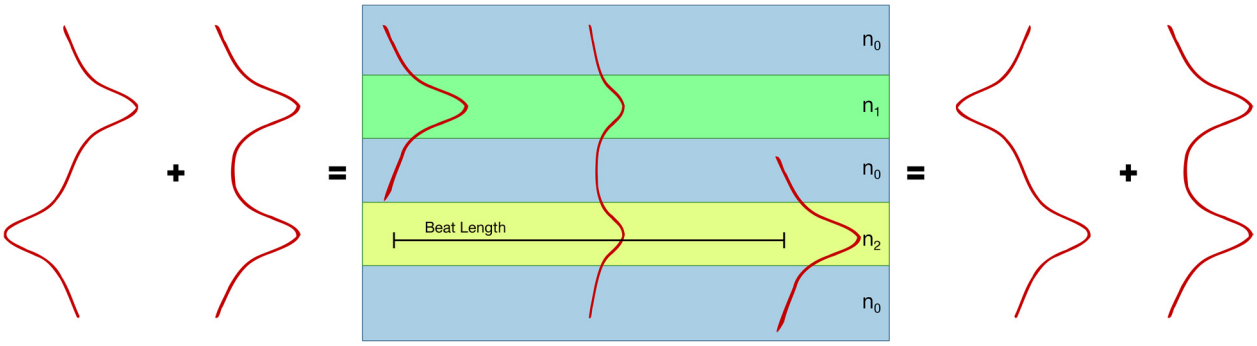

Fig. 2.13: Energy transfer between waveguides described by symetric and anti-symetric collective modes.

By solving this type of "coupled" waveguides using numerical methods, it is not difficult to obtain the beat length and use that to design optical couplers or power splitters. However, when we consider one of the waveguides to be curved, as is the case of a ring resonator, the rate at which the energy is transferred varies along the interaction length. This adds a new layer of complexity, requiring more thorough FEM or BPM simulations to accurately model a device. Nevertheless, in 1997, Little *et al.* provided an approximation to the problem [69], and the coupling constant κ (the fraction of the field amplitude that is coupled) can be calculated by:

$$\kappa = \frac{\omega\varepsilon_0\, cos(k_{x2}w_2)}{2\sqrt{P_1P_1}(k_{x1}^2+\alpha_2^2)}(n_1^2-n_0^2)\sqrt{\frac{\pi R}{\alpha_2}}e^{\alpha_2(w_2-2s_0)}\times$$
$$[\alpha_2 cos(k_{x1}w_1)\, sinh(\alpha_2 w_1)+k_{x1}sin(k_{x1}w_1)\, cosh(\alpha_2 w_1)]. \qquad (2.25)$$

In this equation, ω is the angular frequency, ε_0 the vacuum permittivity, k_{xi} transverse propagation constant in the corresponding waveguide, w_i is half the waveguide width, P_i the mode power, α_i the decay constant, n_i the refractive index (0 is relative to the cladding), R is the curvature radius, and $2s_0$ is the separation length, center to center. The quantities k_{xi}, P_i, and α_i can be found by:

$$(i)\quad k_{xi}=\sqrt{n_i^2k^2-\beta_i^2}$$
$$(ii)\quad \alpha_i=\sqrt{\beta_i^2-n_0^2k^2}\quad , \qquad (2.26)$$
$$(iii)\quad P_i=\frac{\beta_i}{2\omega\mu_0}\left(w_i+\frac{1}{\alpha_i}\right)$$

where k is free space wave vector, β_i the waveguide propagation constant, and μ_0 the vacuum magnetic permeability.

Once we have the κ value for a certain geometry, it is straightforward to predict the behavior of a ring resonator. Let us consider the case of Fig. 2.14. The wave travels along the bus waveguide until it reaches the coupling area, where the electric field is coupled to the ring waveguide by a factor of κ. The remaining field continues on the bus, with the amplitude decreased by a factor of τ. Considering power conservation, we can write:

$$\kappa^2 + \tau^2 = 1. \tag{2.27}$$

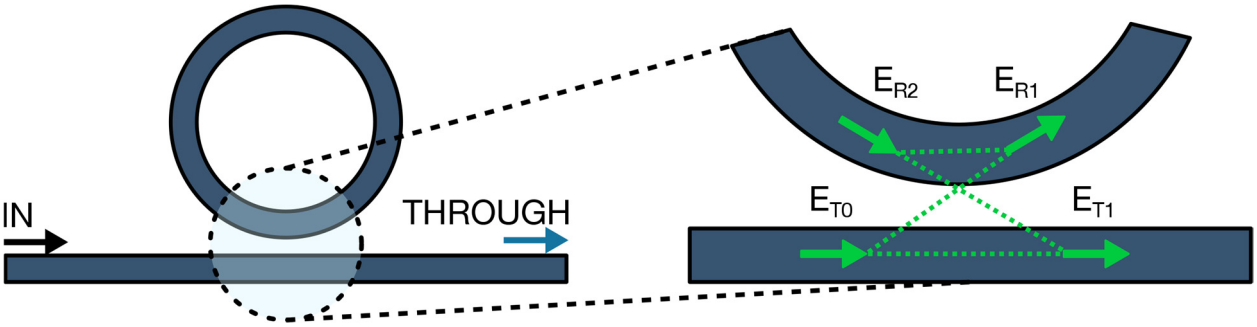

Fig. 2.14: Schematic of the coupling region of a ring resonator with only one bus waveguide.

The fraction of the light that couples into the ring remains inside, up to the point where one roundtrip is completed and it reaches the coupling region again. In the same manner as before, there is a power split, and part of the energy couples back to the bus waveguide, while the rest continues in the ring. At this point, there can be constructive or destructive interference on each of the waveguides. As the wave travelling inside the ring acquires a certain phase difference, there are conditions where depending on the wavelength, light will remain trapped inside the ring. This is called a resonance. To calculate the complete transmission spectrum and obtain the resonant wavelengths, we can write the power division in the coupling region as [70] [71]:

$$\begin{pmatrix} E_{R1} \\ E_{T1} \end{pmatrix} = \begin{pmatrix} \tau & i\kappa \\ i\kappa & \tau \end{pmatrix} \begin{pmatrix} E_{R2} \\ E_{T0} \end{pmatrix}. \tag{2.28}$$

This equation can be easily deduced by splitting the field amplitude using the κ and τ factors, and the complex number i arrives from power conservation. Considering that light is attenuated inside the ring by a factor a, we can define E_{R2}:

$$\begin{gathered}(i)\quad E_{R2} = ae^{i\varphi}E_{R1} \\ (ii)\quad a = e^{-\alpha 2\pi r} \\ (iii)\quad \varphi = \omega t_r = \frac{2\pi c}{\lambda}\frac{2\pi r}{v_g} = \frac{2\pi c}{\lambda}\frac{2\pi r n_g}{c} = \frac{4\pi^2 r n_g}{\lambda}\end{gathered}, \tag{2.29}$$

where α is the attenuation constant, φ the phase accumulated during one roundtrip (angular frequency multiplied by the roundtrip time), r is the ring radius, λ is the wavelength, and v_g and n_g are the group velocity and group index, respectively. The group velocity is a measurement of the overall velocity with which a wave travels along the waveguide, and the group index is related to the effective index by:

$$n_g = n_{ef} - \lambda\frac{dn_{ef}}{d\lambda}. \tag{2.30}$$

By solving (2.28) using (2.29) and defining $E_{T0} = 1$, we obtain for the output field:

$$E_{T1} = \tau + \frac{ae^{i\varphi}\kappa^2}{ae^{i\varphi}\tau - 1}. \tag{2.31}$$

By squaring the result from (2.31), we obtain the intensity in function of the wavelength. From this equation, we see that for a resonance wavelength ($e^{i\varphi} = \pm 1$), the transmission will be minimal when $a = \tau$. This is called the critical coupling condition.

For the waveguide from Fig. 2.10, (Si core with SiO_2 as the bottom cladding and Al_2O_3 as the top) separated by 200 nm from a resonator with 20 μm of radius, and an arbitrary loss of 2 dB/cm, the output spectrum is plotted in Fig. 2.15.

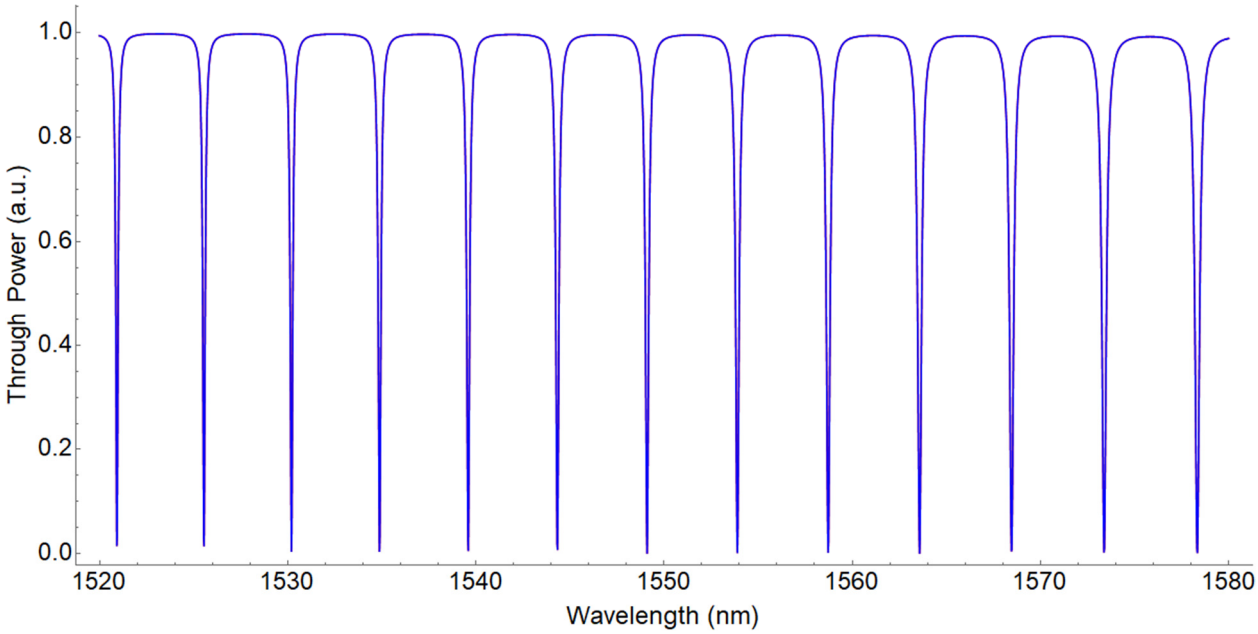

Fig. 2.15: Transmission spectrum for a Si ring resonator clad by SiO_2 and Al_2O_3.

The separation between each resonance is called free spectral range (FSR), and the ratio between input power and the transmitted power of a resonance is called extinction ratio. Both are important characteristics of a ring resonator, but another significant parameter is the quality factor (Q). It is defined by the ratio between the energy trapped inside the ring and the energy lost at each roundtrip. It can be easily calculated by:

$$Q = \frac{\lambda}{\Delta\lambda}, \tag{2.32}$$

where $\Delta\lambda$ is the resonance full width at half-maximum (FWHM). This factor is related to the finesse of the cavity, defined by:

$$F = \frac{Q\lambda}{2\pi r n_g}. \tag{2.33}$$

The finesse can be thought of as the average number of roundtrips a photon can exist inside the ring before exiting. Thus, we can also define the average photon lifetime as:

$$\tau_{ph} = \frac{2\pi r F}{v_g} = \frac{Q\lambda}{c}. \tag{2.34}$$

When a second waveguide is placed close to the ring, Add and Drop ports are introduced, as illustrated in Fig. 2.16.

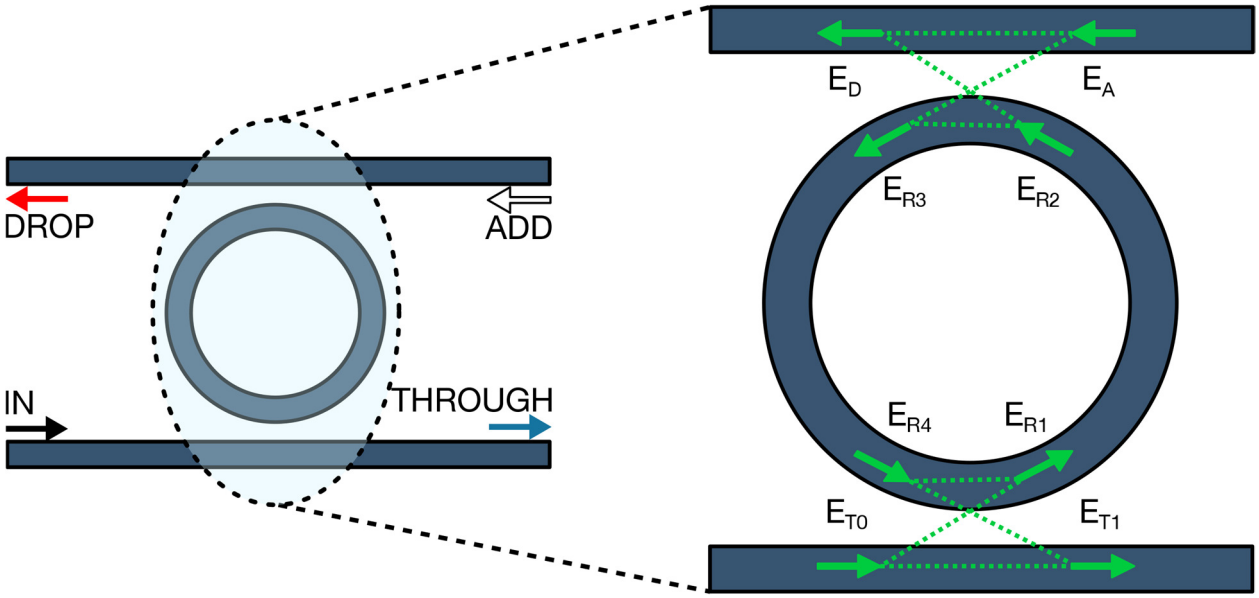

Fig. 2.16: Schematic of the coupling regions of a ring resonator with two bus waveguides.

By following the same procedure to obtain (2.28), it is simple to obtain the matrix equation for this case:

$$\begin{aligned} &(i) \quad \begin{pmatrix} E_{R1} \\ E_{T1} \end{pmatrix} = \begin{pmatrix} \tau & i\kappa \\ i\kappa & \tau \end{pmatrix} \begin{pmatrix} E_{R4} \\ E_{T0} \end{pmatrix} \\ &(ii) \quad \begin{pmatrix} E_{R2} \\ E_{A} \end{pmatrix} = \begin{pmatrix} \tau' & i\kappa' \\ i\kappa' & \tau' \end{pmatrix} \begin{pmatrix} E_{R3} \\ E_{D} \end{pmatrix}, \\ &(iii) \quad E_{R2} = ae^{i\varphi} E_{R1} \\ &(iv) \quad E_{R4} = ae^{i\varphi} E_{R3} \end{aligned} \tag{2.35}$$

Equation (2.35) can be solved in the same manner as (2.28), but now the phase difference is accumulated on only half the roundtrip for each coupling, and the parameters can be different. Considering the same separation for both waveguides, the output spectrum for the drop port is shown in Fig. 2.17.

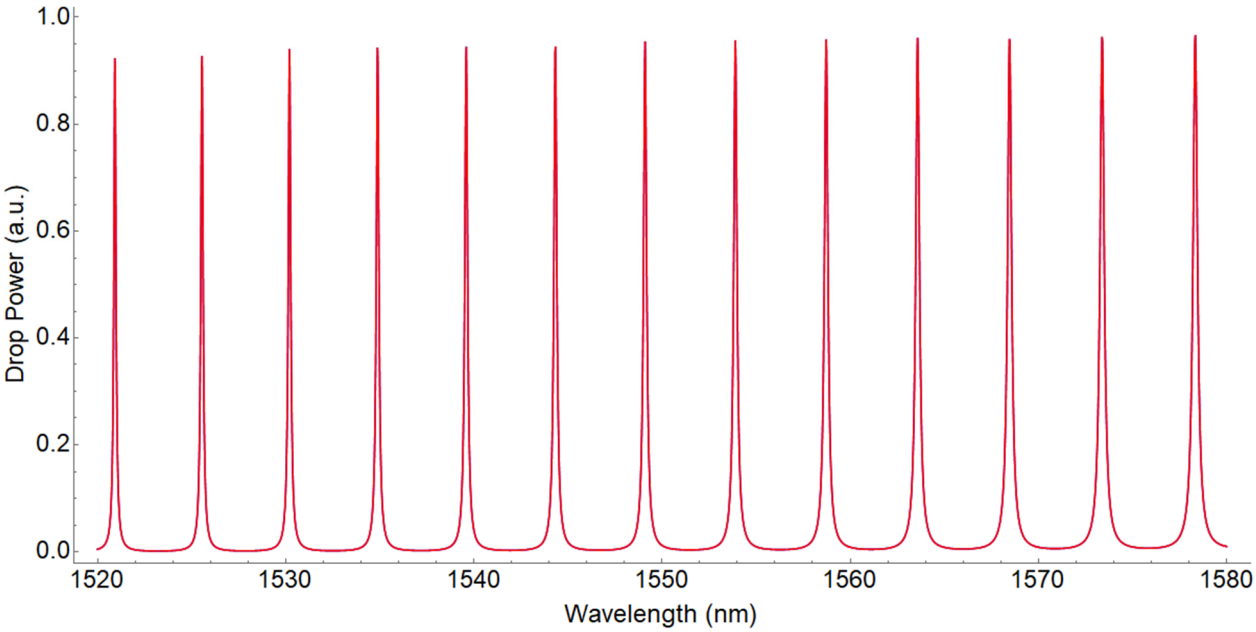

Fig. 2.17: Drop port output spectrum for a Si ring resonator clad by SiO_2 and Al_2O_3.

This spectrum is equivalent to the one in Fig. 2.15, but instead of notches, we now have transmission peaks. These are the characteristics that enable Si ring resonators to be used in applications such as passive routers and filters, because it is possible to direct a signal to a certain port based on its wavelength. By concatenating many resonators, it is possible to develop complex routing maps.

One interesting detail to observe in both output spectra, is that the Q factor tends to decrease with the wavelength (wider resonances), and the drop port output power increases. This is due to the waveguide dispersion. Since the effective index changes with the wavelength, this not only changes the phase difference accumulated in each roundtrip inside the ring, but also changes the coupling factor. In this example, n_{ef}(1520 nm) = 2.47, n_{ef}(1580 nm) = 2.41, κ(1520 nm) = 0.287, κ(1580 nm) = 0.405. This leads to $Q(1520) \cong 11500$ and $Q(1580) \cong 6000$.

A very interesting spectrum results from the case where internal rings are inserted in the system, as depicted in Fig. 2.18.

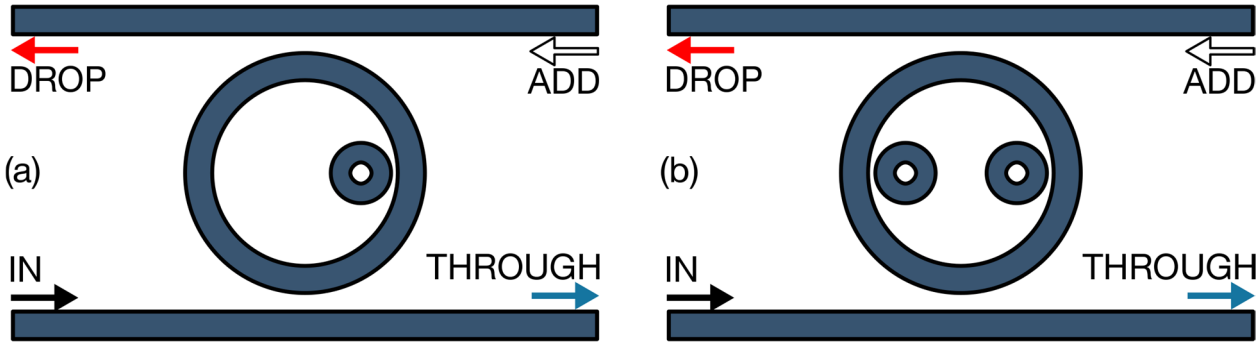

Fig. 2.18: Schematic of resonators with additional internal rings.

Mathematically, the problem is the same, but with additional matrices. We can think of the external ring as the bus waveguide for the coupling region to the internal rings. The matrices will not be shown here, but following the same procedure of (2.35) they are simple to obtain [70]. For both one and two internal rings with 5.5 μm of radius, separated from the external ring by 200 nm, the resulting spectra is shown in Fig. 2.19.

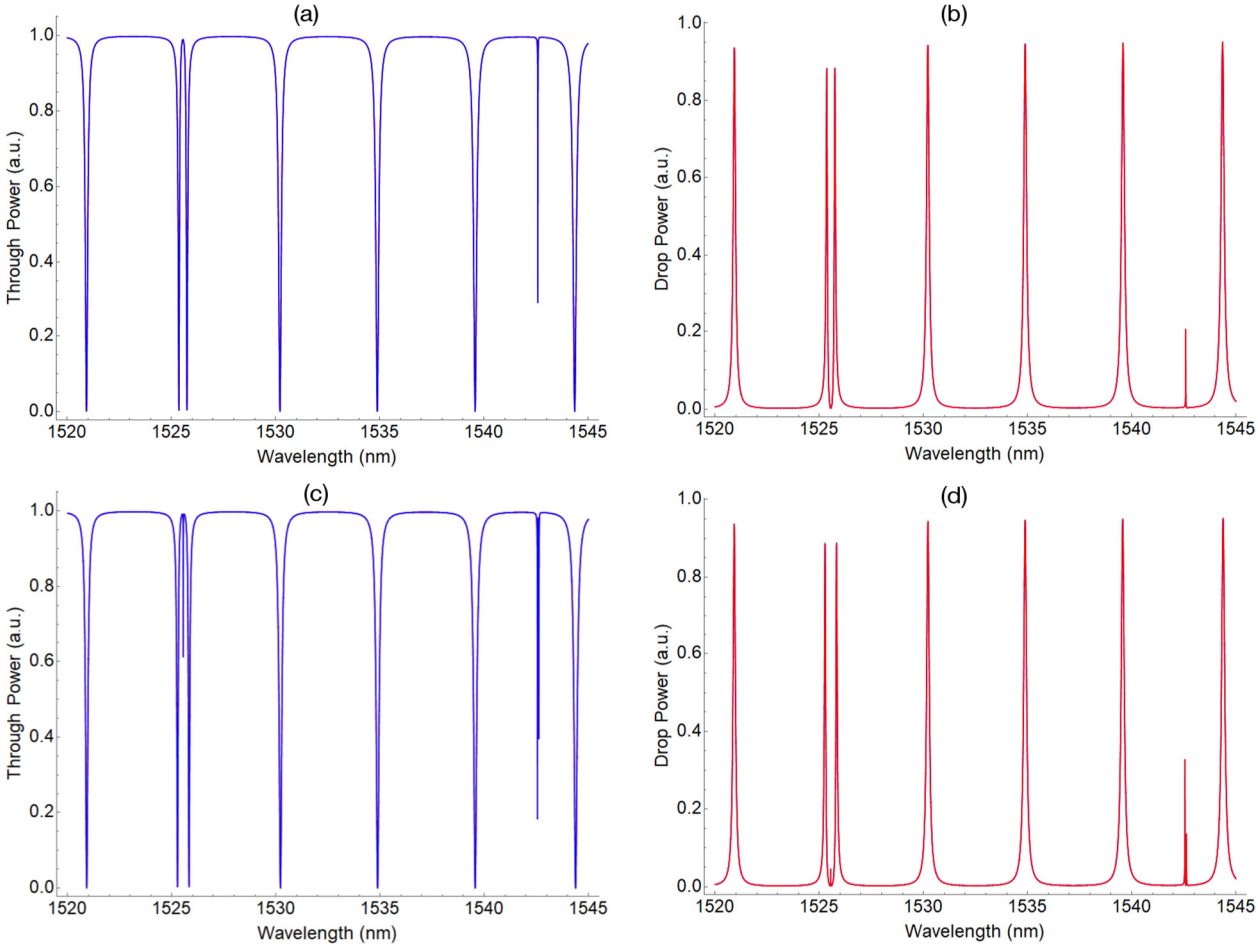

Fig. 2.19: Resulting spectra for one internal ring measured at the through port (a) and drop port (b), and two internal rings, also measured at the through (c) and drop (d) ports.

From Fig. 2.19a and Fig. 2.19b, we see that there are additional resonances, corresponding to the inner ring, with a higher Q factor (~100000) and lower extinction ratio/output power. The first one can be seen at ~1542.5 nm. Due to a Vernier effect, as the wavelength changes, the proximity to an external ring resonance also changes. At ~1525.5 nm they match exactly, and at that point, instead of one resonance, there is a split (doublet), and the Q factor is ~20000, higher than the single ring resonance. The width of this split is related to the coupling factor, or simply to the separation gap between the rings. The same happens when there are two internal rings (Fig. 2.19c and Fig. 2.19d). If they are exactly equal, split resonances corresponding to the two rings always exist, with a Q factor of ~100000. But when their resonance match that of the external ring, there is a triplet resonance, and the Q factor is greatly enhanced in the

middle one, reaching 150000 in the graphs shown. The asymmetry in the doublets of this case exists due to the drop port, which effectively inserts an additional loss before the wave reaches the second internal ring. The trade-off between the Q-factor and the drop port output power previously mentioned is evident here.

An interesting analogy is to think of a single resonator as a *quasi-atom*. In an atom, an electron is trapped around a proton, for example. If we combine more atoms together, we obtain molecules, and the energy levels corresponding to this combination can be complex, leading to energy levels splitting due to degeneracies. In this sense, the combination of more than one resonator can be called a *photonic molecule*. These devices are extensively studied for many applications that require specific spectral response, such as spectral engineering and signal processing [72] [73] [74] [75] [76] [77] [78].

2.5 Resonant Amplification

With valid models for both waveguide amplifiers and ring resonators, it is not difficult to join the two to describe how a resonator that contains gain media would perform. The link between them will be the coefficient defined in (2.24). By looking at (2.29), we see that the field amplitude changes exponentially when travelling in the ring resonator. In that case, we only considered losses, so we called it an attenuation coefficient. If we want to include the possibility of gain in addition to losses, all we need to do is substitute $-\alpha$ by ξ. This enables us to insert the result from (2.24) in (2.29). This coefficient should be calculated along the ring length, or the section of length the wave travels before arriving at the next coupling area. One limitation of this model, however, is that it doesn't take pump depletion into account. Nevertheless, since the pump is also resonant, for the cases that will be discussed it is a very good approximation.

For the waveguide of Fig. 2.10, considering that the cladding is Er-doped, we cannot simply use the confinement factor of the TE mode in (2.19) and (2.20), because the erbium interaction will not occur in the core. Thus, we define the overlap factor Γ as

the ratio between the energy contained in the top cladding and the total energy. For the waveguide in question and the wavelengths of interest, we obtain $\Gamma_{1550} = 0.43$, and $\Gamma_{1480} = 0.41$. By solving the amplification rate equations (2.19), (2.20) and (2.21), for a ring with 20 μm of radius and 2 dB/cm of loss, typical erbium cross-sections from Fig. 2.3 and concentration of $5\text{x}10^{20}$ cm^{-1}, the result is $\xi = 18.3$ m^{-1}. All that is left now is to insert this value in (2.29). Fig. 2.20 shows the results for the drop port output of one doped ring, when a signal of 1 μW (-30 dBm) enters the device, pumped by 10 mW (10 dBm) at 1480 nm.

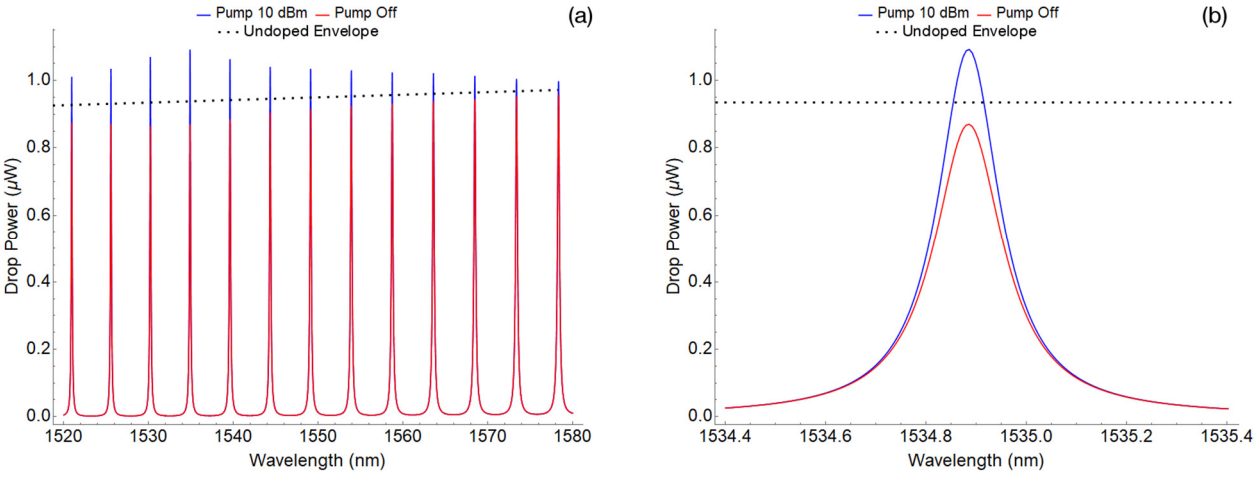

Fig. 2.20: Drop port output spectra for an Erbium-doped ring resonator. (a) Full spectra; (b) Zoom of the resonance at 1535 nm.

There are three conclusions that come from these results. The first, is that there is a clear difference between the pump off and pump on conditions. Since the output power is indeed higher than the input (1 μW), we can conclude that there is net gain, defined by:

$$G = 10\,log_{10}\left(\frac{P_{out}}{P_{in}}\right). \tag{2.36}$$

The second conclusion, is that this gain clearly depends on the wavelength, and is 0.38 dB at the highest point (1534.9 nm). Finally, the dotted line in the graphs represent the envelope of the drop port output in the undoped case (from Fig. 2.17). We can see that the doped cladding is a sufficient condition to insert additional losses.

However, this effect is reverted when the pump is turned on. This agrees with the amplifier model we developed, since the signal wavelength is also absorbed by Er^{3+} ions. To continue the analysis, we now calculate the gain for different pump powers at the 1534.9 nm resonance; and for each resonance with 10 dBm of pump power. The results can be seen in Fig. 2.21.

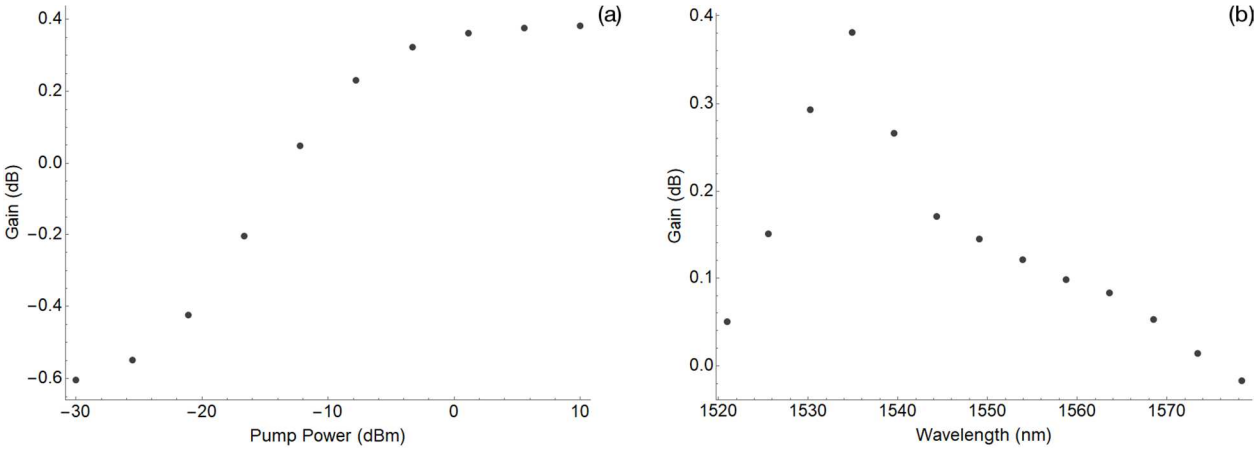

Fig. 2.21: (a) Gain in function of pump power for the 1534.9 nm resonance and (b) in function of wavelength for 10 dBm of pump power.

We can see that if the pump power is below -12 dBm, the signal is attenuated instead of amplified. As the pump power increases, net amplification now exists, up to the point where it saturates, at 0.38 dB, when a high fraction of the Er ions are already at the excited level. Observing the spectral gain from Fig. 2.21b, it is clear that it resembles the erbium emission cross-section spectrum from Fig. 2.3. This is expected, since it was used as input of the model, but also confirms that our models have been successfully coupled.

The only parameter left to analyze is the Q factor. After following the same procedure as the gain, the results obtained are the ones shown in Fig. 2.22.

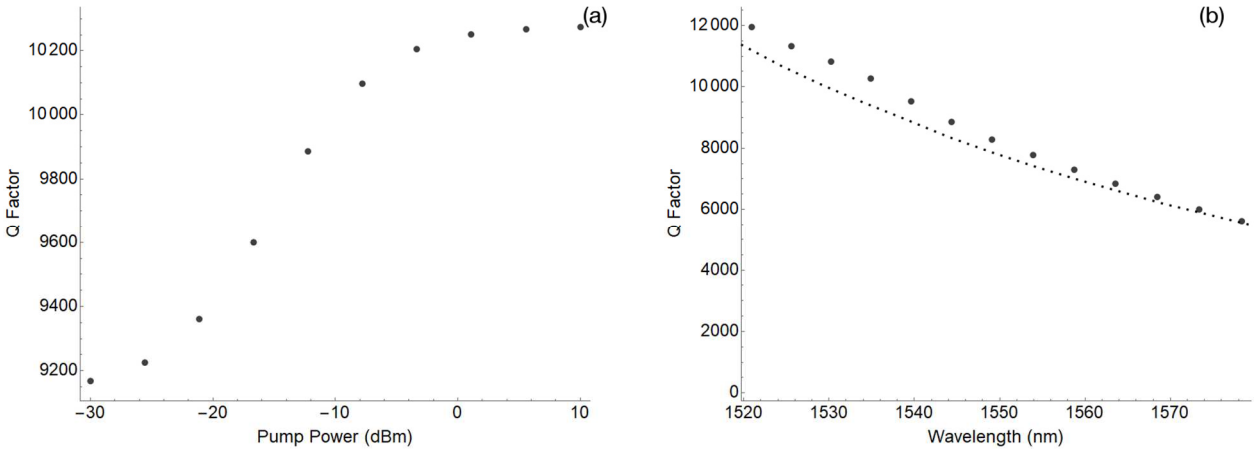

Fig. 2.22: Q Factor in function of pump power for the 1534.9 nm resonance (a) and in function of wavelength for 10 dBm of pump power (b).

We see that the Q factor increases as the pump power is increased, following the same characteristics of the gain curve. This is expected, since the Q factor is related to the dissipation of energy. If we have gain, or a loss decrease, the effective dissipated energy will also be decreased, thus increasing the Q factor. The Quality factor behavior versus the wavelength does not follow the Erbium emission cross-section curve as the gain does. As previously mentioned, due to differences in the coupling factor depending on the wavelength, the Q factor also varies, decreasing with the wavelength. This is indicated by the dotted line in Fig. 2.22b, corresponding to the spectrum of Fig. 2.17. The difference between the curves, however, should resemble the cross-section curve.

It is worth mentioning that all values and parameters used in all the simulations and calculations to obtain these results were based on realistic values. The gain obtained is not high compared to a state of the art EDWA (20 dB), but the intent of this device is to compensate routing losses. From what we calculated, if we consider 10 concatenated resonators composing a complex router (as the example from [24], and illustrated in Fig. 1.5c) the net loss could reach 3.6 dB (0.35 per resonator). Still not the worst obstacle faced by silicon photonics, but not a good figure of merit either. With our proposed method, it is possible to not only completely compensate this loss, but also

achieve 3.8 dB of gain in this router (0.38 per resonator), provided there is enough pump power.

2.6 Chapter Summary

In this chapter, the relevant theory of waveguides, optical amplification and optical resonators was reviewed, and together with the knowledge of key transitions in erbium ions, a functional model of a cladding gain media on Si ring resonators was developed. The next chapter details the first step to obtain an experimental demonstration of this concept: the development of Er-doped Al_2O_3 thin films and the respective optical (emission) characterization.

3. Erbium-Doped Al_2O_3 Films

The basis of all the work described here is the Erbium-Doped Al_2O_3 films. In this chapter, a detailed description of the deposition process will be given, in addition to the optimization of the surface quality, thickness, and optical characteristics, mainly the luminescence at 1530 nm.

3.1 Film Deposition and Characterization

Among the most common techniques for depositing Al_2O_3 films, we may mention Electron Beam Evaporation, Sputtering, Atomic Layer Deposition (ALD), and Plasma-Enhanced Chemical Vapor Deposition (PECVD) [79] [80]. It has been shown that to obtain Erbium-doped films, Sputtering is a very cost-efficient and straightforward process [81], and for this reason it was chosen as the method to develop our films.

As the name implies, a sputtering system grows thin films by ejecting atoms at high velocities from a source material, denominated target. An oscillating voltage (RF) is applied between two electrodes in a low-pressure inert gas (usually Argon) atmosphere, causing the atoms to collide and become ionized, generating plasma. The plasma ions have enough energy to remove atoms from the target, which are then ballistically ejected. A fraction of these particles is deposited on the sample surface, resulting in the growth of a thin film composed of the target material and possibly impurities from the gas atmosphere.

A 99.9% pure Al_2O_3 target was used to create the alumina films. To obtain Er-doped films, 99.9% pure erbium pieces were used in conjunction with the main target. This procedure, also called Co-Sputtering, is illustrated in Fig. 3.1. Although low-cost and straightforward, one drawback of this technique is that it is not trivial to control the dopant concentration.

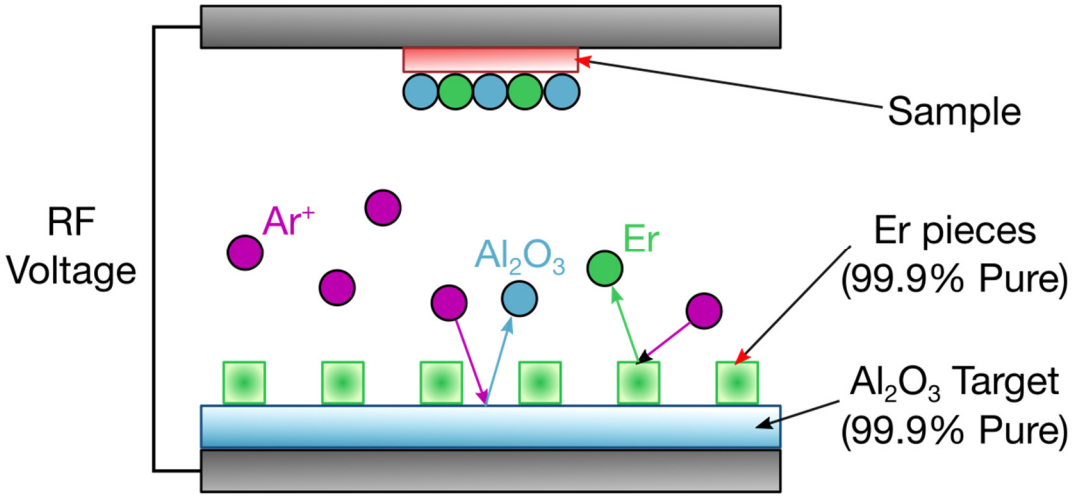

Fig. 3.1: Schematic of the Co-Sputtering technique.

In the used sputtering system, it is possible to control the bias voltage, sample temperature, and the relative flow of a secondary gas. To study how these parameters influence the resulting film, several depositions on glass slides were performed by the Photovoltaic Research Lab's (LPF) researcher Rafael Merlo, in an Argon atmosphere with $6x10^{-3}$ mbar ($2x10^{-6}$ mbar of base pressure), varying each one systematically and measuring the film thickness and refractive index. These measurements were made using a Veeco Dektak 3 ST Profiler and a Rudolph FTM-STD Ellipsometer, respectively. The results for each parameter combination are summarized in Table 3-1.

Table 3-1: Thickness and refractive index of the films for different deposition parameters.

#	Bias (V)	Time (h)	O_2 (% of Ar flow)	Sample Temp. (°C)	Thickness (nm)	Refr. Index
1	150	2	10	200	55	1.61
2	650	2	10	200	125	1.61
3	1000	2	10	200	275	1.61
4	1000	4	10	200	480	1.61
5	1000	6	10	200	620	1.61
6	1000	4	5	200	500	1.61
7	1000	4	1	200	650	1.61
8	1000	4	1	250	630	1.63
9	1000	4	1	300	580	1.66

The goal of this experiment was to obtain a film with the highest refractive index and thickness possible. We observed that by increasing the bias the refractive index was not affected, but resulted in a higher thickness. This occurs because the ions impact

the target with a higher energy, increasing the probability of particle ejection. By decreasing the system standard secondary gas flow (O_2 for oxide depositions) from 10% to 1% of the Argon flow, there was an additional increase in the film thickness, but no change in the refractive index, due to the higher-purity plasma. The last parameter, the sample temperature, influenced the refractive index and thickness, resulting in a higher index but lower thickness for higher temperatures. The molecules that compose the film have a presumably higher mobility in this condition, and if the resulting film has voids, they will be minimized and the overall thickness can decrease. Voids in the film also reduce the refractive index, so a higher value is an indication of the film quality. For this reason, the parameters from deposition #9 were the ones used in subsequent depositions, resulting in a suitable film thickness and the highest refractive index.

3.2 Optical Characterization and Thermal Annealing

The next step in the development of the Al_2O_3:Er films is the luminescence characterization. To this end, we performed photoluminescence (PL) measurements on samples containing the doped film. The experimental setup for this is illustrated in Fig. 3.2. A LaserLine iZi high-power (200 mW, CW) pump laser at 532 nm is modulated by a SRS 540 Chopper Controller, then absorbed by the sample after a beam diameter adjustment. From the transition $^4I_{15/2} \rightarrow {}^2H_{11/2}$ in Fig. 2.1b, we can see that this wavelength is adequate for pumping the doped film, since it is possible to detect photon emission at various energy levels, including the 1550 nm region, during the Er^{3+} ion energy decay. The emitted light is focused inside an Oriel Cornerstone 260 Monochromator, and the wavelength filtered output is subsequently detected by a cooled high-sensitivity Oriel 71893 Photodiode, its temperature controlled by Oriel 77055 Temperature Controller. The signal is then monitored by an EG&G 5210 Lock-in

Amplifier. The reason for modulating the measurement (at 277 Hz) is to mitigate external light interference, since the lock-in only measures signals with the modulated frequency.

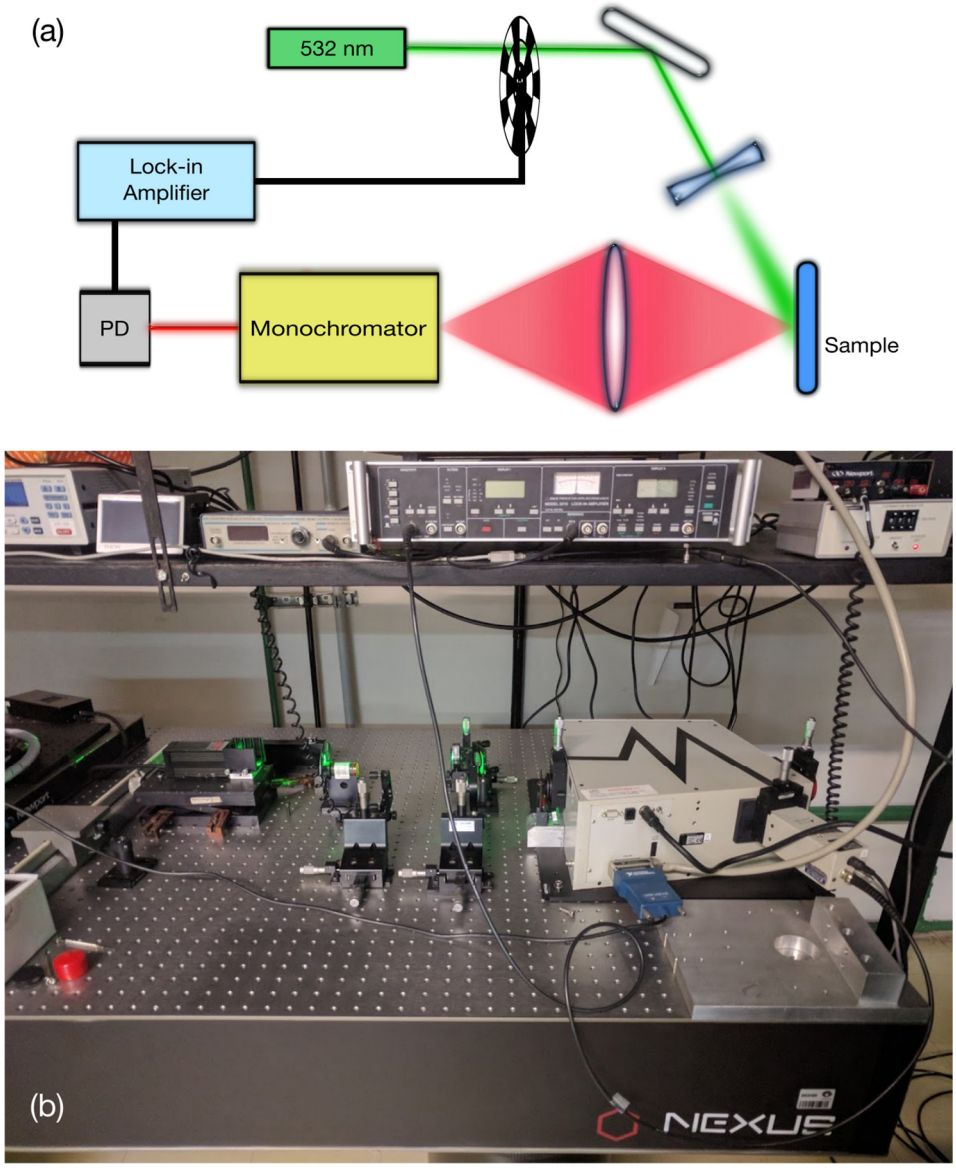

Fig. 3.2: Schematic (a) and photograph (b) of the photoluminescence measurement experimental setup.

By varying the monochromator wavelength, we obtain the luminescence spectrum of the sample. For a typical fabricated film, the normalized spectrum is shown in Fig. 3.3.

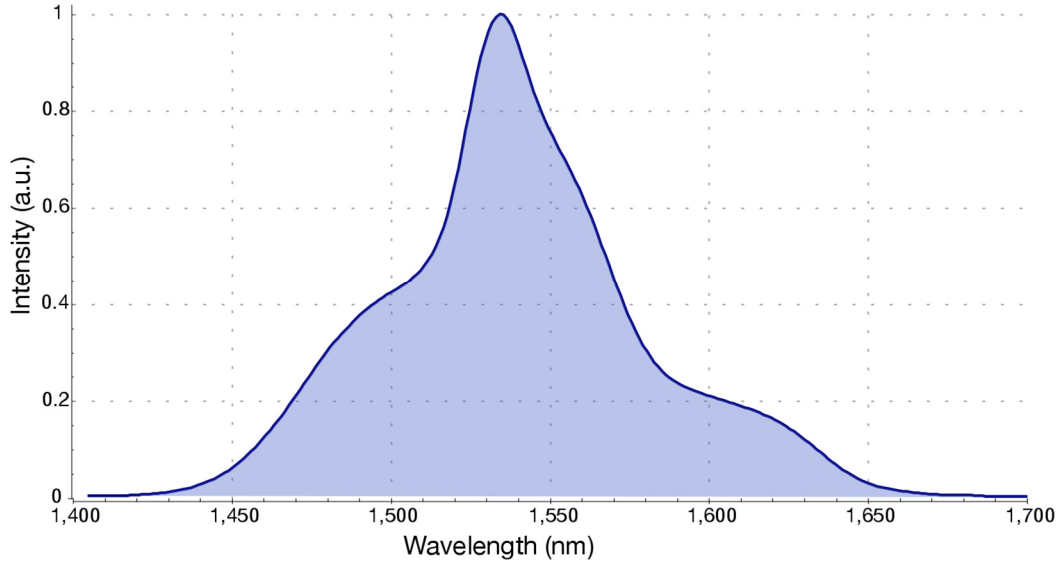

Fig. 3.3: Typical photoluminescence spectrum for the measured films.

This curve closely resembles the erbium emission cross-section. This shows that the Er^{3+} ions incorporated in the film are being successfully excited and are decaying spontaneously, with a higher probability to emit photons at 1535 nm. Nevertheless, the overall intensity of the emission can be further increased by performing a thermal annealing on the film, to activate Er ions and remove remaining voids, defects, and impurities. To this end, doped films were deposited on several samples, which were then subject to thermal annealing for 30 minutes in a N_2 atmosphere, at different temperatures. By measuring the PL spectrum for each of these samples, we determined the optimal temperature regarding the luminescence intensity. The results, normalized by the pump laser reflection power, are shown in Fig. 3.4.

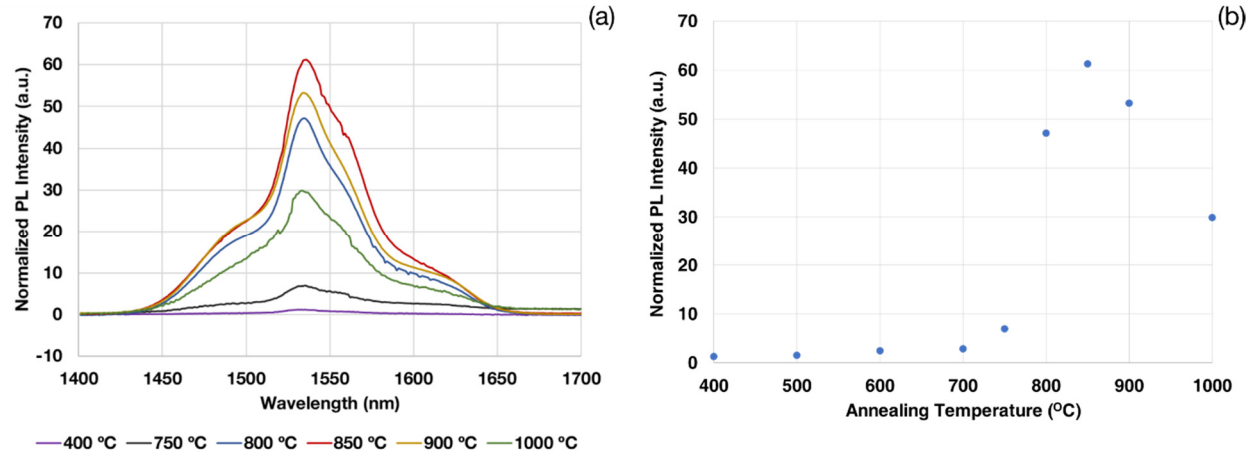

Fig. 3.4: (a) Photoluminescence spectra of Al_2O_3:Er films for different annealing temperatures. (b) Peak emission power in function of annealing temperature.

From Fig. 3.4a, we observe that as the annealing temperature increases, so does the overall emission intensity, up to 850 ^{O}C. For higher temperatures, the emission starts to decrease. This is evidenced in Fig. 3.4b.

We then proceeded to study how the time and annealing atmosphere affect the resulting performance. Different samples were subject to thermal annealing at 850 ^{O}C, for different times (10, 30 and 60 min) and atmospheres (N_2, O_2, ambient air), and the results are plotted in Fig. 3.5.

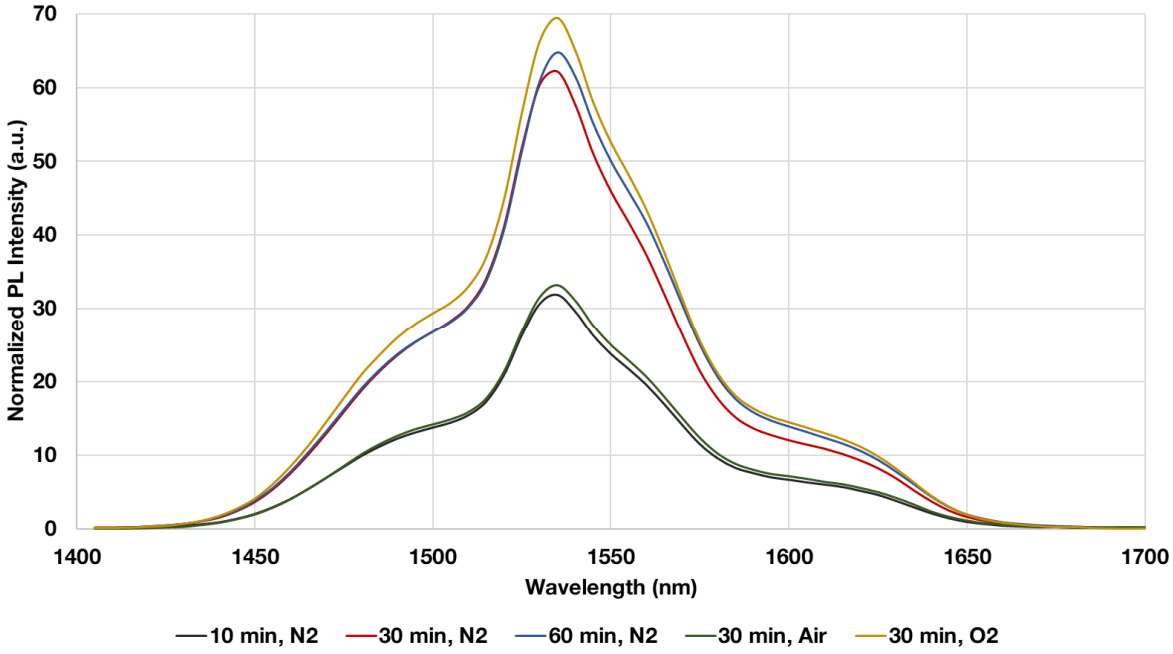

Fig. 3.5: Photoluminescence spectra of Al_2O_3:Er films for different annealing conditions, at 850 ^{O}C.

From the resulting spectra, we conclude that 60 minutes of annealing time produces the best emission results, although the increase in peak emission is only 5%. If no controlled atmosphere is used on this process, the emission decreases 45%, but changing the gas to O_2 actually increases the emission by 13%. This is due to the fact that impurities from the ambient atmosphere are aggregated into the film, so a controlled environment should always be used. Additionally, using an O_2 atmosphere helps reposition any oxygen atoms that may be expelled from the oxide during the process.

As mentioned before, high temperatures can remove gaps, defects, and impurities from the film. This process should affect the refractive index as well, so it is important to measure this value after the annealing. Using ellipsometry, the refractive index was measured at different areas of the annealed samples, resulting in an overall increase, but at the cost of film uniformity, as demonstrated in Fig. 3.6.

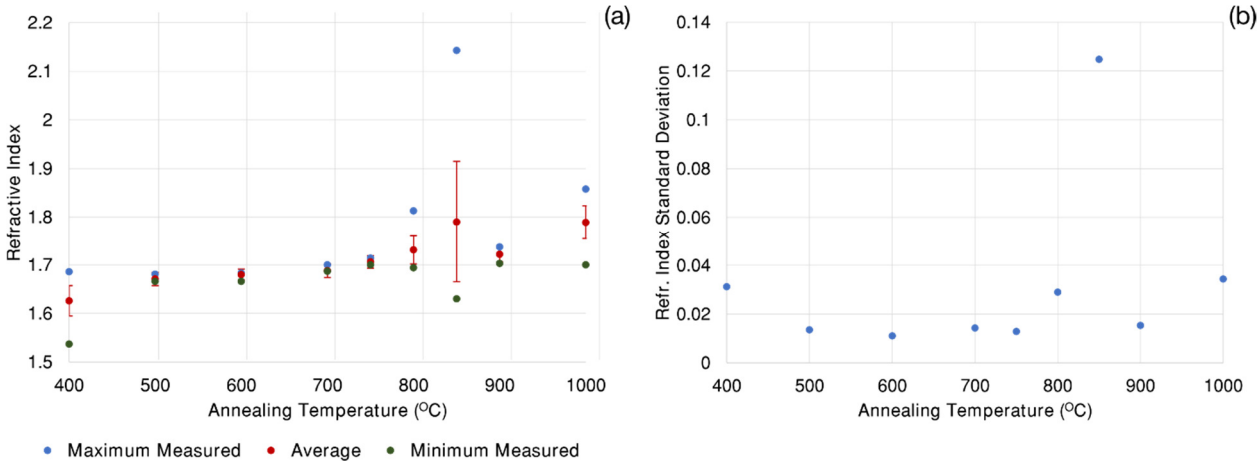

Fig. 3.6: Refractive index (a) and standard deviation (b) in function of annealing temperature.

The refractive index increases after the annealing process, reaching values as high as 2.1 for 850 ^{O}C, and decreases for higher temperatures. However, the variance on different regions of the sample also increases, peaking at this same temperature. This is mainly due to microcrystalline Al_2O_3 structures beginning to form in certain areas, whereas at higher temperatures the coverage of these structures increases [79]. To verify this, Atomic Force Microscopy (AFM) images of the samples were acquired using a Nanosurf EasyScan2 FlexAFM, and the most illustrative results are displayed in Fig. 3.7.

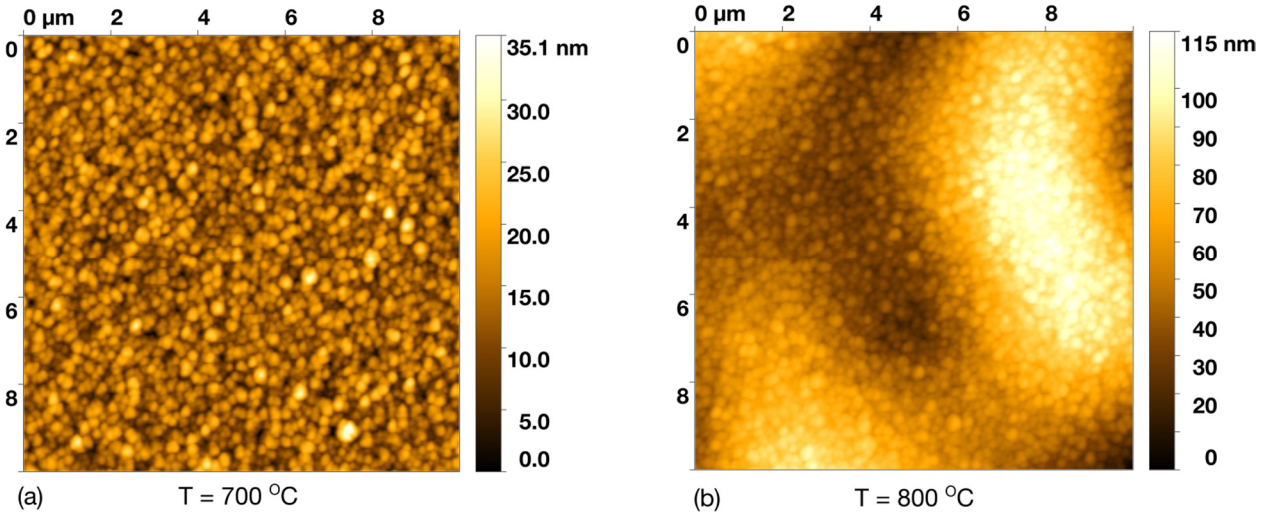

Fig. 3.7: AFM images for Al_2O_3 film samples annealed at 700 ^{O}C (a) and 800 ^{O}C (b).

For annealing temperatures below 700 ^{O}C, although presenting a high granularity, the films are relatively uniform, with a root-mean-square (RMS) roughness of 4.12 nm. For 800 ^{O}C, however, it is possible to measure a higher non-uniformity, and the local RMS roughness increases to more than 20 nm (21.90 nm on the pictured case). For higher temperatures, the film was considerably damaged, and thus no AFM images were successfully acquired. This indicates a severe film degradation, possibly due to gaseous blisters erupting violently when subject to high temperatures, surpassing the reflow capability of the film that, as mentioned, starts to crystallize at 800 ^{O}C. An optical microscopy photo comparing a sample annealed at 750 ^{O}C and another at 1000 ^{O}C is shown in Fig. 3.8.

Fig. 3.8: Microscopy photo of a sample annealed at 750 °C (left) and another at 1000 °C (right) side by side.

Several triangular crystalline clusters can be observed on the left-side sample (750 °C), evidencing the beginning of the crystallization due to the thermal annealing. On the right-side sample (1000 °C), these structures cover the entire area.

With this, a trade-off between film quality and emission strength exists. For all subsequent Er-doped film depositions, the thermal annealing process was defined to be at 800 °C, in O_2 atmosphere, for 60 minutes.

3.3 Chapter Summary

The procedure to obtain Er-doped Al_2O_3 thin films suitable as the top cladding layer of a silicon photonics device has been detailed, and the fabrication procedure refined in order to optimize the film's light emission at the 1520 nm – 1560 nm range (C-band). The application of these films in Si ring resonators and the resulting reduction in optical losses will be demonstrated experimentally in the next chapter, where the microring fabrication procedure and characterization experiments will also be described.

4. Silicon Ring Resonators with Er-Doped Al_2O_3 Cladding

After having developed an optimized Er-doped Al_2O_3 film and a complete model of our device, the next step is to verify the concept of compensating insertion losses in silicon photonics devices based on ring resonators. This chapter will start with a summary of the fabrication procedure of silicon ring resonators (and photonic molecules) with Er-doped cladding. The performed measurements will also be presented and the results discussed, confirming the proposed idea. To finish, an analysis of special design cases that can further improve the intended performance will be given.

4.1 Fabrication Process

We have previously mentioned that one of the advantages of using an Er-doped cladding is that the fabrication is C-MOS compatible, and can benefit from the availability, relative low-cost, and production scalability of commercial foundries. These facilities use Silicon-on-Insulator (SOI) wafers, obtained by bonding two wafers together, to create 220 nm x 450 nm silicon waveguides clad by SiO_2 [82].

To fabricate the intended devices within the thin Si layer, optical or electron-beam lithography techniques can be used. Although e-beam lithography offers a higher resolution (below 10 nm) [83], silicon-photonics foundries employ deep UV lithography, with 200 nm resolution. Taking advantage of the well-established C-MOS technology, optical lithography presents a very high scalability, since the pattern recording is parallel instead of serialized.

To illustrate the UV lithography procedure, Fig. 4.1 shows the steps involved in the fabrication, using a ring resonator as an example pattern.

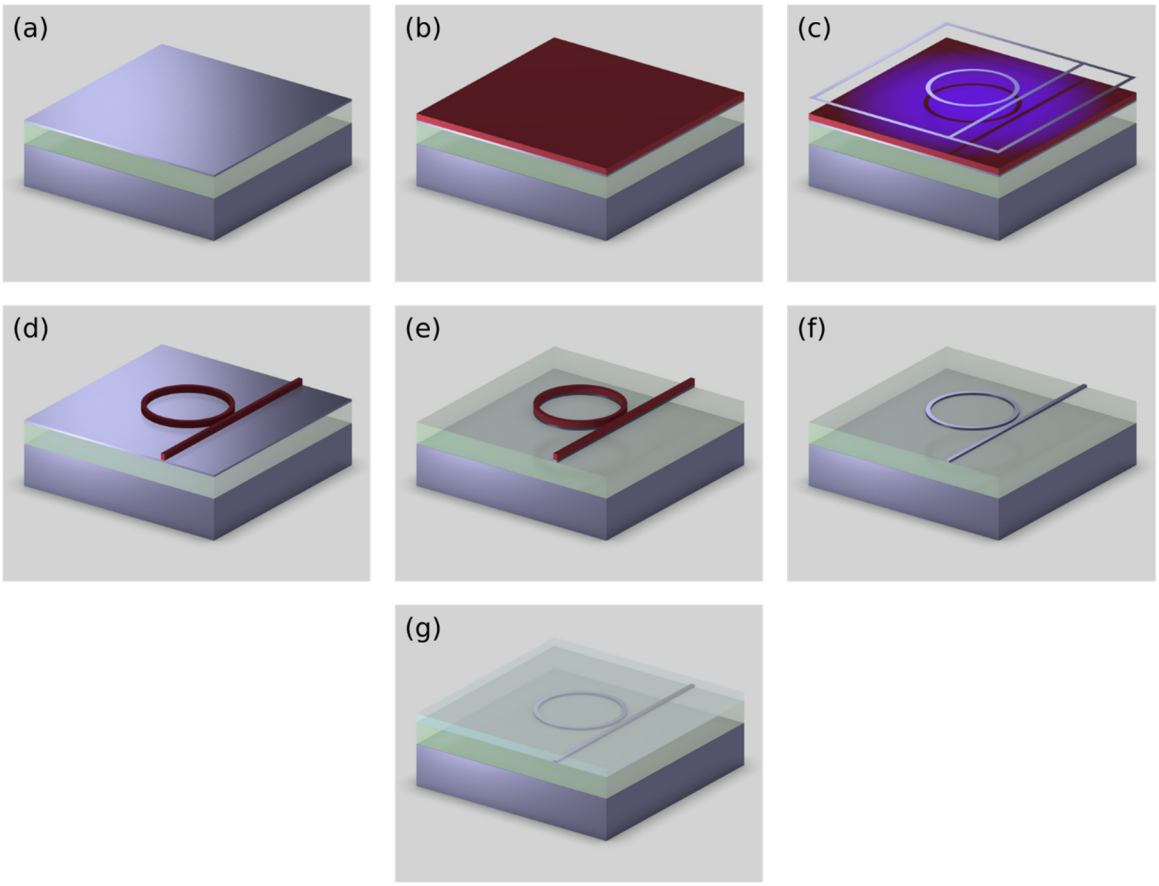

Fig. 4.1: Optical UV litography. (a) Initial sample. (b) Resist deposition. (c) Exposure. (d) Resist developing. (e) Si etch. (f) Resist removal. (g) Top cladding deposition and finished sample.

Starting with a SOI sample, the first step is to deposit a photosensitive colloidal solution (photoresist) on top of it (Fig. 4.1a and Fig. 4.1b). A thermal treatment is responsible for the monomers chemical bonding, forming a polymer. When subject to light with sufficient energy, these bonds are broken and the substance becomes soluble on a developing (alkaline) solution. Thus, by using an opaque mask with the desired pattern, it is possible to transfer this pattern to the polymer. When exposed to UV light (Fig. 4.1c), the region shadowed by the mask retains its integrity, while the remaining area is sensitized. Using the alkaline developing solution, the exposed portion is then completely removed, and only the pattern remains (Fig. 4.1d). It is important to notice that the photoresist described in this example is known as a positive resist. There are also negative resists, in which the exposed area is strengthened, and the pattern is removed during the developing.

The purpose of these steps is to create a protective layer on top of the silicon. When the sample is etched (acid solution or plasma dry etch, Fig. 4.1e), the photoresist covering the Si will remain, and the pattern will then be transferred to the Si layer after the photoresist is removed (with acetone and/or O_2 plasma, Fig. 4.1f).

The last step is to deposit the top cladding on the sample. Typically using Plasma-Enhanced or Low-Pressure Chemical Vapor Deposition (PECVD or LPCVD), a 1 μm layer of SiO_2 finishes the device (Fig. 4.1g).

Although the procedure for optical lithography has been detailed, e-beam lithography utilizes the same principle, but instead of a photoresist, the polymer is an *electroresist*, exposed to a moving electron beam.

To obtain our coupled ring resonator (photonic molecules) samples, it is necessary to design the lithography mask to be used in the fabrication. For this work, the samples were fabricated by IMEC, a Si-photonics foundry located in Belgium. The file format requested by the facility is GDSII, a format capable of storing geometries, text, and layouts hierarchically. Several rules have to be followed during the design, and the waveguide height is fixed at 220 nm. With this constraint, the waveguide width was chosen to be 450 nm, resulting in single-mode behavior in the C/L bands for the TE mode.

Former PhD student Luis Barea designed the photonic molecules devices used in this work, to be thoroughly studied and applied to signal processing and optical communications. For that, the radii were set at 20 μm and 5 μm for the outer and inner rings respectively, and the separation gap was chosen to be 200 nm, the same dimensions as the ones used for the calculations in section 2.4. The resulting mask design for the devices of interest can be seen in Fig. 4.2 [84].

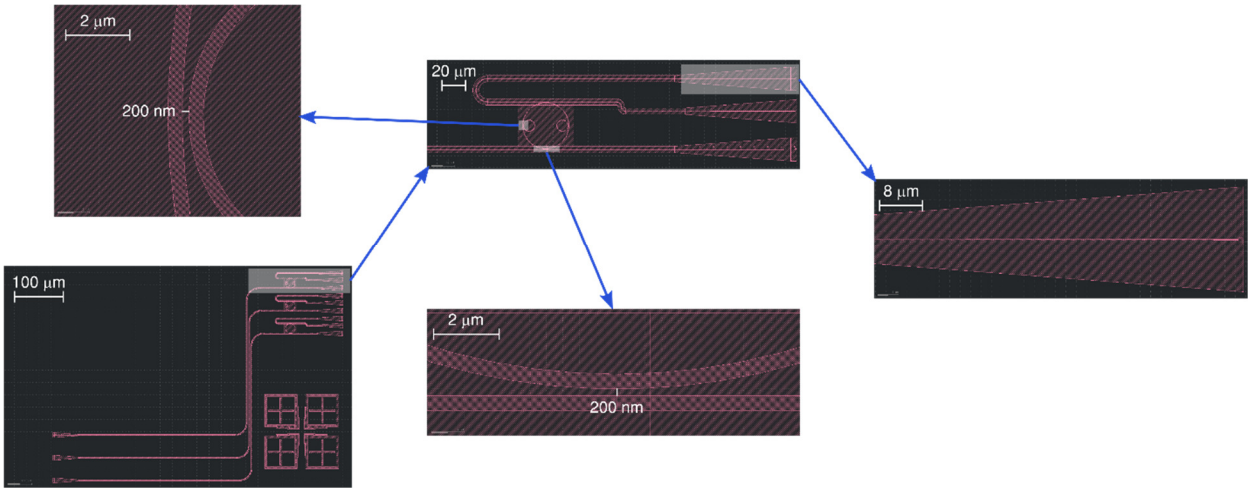

Fig. 4.2: Designed mask sent to IMEC foundry, containing only the devices of interest for this work. Relevant regions are shown with a higher magnification.

To maintain structural integrity and a regular exposure dose along the entire wafer, 1 µm x 1 µm squares are posteriorly added to the blank spaces. Thus, the mask must be two-layered: the first one containing the waveguides (cross hatched areas), and the second containing a "cover" of our entire design, where these squares should not be present (diagonally hatched areas). This procedure also increases the fabrication repeatability.

It is important to notice that at the extremities the waveguides acquire a tapering shape, shown in the rightmost part of Fig. 4.2. This feature is called an inverted taper, and is responsible for the coupling between the waveguide and the input/output fibers. As light travels from the waveguide along the taper, the propagation mode area increases, as light is progressively less confined. For a tip width of 100 nm, the TE mode from the taper and the input/output fiber should match at a certain distance, increasing the coupling efficiency. The development of this coupling can also be seen in more detail in [84].

With the mask properly designed, the foundry manufactures the chips using a similar procedure as the one illustrated in Fig. 4.1, called projection optical lithography

[85]. The result is a complete Si wafer cut into several samples with the submitted mask patterns. One example of the received samples can be seen in Fig. 4.3.

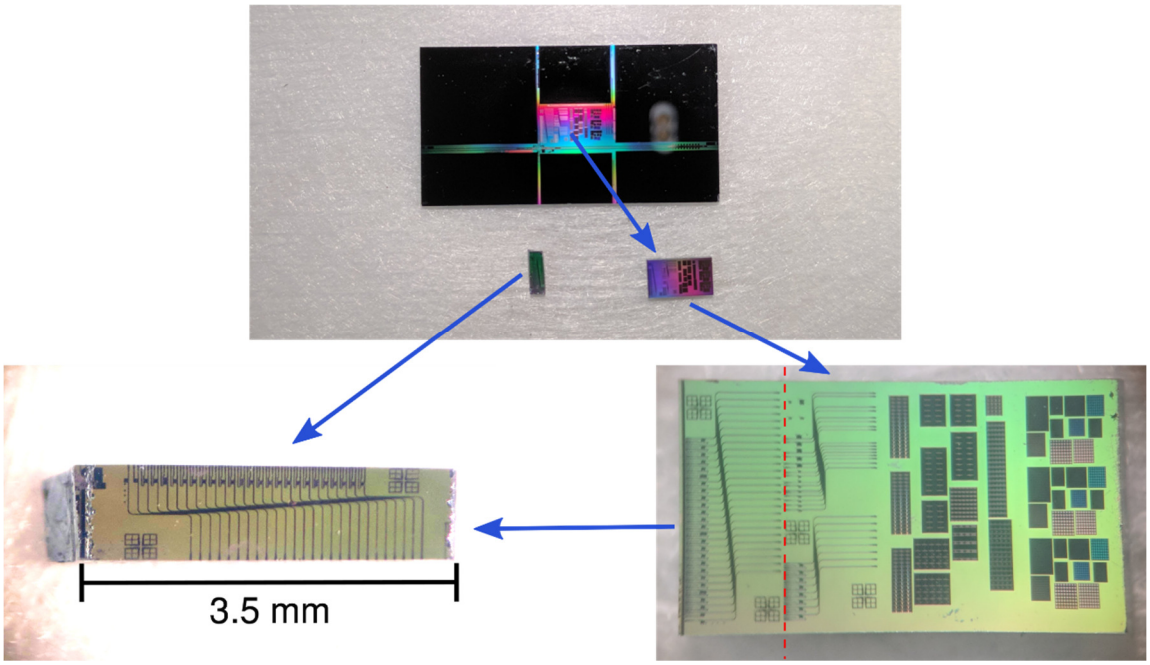

Fig. 4.3: Example of a sample received from the foundry. Since there are different projects on the same chip, it is necessary to cut the desired area.

As shown, the area of interest of the sample is contained within a small region in the center. To separate the chip from the unwanted surrounding material, it is necessary to cut that piece out. This was done at the CTI Renato Archer, using the LPKF ProtoMat S103 Circuit Board Plotter, resulting in the bottom right chip from Fig. 4.3, possessing an area of 6.0 mm x 3.5 mm. This sample, however, is still not ready for the photonic molecules characterization, since there is no access to the tapered waveguides. Additionally, it is usual for a chip layout to contain multiple projects and devices, thus a second cut is necessary, which results in the 3.5 mm x 1.2 mm sample in the bottom left of Fig. 4.3.

Due to the coarse nature and inadequate precision of the cutting process, it has to be executed at a safe distance from the waveguides. The resulting edges possess very high roughness, and a polishing procedure is needed not only for smoothing the surface, but also trimming the sample, until the tapered waveguides tips are exposed at

the sides. This step has been performed on all measured samples, using an adapted Ultratec FFTx Portable Fiber Polisher. This equipment is shown in Fig. 4.4a and Fig. 4.4b.

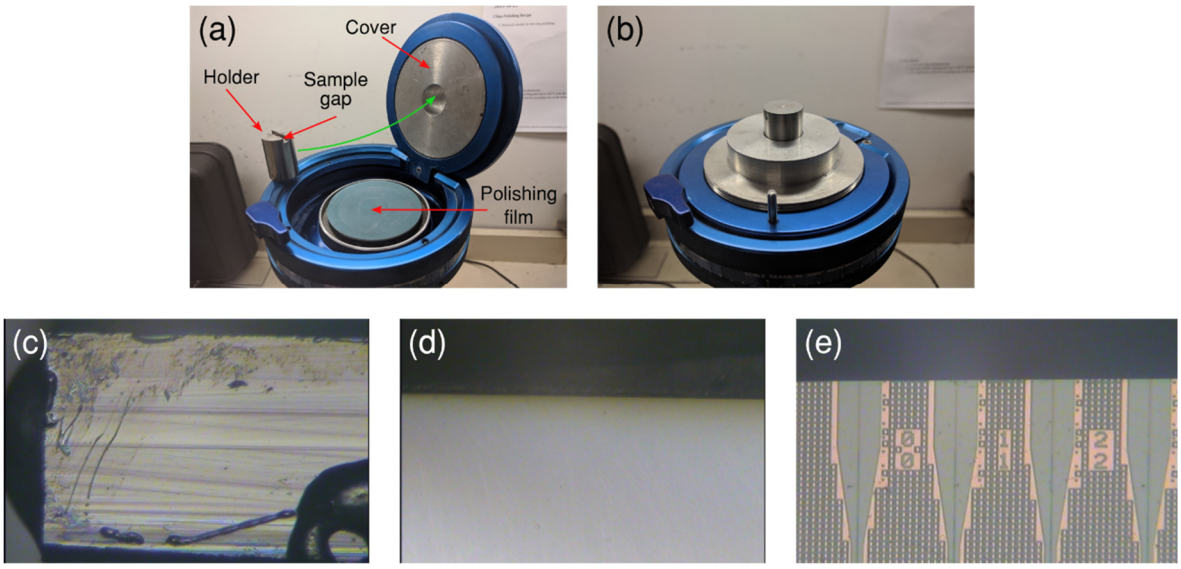

Fig. 4.4: Polisher used to trim and reduce the chip faces roughness (a, b). Side view of one of the chip's faces before (c) and after (d) the polishing. Top view of the tapered waveguides after the polishing (e).

We modified the sample holder, originally for fiber connectors, to accommodate a chip. An aluminum disk with a 1.5 cm wide circular hole is fixed to the polisher's cover. The sample is glued to a small gap in a stainless-steel cylinder with 1.5 cm of diameter, using crystal wax, a polymer that has a relatively low melting point, but is solid at room temperature. By heating the cylinder holder to 90 ^{o}C on a hot plate, it is straightforward to place the sample in the gap, so that one of the faces (at a time) exceeds the cylinder height. After cooling down to room temperature, the cylinder is inserted into the cover hole, and the sample is ready to be polished. For the optimal trimming rate and resulting roughness, several polishing films were employed sequentially, from 9 µm to 0.5 µm of granularity. An example of a chip side before and after polishing can be seen in Fig. 4.4c and Fig. 4.4d. On Fig. 4.4e, it is possible to view the top of the chip after the polishing procedure, with the tapered waveguides at the edge of the sample. Also visible in Fig. 4.4e are the squares added by the foundry to the empty areas of the design.

The procedure described thus far is enough to prepare a silicon chip for characterization. For our purposes, however, post-processing is necessary, to replace the top cladding with the Er-doped Al_2O_3 film. To do that, the SiO_2 film on top of the chip must be removed from the desired areas, as illustrated in Fig. 4.5a through Fig. 4.5c. The first etch design covers the whole devices, while the second covers only the inner rings. The coupling regions are not etched. The purpose of these two designs is to isolate the effect of each ring (outer or inner) on the spectrum, while at the same time preventing excess amplified spontaneous emission (ASE) at the bus waveguides.

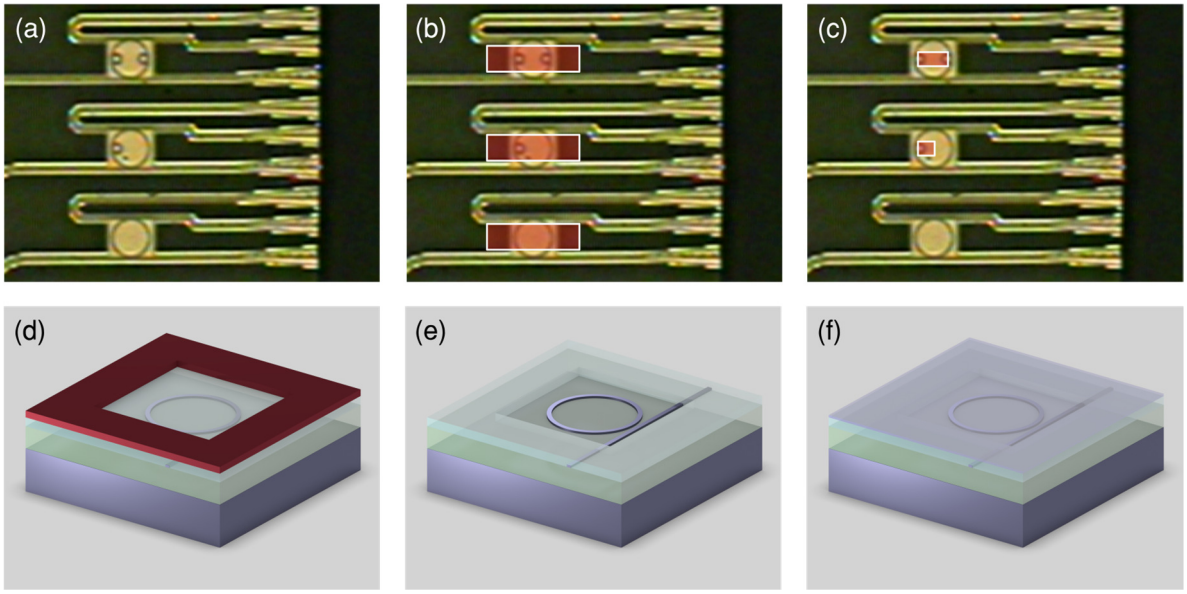

Fig. 4.5: Pictures of part of a ready sample before the cladding etch (a), and indicating the areas to be etched (b, c). Lithography process illustrations for the top cladding etch, showing the photoresist pattern (d), etched cladding (e), and finished sample, with the Al_2O_3 cladding deposited (f).

To etch and deposit the films, optical lithography has been employed following the standard procedure previously described (illustrated in Fig. 4.5d through Fig. 4.5f), using the MJB-3 optical lithography system. The etching was performed by submerging the chips in a buffer hydrofluoric acid (HF) solution for a total time of 6 min, with intervals at every 1 min for depth verification using a Veeco/Sloan Dektak 3ST Profiler. From the measured depth data, Fig. 4.6 was created to illustrate the etching procedure.

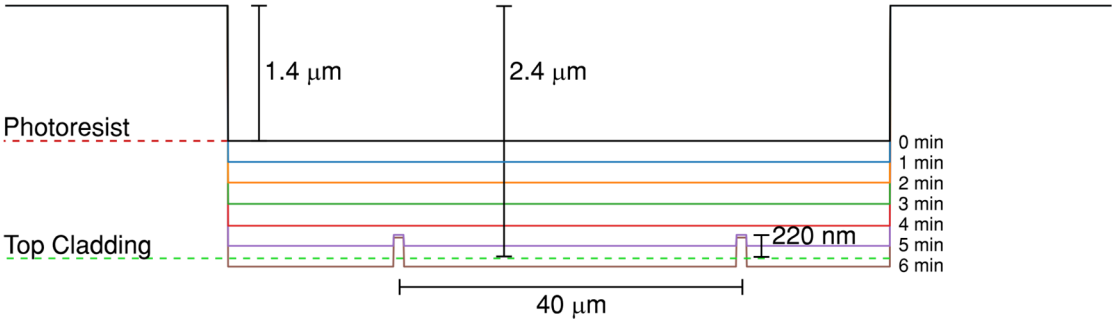

Fig. 4.6: Illustrative representation of the etching procedure, for each 1 minute step.

Finally, the last step of the fabrication process is the deposition of the Al_2O_3 films (both Er-doped and undoped) on top of the samples. Besides the etched ones, these films were also deposited on top of chips shipped without the top claddings. The procedure for the deposition is the same described in Chapter 3, and Fig. 4.7 shows the SEM image of the cross-section of an early sample after this step.

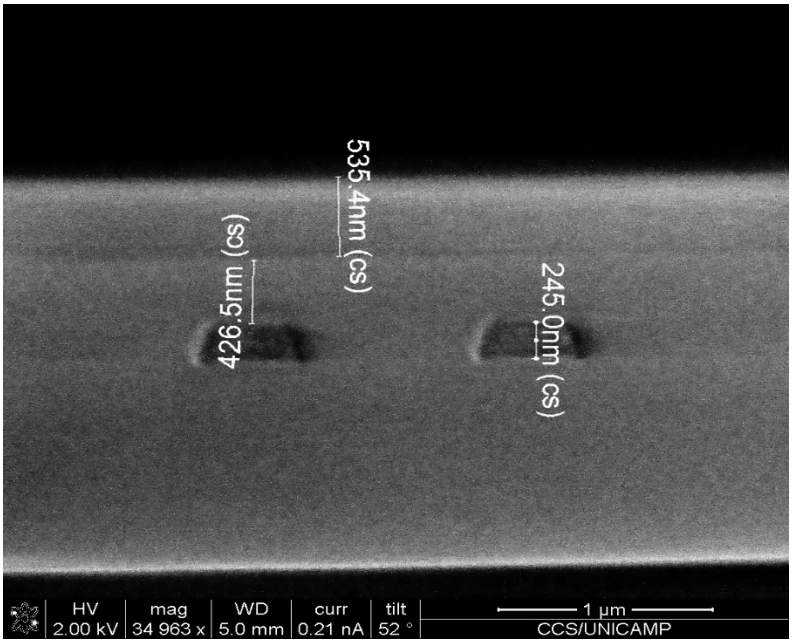

Fig. 4.7: SEM image of the cross-section of a resonator, with a clear interface evidencing two layers of the top cladding.

An important detail from Fig. 4.7 is the clear interface in the top cladding, along with the measured heights. This is evidence for the existence of two top cladding layers, which in turn indicates an unfinished etch. On this sample, the etching procedure was not monitored, and the waveguides were consequentially not exposed. The reason to

monitor this procedure as illustrated in Fig. 4.6 is to ensure complete exposure of the Si waveguides, so the maximum overlap factor (as described in section 2.5) can be achieved. Thus, it would be expected that this sample performs very similarly to a resonator with standard SiO_2 cladding.

Since HF also corrodes Si (at a lower rate), if the sample is etched for a longer time than necessary, it is possible that the waveguide height is slightly decreased as well. This shows that this step is critical, so extra care is needed for a good resulting device.

4.2 Characterization

Ring resonators, as discussed in section 2.4, are mainly characterized by the transmission spectra at their different input/output waveguides, such as the through and drop ports, for example. Aside from the insertion loss (for the drop port) and extinction ratio (for the through port), the quality factor (Q) and free spectral range (FSR) are quantities that describe the component spectral characteristics. These can be obtained directly from the respective spectrum measurements, using the experimental setup shown in Fig. 4.8.

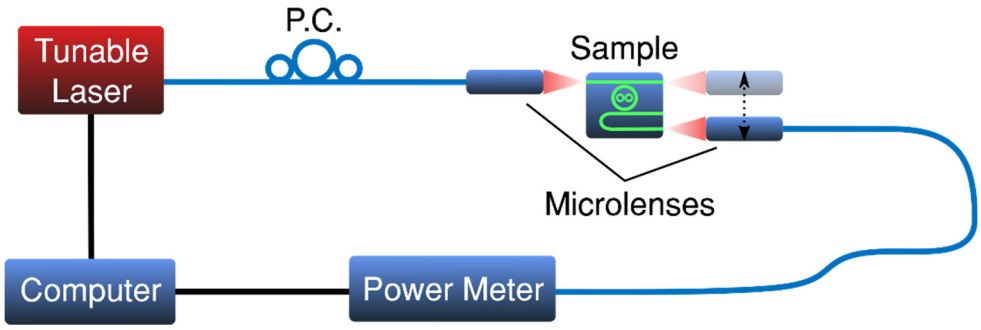

Fig. 4.8: Experimental setup for the initial ring characterization.

Lensed fibers are used to couple light in and out of the chip, through the tapered waveguides. On the output, these can be moved to couple light from the through or drop port. Since we are not interested in adding channels to be measured at the through port, the add port is not used. The light from a tunable laser (Agilent 81940A) passes through the device, and the output is measured on an Agilent 81636B Power

Meter, connected to a computer via a 16-bit National Instruments DAQ with a maximum sampling rate of 1 MHz (10 kHz was used, to avoid large files). A polarization controller (rotator) (P.C.) is placed before the input lensed fiber to ensure optimal coupling (since the tapered waveguide is designed for the TE mode).

Seeking the maximum output power, the optical alignment of the lensed fibers is performed using a ThorLabs NanoMax 3-axis Stage for each fiber, with piezoelectric actuators for higher precision (up to 5 nm). The output spectrum can thus be obtained at each port by continuously sweeping the laser wavelength. The coupling loss strongly depends on the polishing procedure, and typical values range between 5 dB and 8 dB for each side. These values are determined by the output power subtraction from the input power. This gives us the net loss, however, and it is not possible to distinguish the individual value for each side (or the propagation losses) using this method.

For a standard SiO_2-clad single ring, with 20 μm of radius, separated from the bus waveguides by 200 nm, the following spectra were obtained for the through and drop ports:

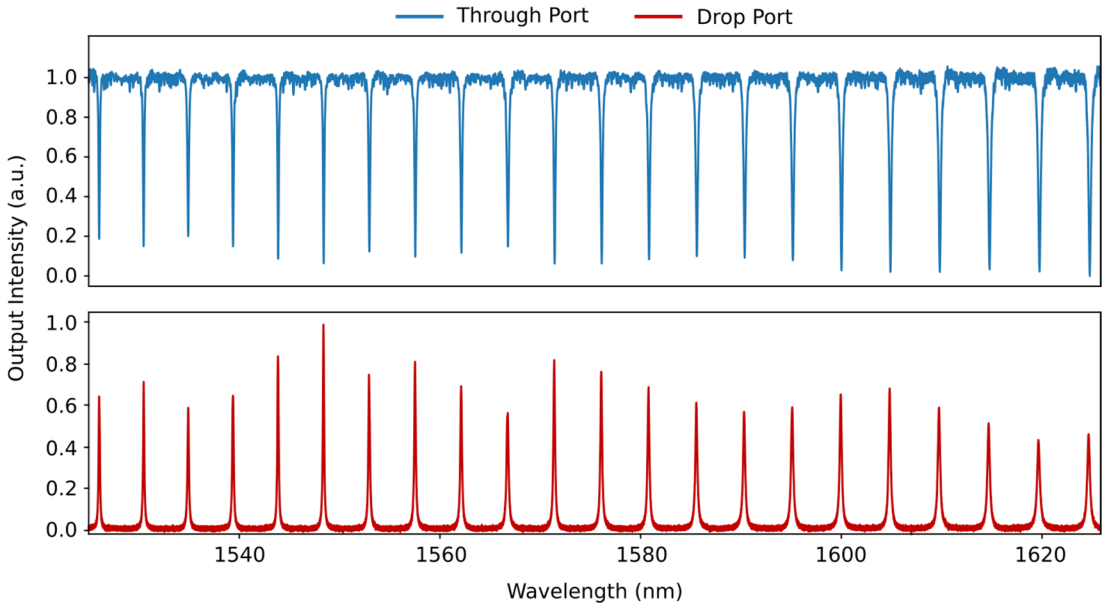

Fig. 4.9: Output spectra for a standard ring, at the through (blue) and drop (red) ports.

The vertical scale of Fig. 4.9 is normalized, so it is easier to compare both spectra. Although it would be interesting to compare the absolute output power from

both ports, such comparison is challenging because it is heavily dependent on the polishing procedure and the alignment. For the data shown, the drop port maximum level was 3 dB below the through port.

The reason for the difference in the extinction ratios (through port) and peak intensities (drop port) is a combination of waveguide dispersion, and the wavelength dependence of the coupling coefficient and the input/output alignments.

It is clear that the drop port noise level is lower than the through port. Since light is only collected at the drop port when it is resonant with the ring, the noise for this port comes from the photodetector and data acquisition board. On the through port, however, we also have the laser noise, and possibly Fabry-Perot interferences at the chip coupling and fiber connections, that due to the periods involved are effectively noise sources. This can be verified by expanding the plot around one of the resonances (1534.8 nm, for example), as seen in Fig. 4.10.

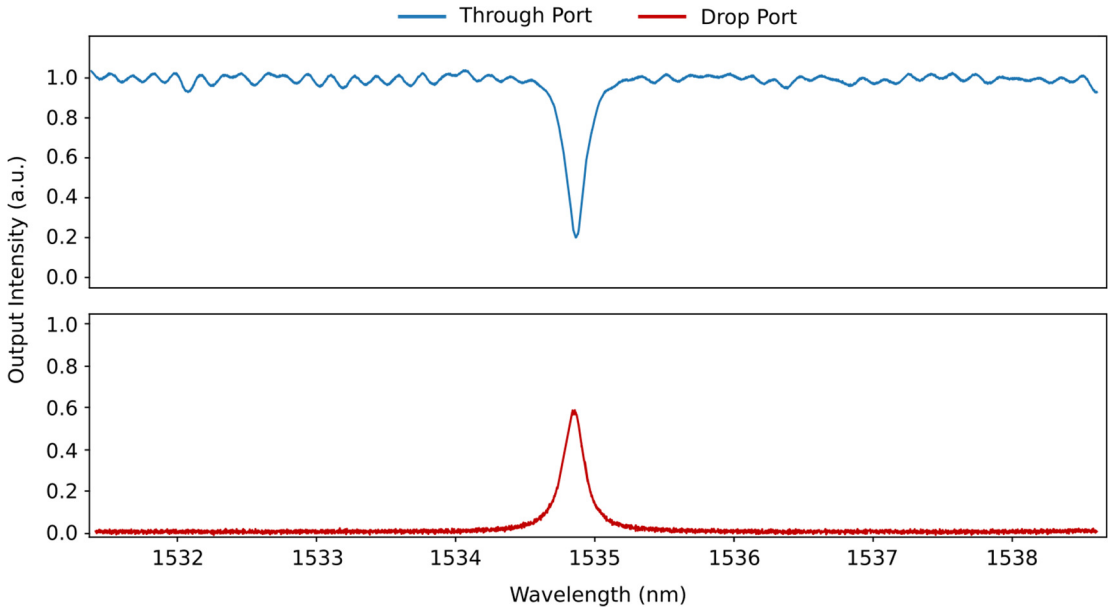

Fig. 4.10: Detail of one resonance, showing the oscilatory noise on the through port spectrum.

For this particular measured ring, the FSR is 4.4 nm, and the Q factor varies from 10200 for the 1525 nm resonance, to 5400 for the 1624 nm resonance. This data matches fairly well the values from the calculated spectra of Fig. 2.15 and Fig. 2.17.

For the samples with the Al_2O_3 top claddings, the output spectra at the drop port for two samples are shown in Fig. 4.11. The red curve corresponds to one where the procedure described in the previous section was employed to replace the top cladding above the devices only, preserving the SiO_2 layer on the remaining chip regions. Clearly, the noise level is higher than on Fig. 4.9, and the maximum output power is 10 dB below the blue curve, that corresponds to a sample initially without the top cladding layer, where the deposited Al_2O_3 film covers the entire chip.

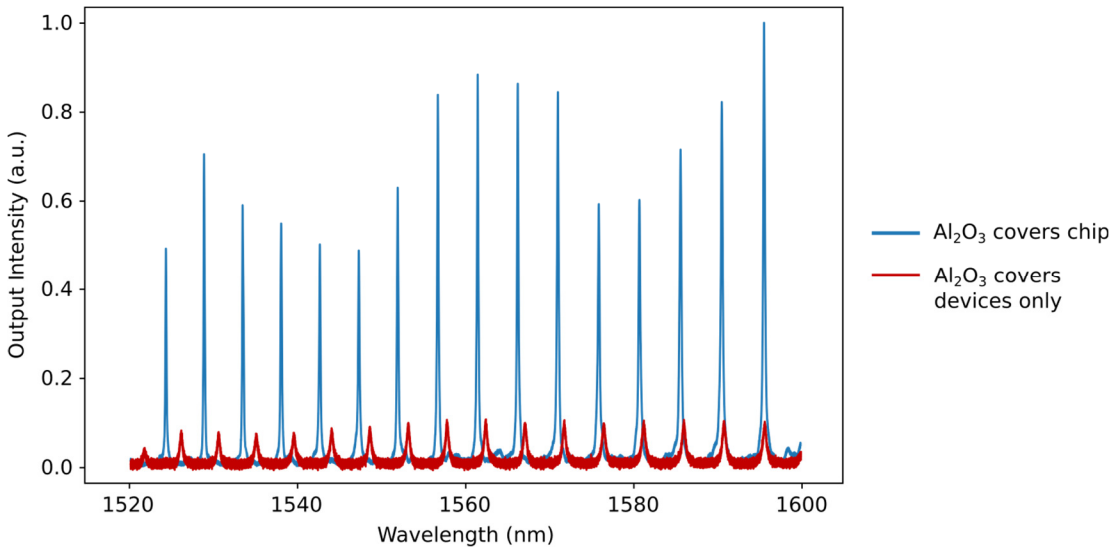

Fig. 4.11: Drop port output for samples where the alumina film cover the entire chip (blue), and where only the devices are covered (red).

The Q factors for the 1547.6 nm (blue) and 1548.6 nm (red) resonances are 8600 and 3800, respectively. This decrease (more than 50%) in the Q factor indicates that most of the additional loss comes from inside the ring, and is not a result of an inadequate polishing procedure or poor alignment. A small attenuation is expected at the top cladding interfaces for the designs from Fig. 4.5, where there is an abrupt refractive index change. Since resonant light completes a high number of roundtrips inside the ring (related to the cavity finesse), it is possible that the interface attenuation is accumulated, leading to a higher energy loss, explaining the substantial Q factor reduction.

Also worth mentioning is the small FSR difference between the two spectra, 4.6 nm for the sample with the entire Al_2O_3 top cladding, and 4.5 nm for the sample where only the rings are covered by the deposited film. This difference is also responsible for the resonances mismatch, and is caused by the fraction of the ring not covered by alumina, leading to distinct effective lengths.

Since the higher loss and lower Q factors were consistent across different samples that underwent the etching procedure before the film deposition, the next section will only present results from previously unclad samples, so the Al_2O_3 layer acts as the top cladding for the entire chip. Although these devices possess different coupling characteristics, the results are not negatively affected. Furthermore, as will be demonstrated, we were still able to study the individual effects of internal rings on the output spectra without significant interference from undesired spontaneous or stimulated emissions.

4.3 Loss Compensation

The setup shown in Fig. 4.8 needs to be modified to perform measurements of the loss compensation on the fabricated devices. The first step is, of course, to include the pump laser. The laser used as pump was of the same brand as the signal, with the same tunability width, but at a lower wavelength range (Agilent 81980A 1465 nm – 1575 nm). This laser has a limited nominal output power of 14 dBm, which in practice varies with the wavelength. For the wavelengths of interest (~1480 nm), the maximum measured output power was 11 dBm. According to Section 2.5, this power level is enough to observe a considerable increase in the output power. However, since there are coupling losses involved, the pump power entering the ring will be lower (up to 8 dB). An attempt to compensate this issue involves adopting a pulsed signal scheme, effectively concentrating the signal photons in a short time window, permitting a higher fraction of the Er^{3+} ions to return to the excited state before the next pulse arrives. This results in

a higher (but during a short time) stimulated emission. A HP 8116A function generator in conjunction with a Covega $LiNbO_3$ intensity modulator created the modulated signal.

Another important step to consider is the pump filtering, since the photodetector that measures the signal is also sensitive to the pump wavelength. To ensure the minimum residual pump possible, a WDM filter was employed, in addition to a counter-propagating pumping setup, in which circulators (with 28 dB of isolation and 1.5 dB of insertion loss) separate the relative backward and forward components, allowing the signal output to be measured at the primary power meter (PM1), and the remaining pump output level to be measured at a secondary power meter (PM2). To ensure an accurate measurement of the signal pulses, a SRS SR200 Boxcar Averager with a 2 ns Gated Integrator is synchronized to the function generator, and samples the voltage from the power meter during the pulses only, averaging the data before sending it to the computer. The entire setup can be viewed in Fig. 4.12a photograph, and is illustrated in Fig. 4.12b.

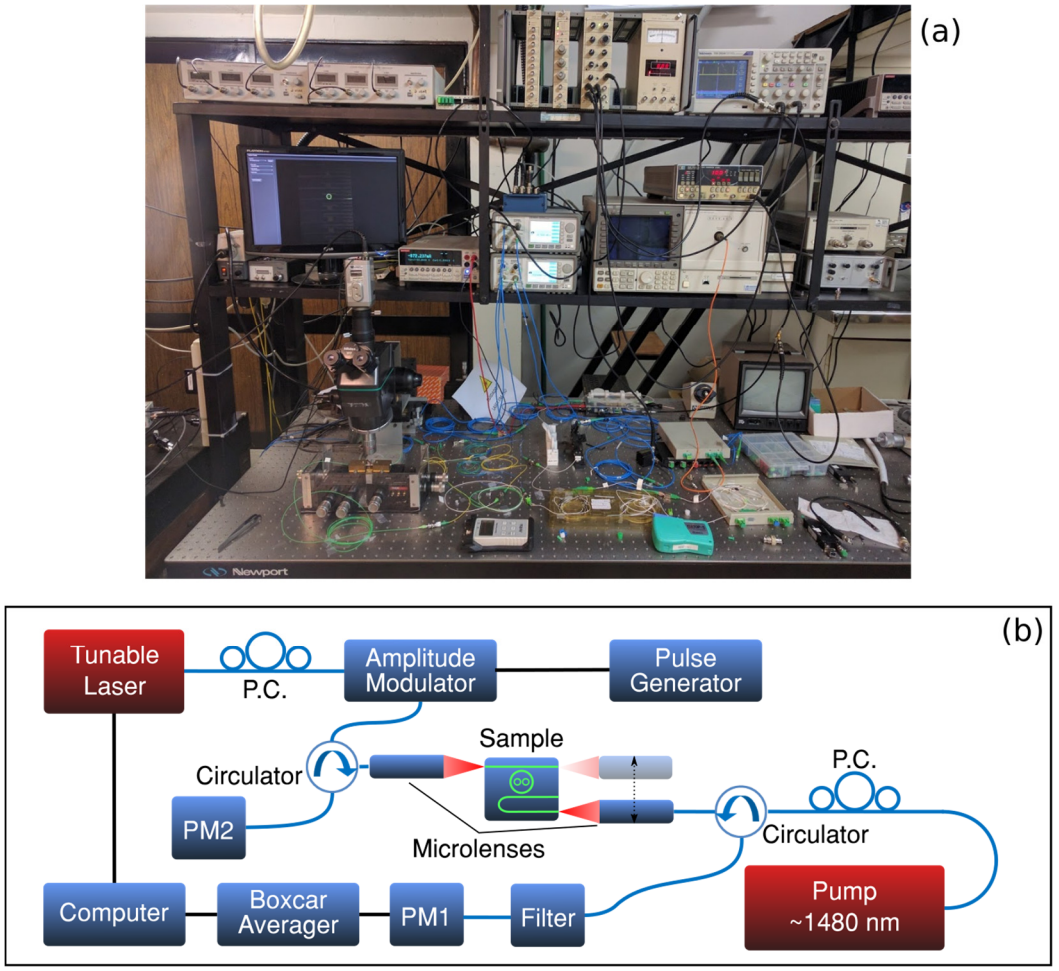

Fig. 4.12: Photograph (a) and schematic (b) of the experimental setup for the loss compensation measurements.

The first step to characterize the loss reduction effect of the erbium-doped layer is to set the pump wavelength to a resonance of the selected ring. To achieve this, the two closest resonances to 1480 nm were found, and the one below this wavelength was selected (1476.2 nm for the measured outer rings), guaranteeing a higher energy for the pump photons. To trap the maximum possible energy inside the ring, thus optimizing the Er^{3+} ions pump absorption, the wavelength was carefully swept in steps of 100 pm, 10 pm, and 1 pm, until the minimum pump output power was measured at PM2, when the lensed fiber was aligned to the through port. Thermal effects can shift the resonances, so to maintain the pump tuning, the chip mounting base temperature must be controlled with a Peltier. Nevertheless, the signal laser can also cause a temperature increase, due to two-photon and free carrier absorptions [86], so a low input power is best suited for

this experiment, which also benefits the signal enhancement measurement, as demonstrated in section 2.3.

From the results in section 2.5, the measured signal output power should rise when the pump power is increased. To first test this concept, and simultaneously verify the presence of amplified stimulated emission (ASE) and residual pump light, we observed the drop port output of a 0 dBm input signal, tuned to the 1548.5 nm resonance of a ring with 20 μm of radius. This signal was modulated at 4 kHz at a duty cycle of 50% (resulting in 125 μs pulses), and a Tektronix TDS-1012 oscilloscope was used to observe the output. To tune the signal wavelength to the resonance, the same procedure described above was used, where the lensed fiber was aligned to the through port, and the wavelength was carefully adjusted until the minimum output power was measured at PM1.

The result can be seen in Fig. 4.13, for the conditions when the pump is disabled or enabled (CW). It is important to notice that for the second case, the signal wavelength needs to be adjusted to the new resonance position, due to the shift caused by the thermal effects from the relatively high pump power.

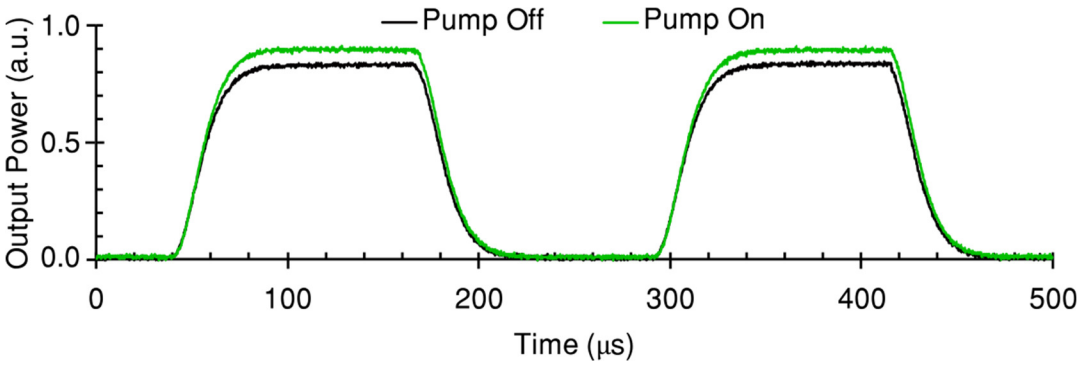

Fig. 4.13: Pulsed signal verification. When the pump is turned on, the output power increases 0.4 dB.

We can see that when the pump is enabled, the signal increases. As previously mentioned, it is difficult to individually attribute an exact value to each coupling loss present, and consequentially it is just as difficult to know the exact signal power at the ring input and output, preventing the measurement of internal optical gain (the optical

gain inside the device, not considering the coupling losses). Therefore, to present a quantitative analysis of the power increase, we can define the signal enhancement, in dB, as:

$$SE \equiv 10\log\left(\frac{P_{On}}{P_{Off}}\right) \quad (4.1)$$

Here P_{On} is the output power with the pump on (10 dBm), and P_{Off} the output power with the pump turned off. For this measurement, $SE = 0.4$ dB, a small but clear and significant observation, considering that the measurement parameters (such as pulse width and repetition rate, and input power) were not optimized. We can also notice that the noise level remains constant during the measurement, and the power is only increased within the pulse duration. This indicates that the increase in output power when the pump is enabled, happening exclusively when the signal is present, is not due to residual pump light bypassing the circulator, and thus our isolation/filtering setup is sufficient for these measurements. Additionally, this observation also reassures us that the ASE that is generated on the bus waveguides does not contribute significantly to the measured output power. In case the power increase would also be present outside the pulse duration, these two issues would become significant, and the designs from Fig. 4.5 would be necessary to avoid them.

Following the confirmation of the increase in output power, the next step before the final measurements was to optimize the pulse duration and repetition rate, aiming to obtain the maximum signal enhancement. Using the same setup and procedures as the last measurement, the data from Fig. 4.14 was obtained, but now for a resonance at 1534.3 nm.

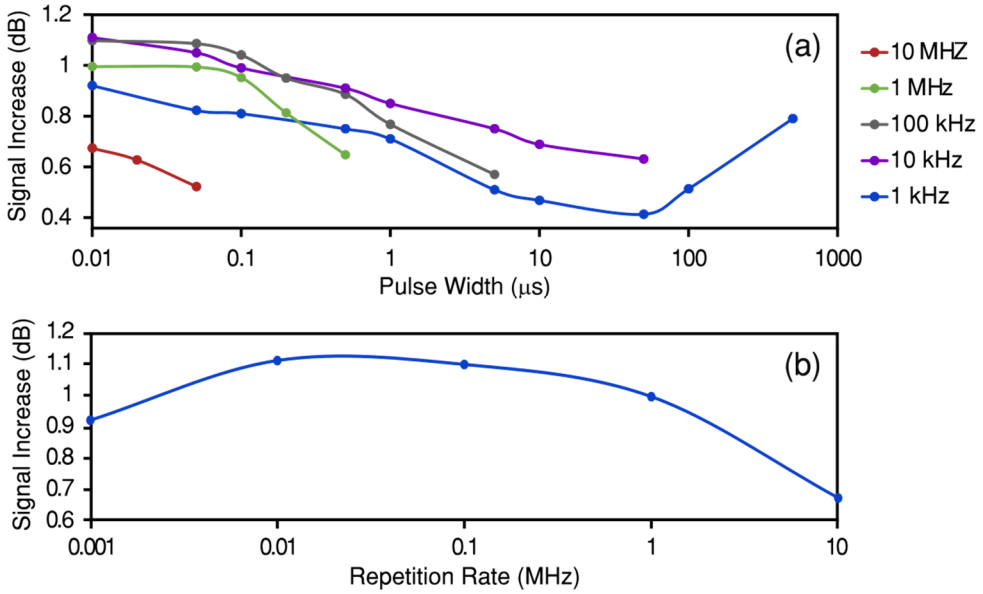

Fig. 4.14: (a) Signal increase for varying pulse widths and repetition rate. (b) Maximum observed increase for different repetition rates.

From the upper graph, we observe that as the pulse width increases, the signal enhancement tends to decrease, the 1 kHz case being the exception. In addition, the enhancement is higher as the repetition rate decreases, peaking at 1.11 dB for 10 kHz. The explanation for this is that for shorter pulses and lower repetition rates, Er^{3+} ions have a higher probability to absorb a pump photon and reach the excited state before the next signal pulse arrives. However, if the repetition rate is too low, the probability of ions decaying via spontaneous emission increases at the same time, explaining the peak at 10 kHz followed by a lower result for 1 kHz.

The blue curve in Fig. 4.14a, corresponding to the 1 kHz case has a different behavior than the rest, as the signal enhancement increases for pulse widths higher than 100 μs. This is explained by the fact that, as the spontaneous emission for this curve is relatively high, there is a high fraction of lost pump energy, causing this repetition rate to be very inefficient for this purpose. Nevertheless, when the pulse width increases, effectively increasing the duty cycle, there is a shorter time at which this undesired effect happens, and a fraction of the light that was emitted via spontaneous emission is now emitted via stimulated emission, contributing to the output power increase.

Although the optimal repetition rate according to Fig. 4.14b is 10 kHz, a repetition rate of 100 kHz and pulse width of 50 ns were chosen for the subsequent results, to minimize the possible spontaneous emission and prevent loss of data due to the SR200 averaging. It is important to address the fact that there is a trade-off between file size (and processing time), measurement time, resonance definition (related to the wavelength resolution), signal enhancement, and averaging. With this choice, we obtained data files with 160000 points, during 16 seconds measurements (wavelength sweep of 5 nm/s), resolution of 0.5 pm, with 4 sample averages. This results in a negligible SE reduction from the optimal case (1.11 dB to 1.09 dB).

As mentioned in section 4.1, besides the Er-doped Al_2O_3 film, an undoped film was deposited on some of the samples as well. These control samples underwent the same thermal annealing process, and focusing on a resonance close to 1550 nm, we can compare the drop port output power from both samples, for the pump turned off and on (10 dBm) conditions. The results can be seen in Fig. 4.15.

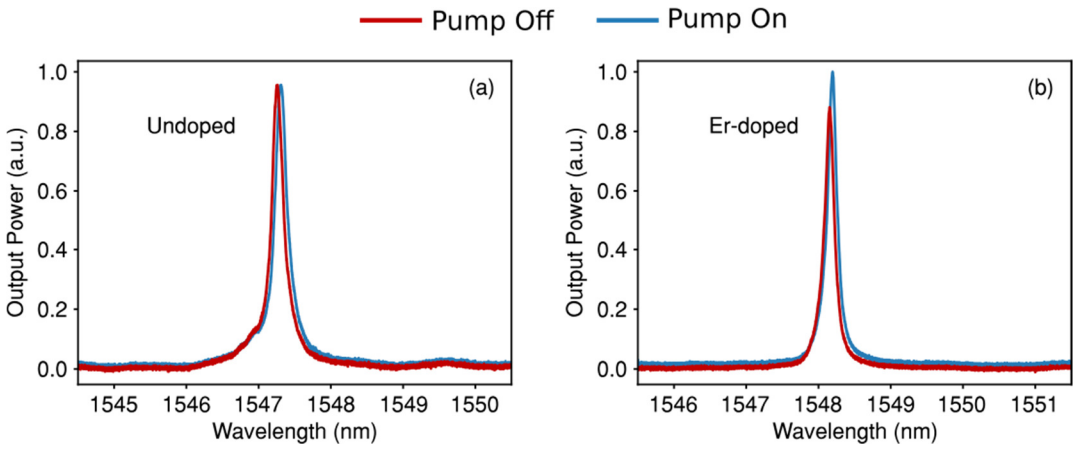

Fig. 4.15: Drop port output for an undoped (a) and doped (b) sample, with the pump turned off and on (10 dBm).

Besides a small thermal red-shift, the behavior from each sample is significantly different when the pump is turned on, and we can see a 0.6 dB increase for the Er-doped sample. No mensurable increase can be seen in the undoped case. Again, this confirms that the signal increase is not residual pump light, and in fact is a result of

the stimulated emission from the Er^{3+} ions. The small difference on the resonance wavelength can be attributed to a fluctuation of the film quality during deposition, effectively changing the refractive index.

For a wavelength sweep from 1520 nm to 1580 nm, using a sample with two internal rings (5 µm of radius), the resulting spectra for the pump on (10 dBm) and off conditions can be seen on Fig. 4.16. In addition, the pump wavelength region is also present on the same plot.

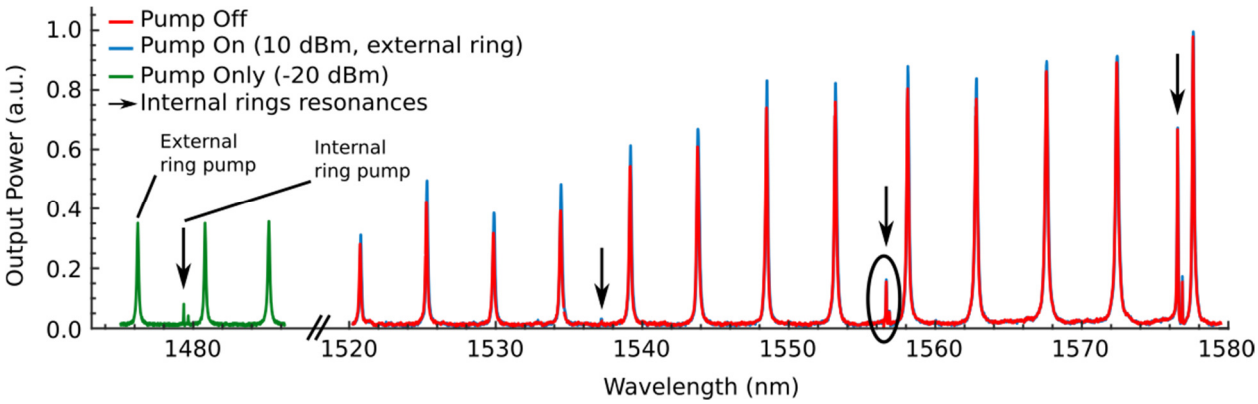

Fig. 4.16: Drop port output spectra for a sample with two internal rings, for the disabled (red) and enabled (blue) pump conditions, tuned to an outer ring resonance, indicated in green. Resonances from the internal rings are indicated by black arrows.

The pump wavelength used is indicated on the green curve, corresponding to a resonance at 1476.2 nm (external ring). For most of the resonances, there is a clear increase in output power when the pump is enabled, the notable exceptions being the inner ring resonances, indicated by black arrows, displaying a greatly reduced output power, as predicted in section 2.4. If we plot the signal increase as a function of the wavelength for each of the outer ring resonances shown, the result in Fig. 4.17a is obtained, in linear scale.

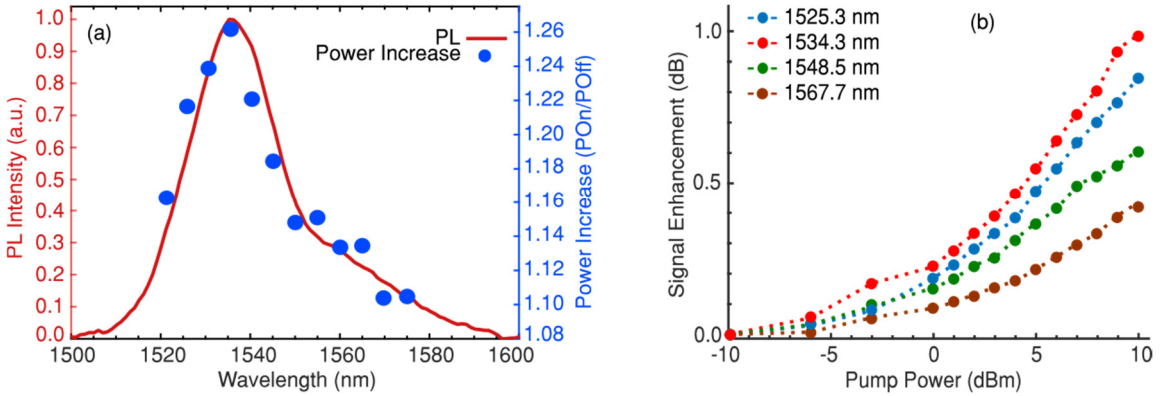

Fig. 4.17: (a) PL of the Er-doped Al_2O_3 film (left axis) and output power increase (right axis). (b) Signal enhancement in function of pump power, for different outer ring resonances.

Comparing these data with the sample's PL spectrum (obtained by the method described in section 3.2), we notice a high similarity. Since the PL and erbium emission cross-sections are closely related, this result is an additional confirmation that the power increase is indeed an effect of the Er-doped film.

If we now perform the wavelength sweeps with varying pump powers, the signal enhancement will be different for each measurement. Selecting certain illustrative resonances (low and high edges of the sweep, highest increase, and closest to 1550 nm), the graph from Fig. 4.17b can be constructed. We can observe that the signal enhancement is higher as the pump power increases. In contrast with Fig. 2.21a, there is no clear saturation present. This is due to the coupling losses effectively decreasing the pump and signal powers that enter the chip, and consequently decreasing the energy inside the rings as well. From these results, we confirm that the highest signal enhancement occurs on the 1534.3 nm resonance, as expected, and the resonance at 1548.5 nm presents a 0.6 dB lower enhancement. The Q factors for these resonances, displayed in Table 4-1, increase when the pump power is at its maximum (10 dBm), and the highest improvement, at 1534.3 nm, is 5.7%. These values were obtained by fitting a Lorentzian curve to the data points and using Eq. 2.32, where the full-width at half maximum (FWHM) is a fitting parameter corresponding to the resonance width. These fitted curves are shown in Fig. 4.18.

Table 4-1: Quality factors for selected resonances of a single ring.

Wavelength (nm)	Q (Pump Off)	Q (Pump On)	Q Increase
1525.3	11520	11820	2.6%
1534.3	10500	11100	5.7%
1548.5	9490	9970	5.0%
1567.7	7330	7360	0.4%

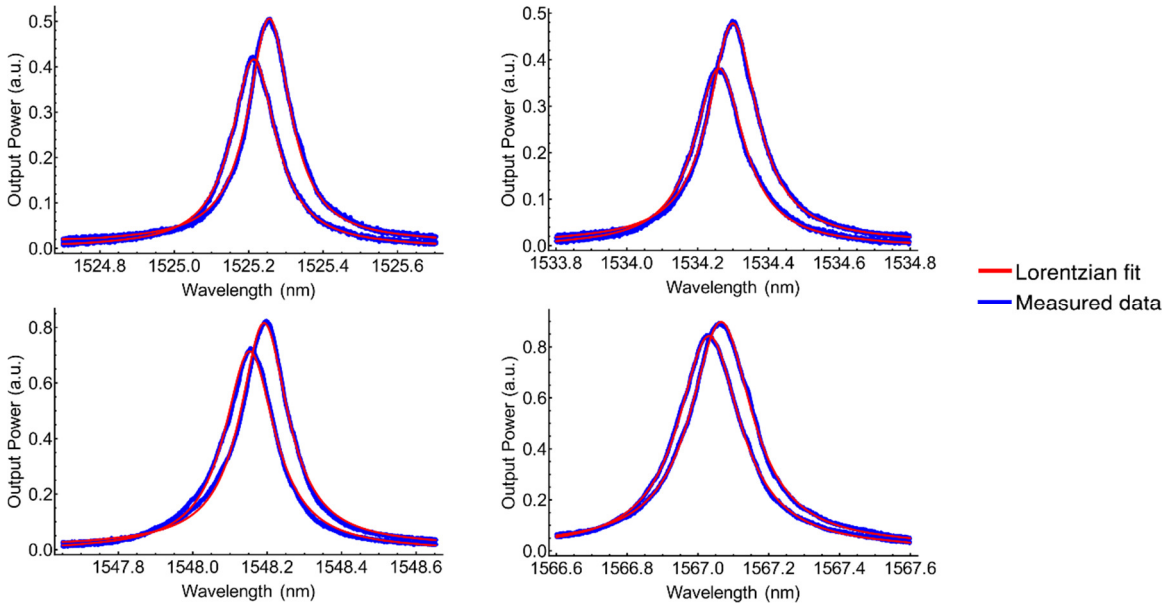

Fig. 4.18: Lorentzian fits of the respctive resonances.

In accordance with section 2.5, the Q factor decreases as the wavelength increases, due to the change in the coupling factor. The Q factor increase reaches its maximum at the 1535 nm region, corresponding to the PL intensity and the emission cross-section peaks. This change in the quality factor can be interpreted as loss reduction, since it is equivalent to a decrease of energy dissipation per roundtrip, an additional confirmation that the attenuation is being compensated.

To complete this first analysis, we can compare the data from Fig. 4.17a and Fig. 2.21b, as shown in Fig. 4.19.

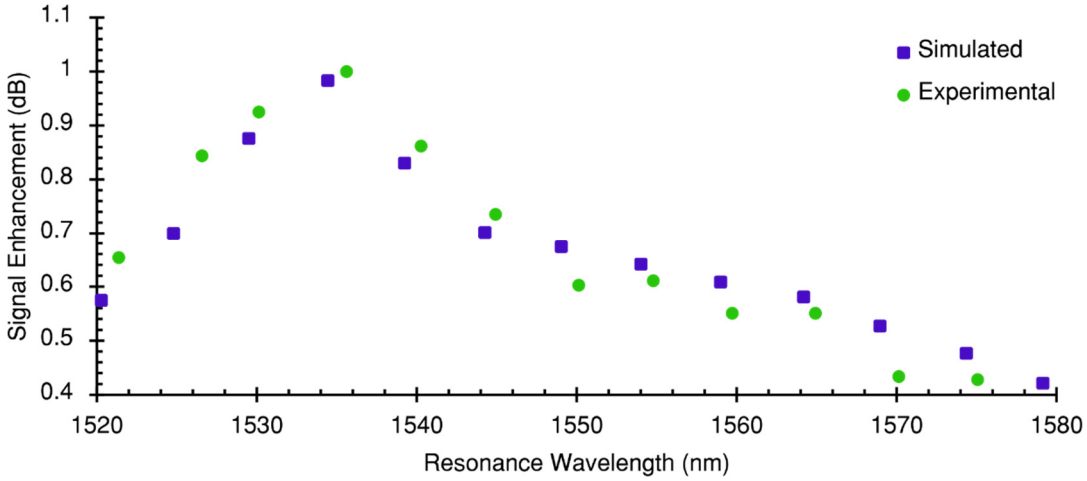

Fig. 4.19: Comparison between the simulated and experimentally obtained spectral signal enhancement for external ring resonances.

The data are clearly consistent, and the measured signal enhancement deviates only 2% from the calculated value at the 1535 nm region. This is an important verification of the model developed in Chapter 2, before proceeding with the analysis performed in the next section.

To analyze the behavior of the inner rings resonances, the pump wavelength needs to be tuned to a value corresponding to one of these, as close to 1480 nm as possible. From the green curve of Fig. 4.16, we can see that 1479.6 nm is an appropriate choice, and performing the wavelength sweep for this pump condition yielded the spectra in Fig. 4.20.

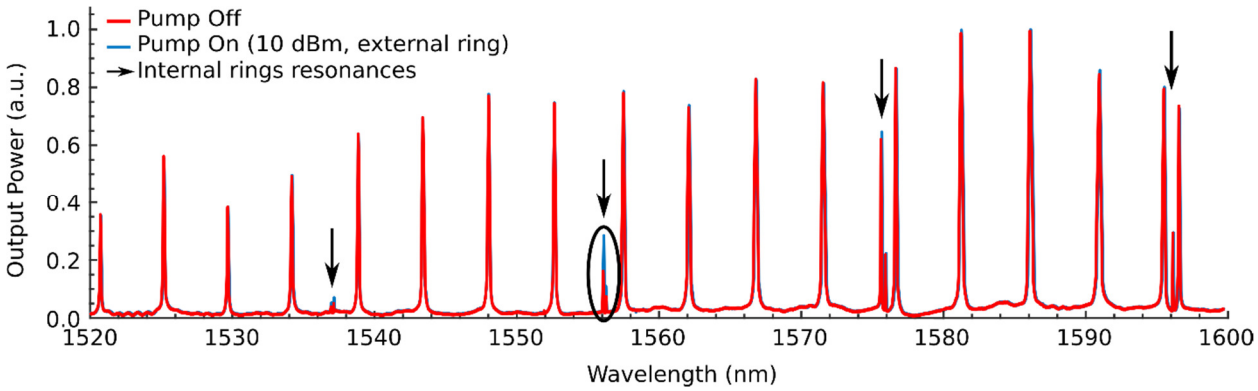

Fig. 4.20: Drop port output spectra for for the disabled (red) and enabled (blue) pump conditions, tuned to an inner ring resonance. Resonances from the internal rings are indicated by black arrows.

The output spectrum itself is very similar to the case where the external ring is pumped, but when the pump on/off behavior is examined, both cases become very distinct. There is a slight (< 0.1 dB) output power increase for a few of the outer ring resonances. For the internal rings, however, we can observe a stronger signal enhancement, as opposed to the previous pump wavelength. Since the FSR for the smaller rings is higher, only 4 resonances are contained within the sweep range (1520 nm to 1600 nm). As such, it is not possible to perform a detailed analysis of the spectral enhancement as shown in Fig. 4.17a and Fig. 4.19. From the three resonances that present output power increase (1537.0 nm, 1556.2 nm and 1577.8 nm), the one at 1556.2 nm is clearly the most efficient, where the signal was improved by 2.6 dB. This resonance is indicated by a circle on both Fig. 4.16 and Fig. 4.20, and is shown in detail in Fig. 4.21a. Comparing the signal enhancement from this resonance with the one at 1534.3 nm (when the external ring is pumped), we obtain the curves in Fig. 4.21b.

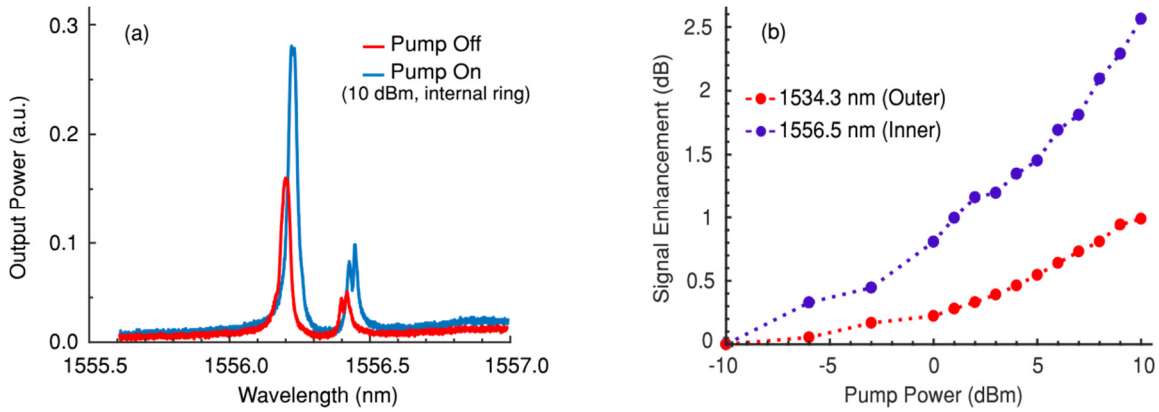

Fig. 4.21: (a) Detail of the 1556.2 nm resonance when the pump is tuned to a internal ring resonance (enabled and disabled). (b) Comparison between the signal enhancement for the 1556.2 nm and 1534.3 nm resonances.

The signal enhancement is significantly higher for this internal ring resonance (2.6 dB), compared to the external ring (1 dB). This is an indication that a photonic molecule has a higher potential for optical loss reduction, or even amplification. Due to the higher Q factor, light remains trapped in the devices for a longer period of time. This

is analogous to a longer amplifier, which according to section 2.3, is capable of providing a higher gain if the pump power is sufficient.

If we now focus our attention to the output power of the inner rings resonances, it is clear that the absolute loss will be very high for the resonances near 1537 nm and 1556 nm, but lower near 1578 nm and 1596 nm. This difference can be explained by small deviations between designed and fabricated dimensions (as low as 100 nm in 31 μm of perimeter), causing a Vernier effect that leads to the higher distance between the inner and outer rings resonances observed at lower wavelengths. As the proximity between these resonances increases, light trapped in the inner ring has a higher chance of coupling back to the external ring, thus exiting via the drop port. The output power of an inner ring resonance can be increased if it is brought closer to one corresponding to the outer ring. This can be done via careful design and fabrication or active control [87], and would be of special significance for the wavelength region within the Er emission bandwidth. The Q factor of such resonances, however, decreases at the same time, so a trade-off exists, and an optimal design can be obtained for the intended application.

It is important to notice that due to a high Er concentration, a strong green luminescence results from the pumping process, allowing us to verify the location of the highest light accumulation. In Fig. 4.22a and Fig. 4.22b we can see the luminescence resulting from the pump at 1476.2 nm (external ring) and 1479.6 nm (internal ring), respectively. At high pump powers, this green light emission is even visible to the naked eye, as seen in Fig. 4.22c.

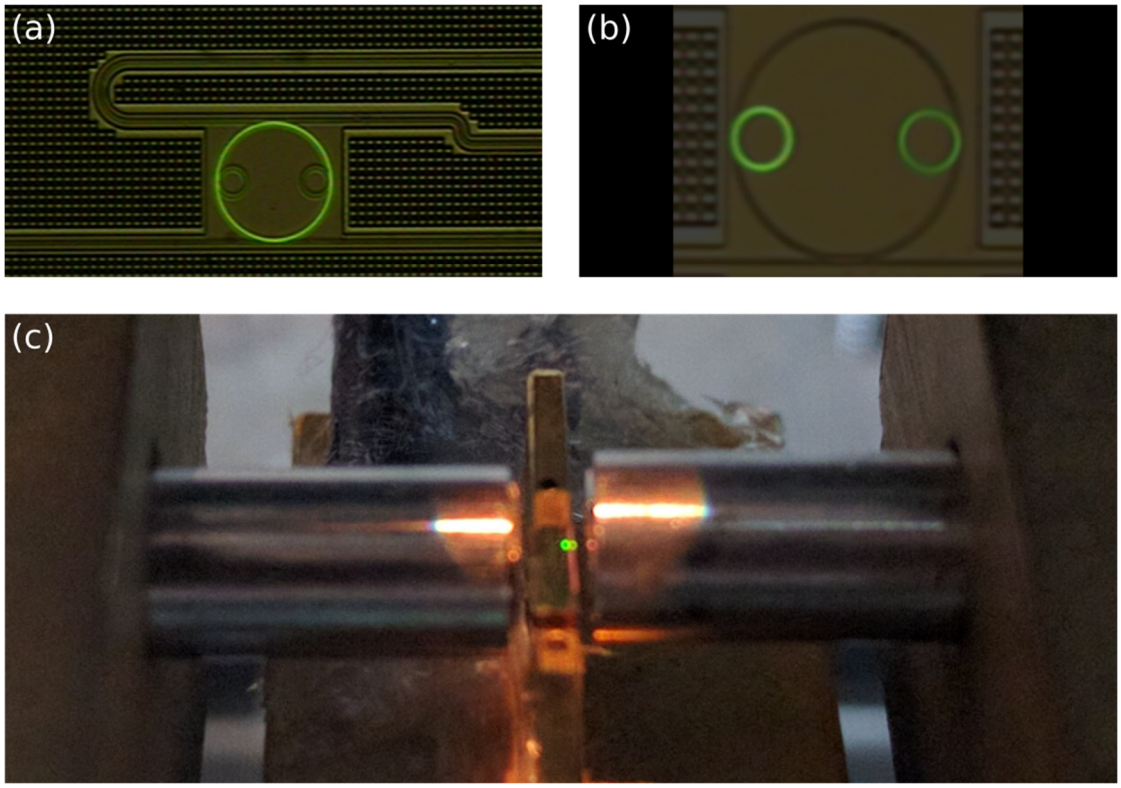

Fig. 4.22: Green luminescence when the sample is pumped at a external (a) and internal (b) ring resonance wavelength. The luminescence is even visible to the naked eye (c).

This phenomenon happens when an Er^{3+} ion at the excited state ($^4I_{13/2}$) absorbs additional photons, either from the pump or signal lasers, and is promoted to the $^4I_{9/2}$ level, eventually reaching the $^4S_{3/2}$ or $^2H_{11/2}$ states. When the ion returns to the ground state, via spontaneous emission, a photon with the corresponding energy is emitted (530 nm or 550 nm, respectively). Since photons are being absorbed and are not reemitted at the signal or pump wavelengths, the stimulated emission potential is degraded [39] [88]. To mitigate this effect, the device can be co-doped with Ytterbium, which absorbs the pump energy and transfers it to the erbium ions, so a higher amplification can be achieved. When applied to a high-Q cavity, this can enable the design and fabrication of amplifiers and lasers based on Er/Yt-doped materials [89]. An additional method to further increase this potential is to employ slot waveguides on photonic molecules, which greatly enhances the overlap between the mode energy and Er-doped cladding, since light travels between

two high-index walls [43] [44]. With this, it should be possible to create compact lasers on silicon with CMOS compatible technologies.

The last step of the analysis of our experimental results is to obtain the Q values for the resonance of Fig. 4.21a. As before, by fitting a Lorentzian curve to the spectrum, we can obtain the FWHM, related to the Q factor. When unpumped, this value is approximately 40000. When the pump is turned on, however, the quality factor is very close to 50000, representing a 25% increase.

If we consider an undoped device with this Q (50000), with the same dimensions as before but a different coupling gap, and calculate the output power of this resonance using the formalism in sections 2.4 and 2.5, the insertion loss would be approximately 3.6 dB. Doing the same for a doped device with this enhanced Q value, the loss would decrease to approximately 0.2 dB. From a device design point of view, the signal output power and Q enhancement we measured would be equivalent to a loss reduction of 3.4 dB, since it should be possible to obtain a photonic molecule with the same dimensions and resulting Q factor desired, but with a much lower insertion loss when an Er-doped cladding is considered.

This observation enabled us to perform an additional (theoretical) study of the loss reduction from this perspective.

4.4 Designing Low-Loss Compact High-Q Devices

If we extend the formalism from section 2.5 to include the matrix equations for a photonic molecule with two internal rings, as the one in Fig. 2.18b, and focus on one of the internal rings resonance, we obtain the drop port output spectra shown in Fig. 4.23a, detailed in Fig. 4.23b. The internal rings radius was adjusted to match the location of the equivalent measured resonances (r = 5.104 μm).

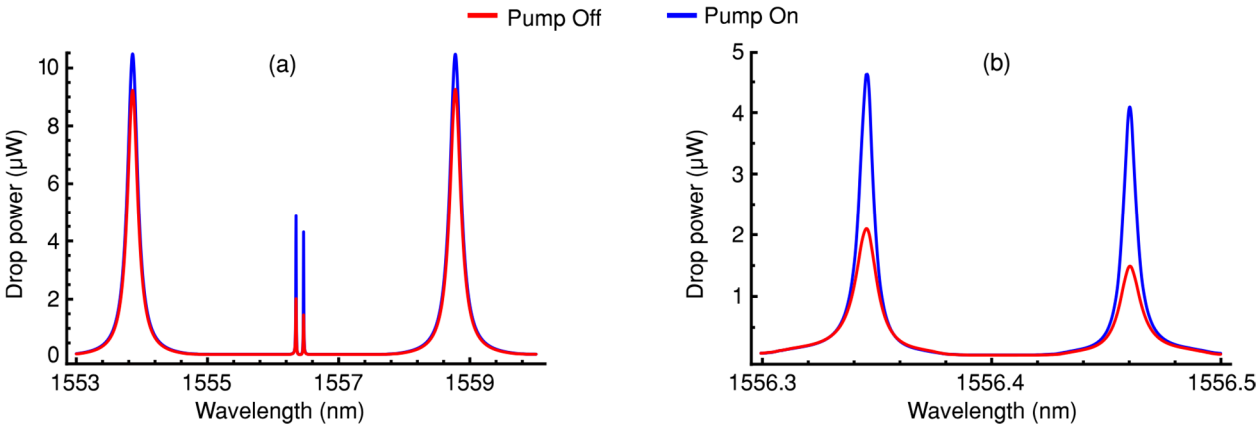

Fig. 4.23: Calculated drop port output spectra for a photonic molecule with two internal rings (a), and zoom of the internal rings resonances (b).

As in the measured results, we see that the output power increase is higher for the internal rings resonances, reaching 3.6 dB, as opposed to 0.6 dB for the external ring. The Q value of the inner resonances is 96700, increased to 265500 when the pump is turned on. Since these calculations consider that the entire device is pumped at the same time, the enhancement is present for all resonances. The signal enhancement and Q values obtained for the inner rings resonance are higher than the measured ones (2.6 dB, Q of 40000 increased to 50000). A possible explanation is that, since these resonances present a higher Q, a photon performs more roundtrips on average before exiting the ring. A small difference in the parameters considered can lead to a higher deviation from the calculated values. Additionally, since the inner rings are smaller, it is possible that curvature losses play a larger role on the experimental results. We did, however, consider these losses for the presented results (0.005 dB/turn, or 0.003 dB/rad) [90], but they may differ from the real values.

Despite the difference between these values, we can still take advantage of the developed model to predict the behavior of similar devices, but with varying coupling distances. The graphs in Fig. 4.24a show the resulting signal enhancement (ratio between the output powers with the pump turned on and off) in function of the separation gaps, considering the external and internal rings resonances at 1553.9 nm and 1556.35 nm, respectively. For simplicity, the gap is considered the same on all coupling regions.

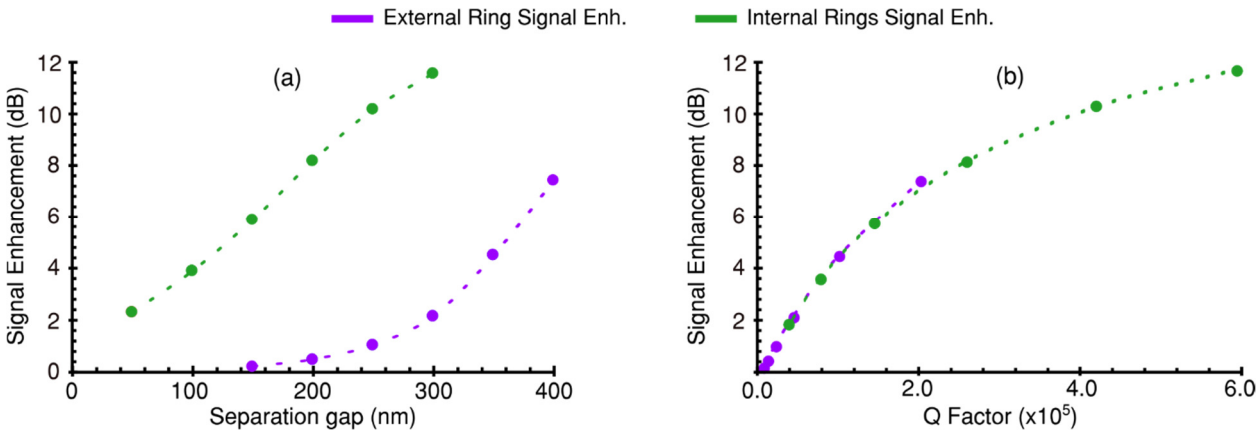

Fig. 4.24: Signal enhancement for external and internal rings resonances in function of the separation gap (a) and resulting Q factor (b).

This result shows us that, again, the internal ring resonances present a higher signal enhancement, reaching 11.5 dB for a 300 nm gap, compared to 7.5 dB for the external ring resonance with a gap of 400 nm. For gap distances higher than the ones showed, the spectra start to diverge, due to the very low coupling coefficient ($\kappa < 0.03$). For each of the obtained data points, we can calculate the resulting Q factor (when the pump is turned on), from the FWHM of the fitted Lorentzian curve. Thus, the graph in Fig. 4.24b can be constructed. We see that the signal enhancement seems to depend mainly on the Q factor, but that is only the case because the waveguide characteristics of the rings are the same (including the separation gaps). Nevertheless, it is clear that by employing internally coupled rings, it becomes possible to obtain higher Q factors on the same chip area.

In addition to the signal enhancement, we can plot the relative output power as a function of the quality factor, for both doped and undoped devices, resulting in the graphs from Fig. 4.25.

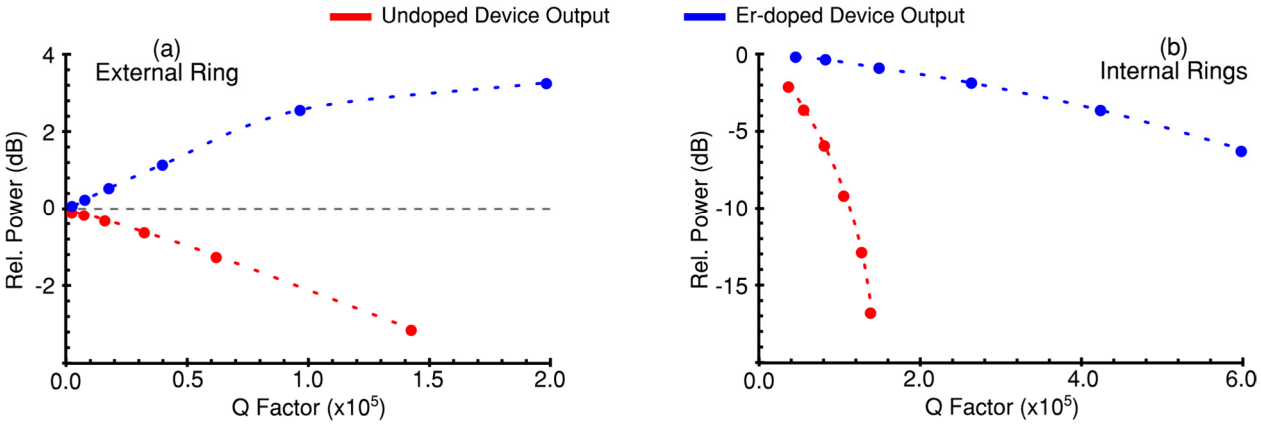

Fig. 4.25: Relative output power for undoped and doped devices, considering external (a) and internal (b) rings resonances.

As the first calculations for a single ring show (section 2.5), it is possible to obtain a small optical gain. When this value is compared to the loss introduced by an undoped device, designed to present the same Q factor as the doped one, we can conclude that the effective loss reduction of this technique is even higher than the observed power increase. As the Q factor increases, the output power of the undoped device decreases, while increasing for the Er-doped clad ring. This effect is clearer when we consider the resonances from the internal rings (Fig. 4.25b). Although there is no optical gain, the output power for the undoped case decreases much faster than for the case where this method of loss reduction is applied. As an example, for a Q factor of approximately 1.5 $\times$ 10^5, the undoped insertion loss is higher than 15 dB, decreasing to less than 1 dB for the doped case.

For a clearer visualization of the loss reduction impact, we can plot the difference between the output powers as a function of the Q factor, and the results can be seen in Fig. 4.26.

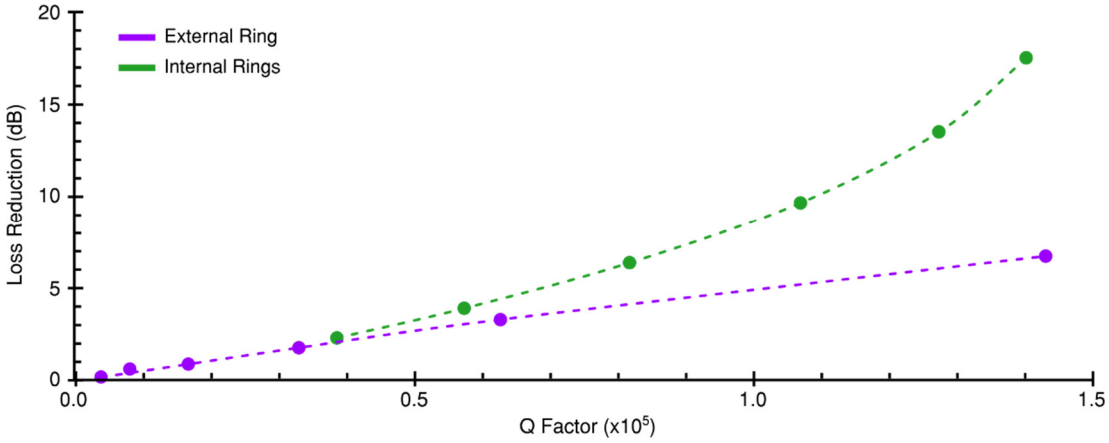

Fig. 4.26: Effective loss reduction for external and internal rings resonances.

The loss reduction for both cases increase with the Q factor, but the rate of increase is higher for the internal rings, reaching 17 dB for the $Q = 1.5 \times 10^5$ case. For the extreme situation ($Q = 6 \times 10^5$), the total attenuation is reduced to only 5 dB from an (extrapolated) initial value of more than 30 dB. This represents a loss reduction of more than 25 dB.

These results show that the process of employing Er-doped claddings for loss reduction can enable applications of compact high-Q devices based on photonic molecules, such as routers or narrow bandpass filters where low insertion losses and reduced chip area usage are important considerations. A device presenting an insertion loss of 15 dB is not suitable for most ends, but if this value is reduced to 1 dB, the number of applications increase dramatically, with the benefit of using the same design without additional chip area sacrifice.

4.5 Chapter Summary

This chapter covered the experimental portion of the work related to the application of Er-doped Al_2O_3 films as claddings of Si Photonics devices based on ring resonators. The fabrication process was detailed, focused on the post-processing steps performed on samples manufactured in a SOI foundry. The basic characterization of the devices was described, and the results discussed, not diverging from the predicted

behavior from the theoretical model. When the devices were pumped, it was possible to observe an increase of the output power, confirming the potential for loss reduction of the method. Finally, the model developed in Chapter 2 was extended to include the internal rings, and additional analyses were performed to study the effective loss reduction provided by this technique from a device design point of view, where devices with high Q occupying a small chip area were demonstrated to be possible.

The next chapter will describe the study of the application of Er-doped Al_2O_3 films to III-V materials, focusing on the compatibility between the processes involved in the films fabrication and the delicate epitaxial structure from InGaAs/GaAs quantum well lasers.

5. Er-doped Al2O3 Films for III-V integrated Photonics

Although it was demonstrated that Er-doped Al_2O_3 films applied to Si photonics opens new possibilities for compact devices and cavities with a high quality factor, another interesting question is the possibility of application of these films on III-V devices. The high temperature processes involved in obtaining the films can lead to a degradation of the III-V electrical and optical characteristics, and this appendix will detail the study of these effects on InGaAs/GaAs Quantum well (QW) lasers, with the intent to evaluate the possibility of a conceptual monolithic Er-Doped Waveguide Amplifier (EDWA).

5.1 Concept

It has been mentioned that EDFAs had a major role in today's internet development, and signal attenuation is a relevant concern in silicon photonics. Considering the eventual connection between two distinct Si photonic devices where the signal intensity needs to be increased, the availability of a compact monolithic amplifier would be of great interest. In this context, the possibility of an Er-doped waveguide amplifier built on the same substrate as its pump laser is a promising study. This conceptual device is shown in Fig. 5.1.

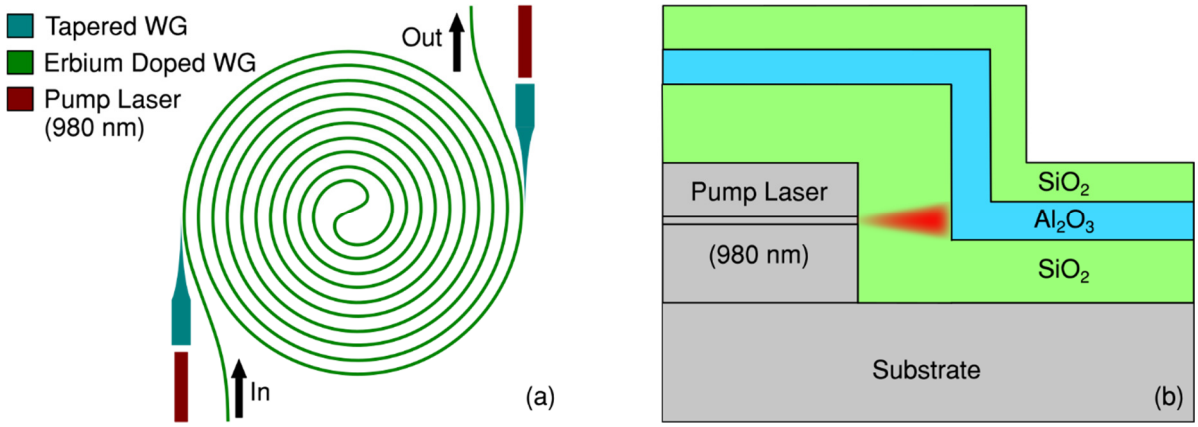

Fig. 5.1: (a) Illustrative representation of the entire device and (b) the coupling between the laser and tapered waveguide.

A bi-directional pump scheme is shown in Fig. 5.1a, where two lasers are fabricated on the substrate, and an Er-doped Al_2O_3 spiral waveguide is created on the space between them. Two additional tapered waveguides are used to couple light from the lasers into the main waveguide via evanescent field. Light from the laser is directly coupled to the tapered waveguides (Fig. 5.1b), and the distances and dimensions involved are such that the modes from each one of the waveguides (laser and Al_2O_3) have a high overlap, resulting in the highest coupling efficiency possible.

The pump lasers, emitting at 980 nm, excite the Er^{3+} ions present in the waveguide, and as the signal light (1520-1570 nm) travels along the spiral, it is amplified via stimulated emission, eventually exiting the device.

Conceptually, this device is an attractive project, despite certain fabrication difficulties such as the coupling regions. But one issue of particular concern, that will be studied in this chapter, is the high temperature annealing involved in the "activation" of the Er-doped film, as described in Chapter 3. Since many III-V devices, including 980 nm pump lasers, possess a delicate epitaxial structure, an 800 ^{o}C annealing can degrade the device's electrical and optical properties. It is possible to study the effects of this procedure on the emission characteristics of lasers, if the standard Si_3N_4 insulating layer is replaced by an Er-doped Al_2O_3 film and the sample is subject to the high temperature

annealing. Comparing the results with a control sample (same alumina insulating layer, but no thermal treatment), it is possible to evaluate the feasibility of this proposal.

5.2 Basic Semiconductor Laser Theory

Semiconductors are materials whose electrical conductivity values are usually between those of dielectrics and conductors such as metals. The particular crystal structure of the semiconductor's molecules and their respective interaction lead to the existence of energy bands, similar to energy levels in molecules, responsible for not only this conductivity effect, but light emission, absorption, and electrical rectification as well, among others. As an example, the crystal structure of Si and GaAs are shown in Fig. 5.2a and Fig. 5.2b, respectively.

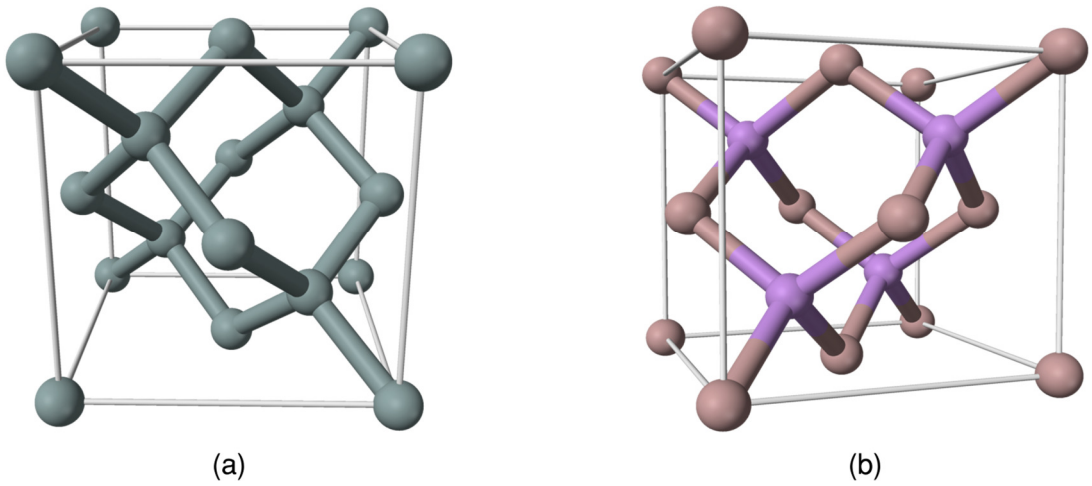

Fig. 5.2: Silicon (a) and Galium Arsenide (b) crystal structures.

By solving Schrödinger's equation for an electron in a periodic structure, for certain particular directions, it is possible to find the allowed energy states this electron can be in, often leading to gaps corresponding to "forbidden" energies [91]. Following the example above, Fig. 5.3a and Fig. 5.3b show the results for Si and GaAs. Since instead of well-defined discrete levels we have continuous "bands", this result is referred to as the band diagram of the material.

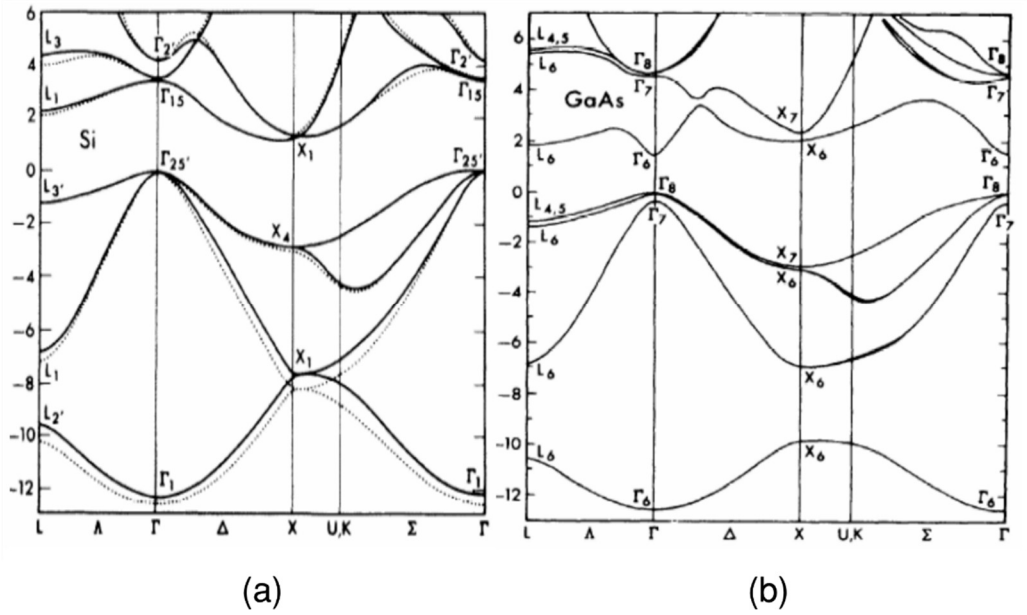

Fig. 5.3: Silicon (a) and Galium Arsenide (b) band diagrams.

Semiconductors can emit light via radiative carrier recombination processes, where an electron in the conduction band is combined with a hole from the valence band, and a photon possessing the energy difference between these bands (energy gap) is emitted. Although the only difference between the Si and GaAs crystal structures is the existence of two different atoms in GaAs, their band diagrams show a very important distinction: Si has an indirect gap. This means that the recombination process is usually non-radiative, since a phonon absorption or emission is necessary to shift the photon's momentum. A consequence of this fact is that Si is not an efficient light emitter, hampering the development of all-silicon integrated photonic circuits.

To understand the dynamics involved in a semiconductor laser, we can assume that it is composed of a waveguide with an active region, that is, where carriers can be excited and photons generated, enclosed by two mirrors forming a cavity. To induce light emission on this structure, an electrical current can be applied to create electron-hole pairs (electrons at the valence band are promoted to the conduction band, leaving a vacancy), that can be recombined radiatively. The rate of change of the pair (or carrier) density N can then be written as [92]:

$$\frac{dN}{dt} = \frac{\eta_i I}{qV} - R_{sp} - R_{st} - R_{nr} = \frac{\eta_i I}{qV} - \frac{N}{\tau} - R_{st}. \quad (5.1)$$

On this equation, η_i is the fraction of the current that is due to recombination in the active region, I is the applied current, q the electron charge and V the volume where carriers can be generated. The R_{sp}, R_{st} and R_{nr} are terms corresponding to the rate of recombination via spontaneous emission, stimulated emission, and non-radiative processes, respectively. The non-stimulated recombination terms can be written in terms of the average carrier lifetime τ.

Since photons are being generated, we can also write the respective density (N_p) rate of change as:

$$\frac{dN_p}{dt} = \Gamma\left(R_{sp} + R_{st}\right) - \frac{N_p}{\tau_p}, \quad (5.2)$$

where Γ is the confinement factor and τ_p is the average photon lifetime. The confinement factor is important because we are only interested in photons that remain inside the laser waveguide. Considering that these photons travel along the waveguide and can stimulate additional photon emissions, after distance ΔL, we can write:

$$N_p + \Delta N_p = N_p e^{g\Delta L}. \quad (5.3)$$

The quantity g introduced on this equation is called the gain coefficient, and represents the light intensity increase per unit length. If we consider a very small distance and introduce the group velocity v_g, Eq. 5.3 can be approximated as:

$$N_p + \Delta N_p = N_p(1 + g\Delta L) \rightarrow \Delta N_p = N_p g v_g \Delta t. \quad (5.4)$$

This leads us to:

$$\frac{\Delta N_p}{\Delta t} = R_{st} = N_p g v_g. \quad (5.5)$$

Considering a stationary state ($dN_p/dt = 0$), Eq. 5.2 becomes:

$$\frac{dN_p}{dt} = 0 = \Gamma\left(R_{sp} + N_p g v_g\right) - \frac{N_p}{\tau_p} \rightarrow N_p = \frac{\Gamma R_{sp}}{\tau_p - \Gamma g v_g}. \quad (5.6)$$

From this equation, we can see that as the term representing the photon increase ($\Gamma g v_g$) approaches the term representing the losses (τ_p), the number of photons tends to infinity. This is called the threshold condition, that is, when lasing starts to occur. It is important to notice that g depends on the injected current, and for $I > I_{th}$, $g = g_{th}$. This can be written as:

$$g = g_0 \ln\left(\frac{I}{I_{tr}}\right). \tag{5.7}$$

Here, I_{tr} is the transparency current (the necessary current so that the optical loss is effectively zero), and g_0 is the material gain coefficient.

It is possible to define a loss coefficient in terms of the waveguide attenuation coefficient α, the cavity length L, and the mirrors reflectivity R, so that at the threshold, since the gain approaches the total loss coefficient, we can write:

$$g_{th} \cong \alpha + \frac{1}{L}\ln\left(\frac{1}{R}\right). \tag{5.8}$$

Thus, Eq. 5.7 can be rewritten as:

$$\ln(I_{tr}) = \ln(I_{th}) + \frac{1}{g_0}\left[\alpha + \frac{1}{L}\ln\left(\frac{1}{R}\right)\right]. \tag{5.9}$$

This equation means that if we can determine I_{th}, the waveguide attenuation coefficient, and the laser mirror reflectivity, the material gain coefficient can be found. The threshold current can be experimentally determined by the behavior of the emitted light intensity in function of the applied current. A qualitative representation is shown in Fig. 5.4:

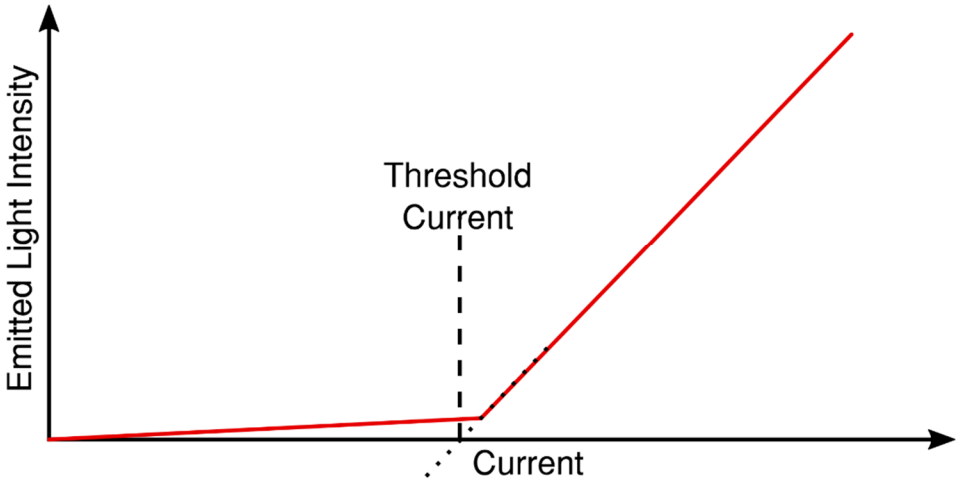

Fig. 5.4: Qualitative representation of the emitted light intensity in function of the applied current.

From this graph (also referred to as the L x I curve), we see that there is an abrupt change in the curve inclination (rate of photon emission), representing the threshold condition. By extrapolating the section with the highest inclination (above threshold), we can determine the threshold current at the point where the extrapolation crosses the current (x) axis at zero intensity (y).

To determine the waveguide attenuation coefficient, the concept of external (η_e) and internal (η_i) quantum efficiencies can be used. The external value is the ratio between the number of extracted photons and injected electrons, while the internal is relative to the number of photons generated internally. If we define the extraction efficiency (η_o) as the ratio between the number extracted and internal photons, we can write:

$$\eta_e = \eta_o \eta_i = \eta_i \frac{\alpha_m}{\alpha_T} = \eta_i \frac{\frac{1}{L} ln\left(\frac{1}{R}\right)}{\alpha + \frac{1}{L}\ln\left(\frac{1}{R}\right)} ; \qquad (5.10)\ (i)$$

$$\frac{1}{\eta_e} = \frac{1}{\eta_i} + \frac{1}{\eta_i}\frac{\alpha L}{\ln\left(\frac{1}{R}\right)} . \qquad (5.10)\ (ii)$$

This equation establishes a relationship between the internal quantum efficiency, waveguide attenuation coefficient, and the external quantum efficiency, which is straightforward to obtain experimentally from the above-threshold slope of the L x I curve (considering that light intensity from only one facet is measured):

$$\eta_e = 2\frac{\Delta P}{\Delta I}\frac{q}{E_{ph}} = 2\frac{\Delta P}{\Delta I}\frac{q\lambda}{hc}. \quad (5.11)$$

These equations allow us to obtain several characteristics of the laser by measuring the power output in function of the applied current, a very important conclusion if the performance of a laser needs to be evaluated, as will be demonstrated in the next sections.

5.3 Laser Design and Fabrication

The first step of the proposed investigation is the design of the lasers. Following up on the concept that this is going to be applied to an Er-doped waveguide amplifier, the emission wavelength needs to be suitable for erbium pumping. Since 980 nm is the most widely used wavelength on EDFAs, it is a convenient choice. To achieve this, a strained InGaAs/GaAs quantum well structure was chosen [93]. The development of the complete epitaxial structure is out of the scope of this document and can be found in the literature [94], [95]. The wafers were fabricated at Spire Semiconductors, containing the following layers:

Table 5-1: Epitaxial structure of the 980 nm laser.

Layer	Material	Mol. Fract. (x)	Thickness (μm)	Doping/Type	Dopant
13	GaAs	-	0.10	$> 5 \times 10^{19}$/p++	Zn
12	GaAs	-	0.10	$\sim 3 \times 10^{19}$/p+	Zn
11	In(x)GaP	0.49	0.19	1×10^{18}/p	Zn
10	In(x)GaP	0.49	0.91	6×10^{17}/p	Zn
9	In(x)GaP	0.49	0.05	2×10^{17}/p	Zn
8	GaAs	-	0.006	2×10^{17}/p	Zn
7	In(x)GaP	0.49	0.10	2×10^{17}/p	Zn
6	GaAs	-	0.10	-	-
5	InGa(x)As	0.17	0.007	-	-
4	GaAs	-	0.10	-	-
3	In(x)GaP	0.49	0.15	5×10^{17}/n	Si
2	In(x)GaP	0.49	1.05	1×10^{18}/n	Si
1	GaAs	-	0.5	$\sim 2 \times 10^{18}$/n+	Si
-	GaAs	-	Substrate	$> 2 \times 10^{18}$/n+	SiGa

The quantum well is composed of layers 4 to 6, and the resulting band structure is responsible for the 980 nm emission. Since the laser needs to be composed of a waveguide, InGaP layers (2, 3, 7, 9, 10 and 11) with higher doping concentration and lower refractive index serve as the cladding layers. Layer 8 is called an etch-stop layer, and its presence does not impact the electrical or optical characteristics of the device. The purpose of this layer is to ensure that the etching procedures involved the device fabrication stop at that exact point. The dopants and doping concentrations are chosen to provide suitable electrical characteristics and appropriate ohmic contacts.

The fabrication procedure is very similar to the ones described in section 4.1, using optical UV lithography. On samples containing the epitaxial structure from Table 5-1 (Fig. 5.5a), straight lines corresponding to the laser waveguides are written, with 7 µm of width. The sample is then etched in a $1H_2SO_4 + 8H_2O_2 + 40H_2O$ solution for 30 s, and in a $3HCl + 1H_2O$ solution for 90 s. As a result, layers 13 and 12, and 11 through 9 are removed from the exposed regions (Fig. 5.5b).

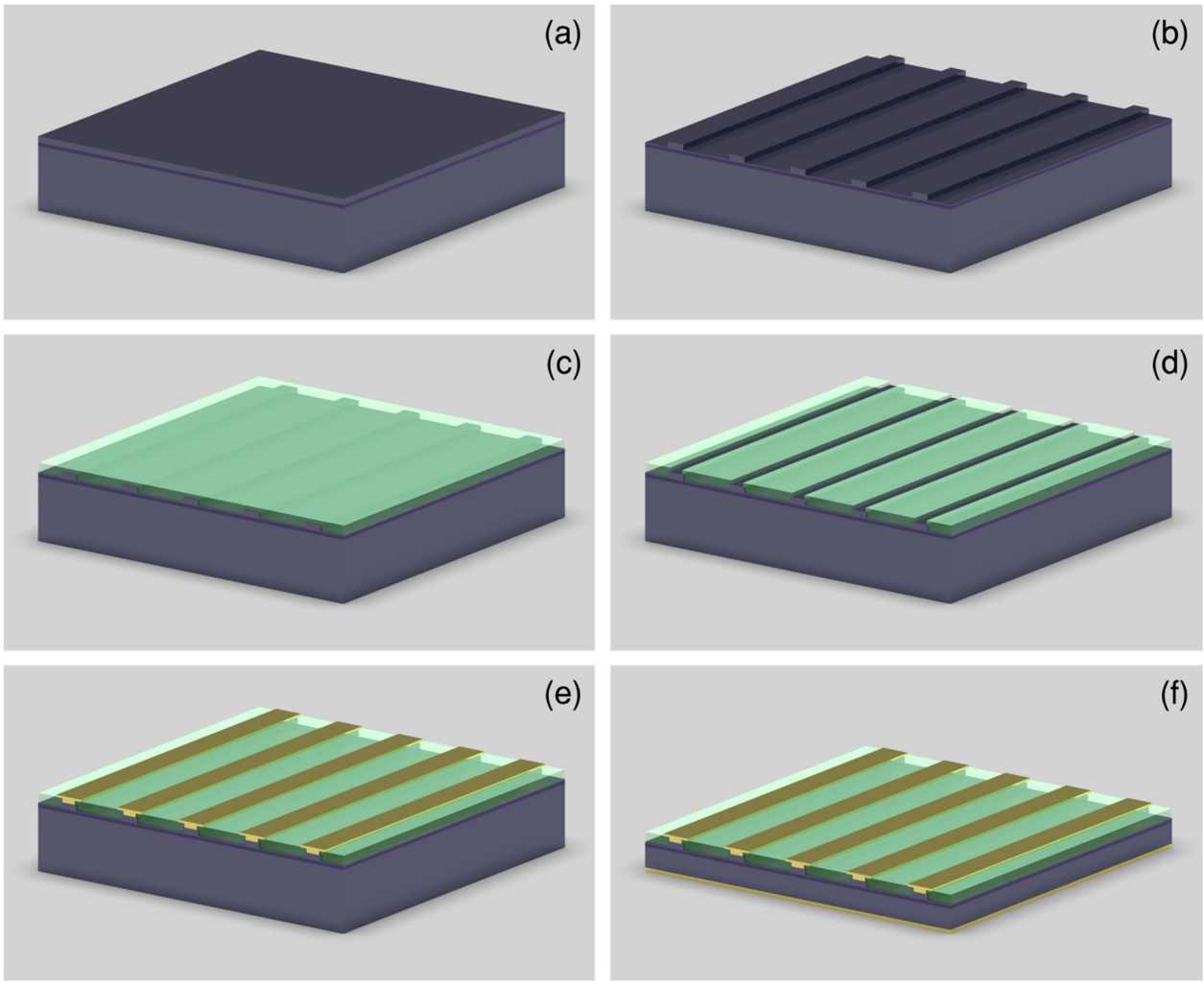

Fig. 5.5: Laser fabrication steps: InGaAs/GaAs QW sample (a), ridges etching (b), insulating layer deposition (c), window opening (d), metal deposition and lift-off (e), trimming and n contact deposition (f).

The next step is the deposition of a dielectric layer, responsible for the insulation between the several fabricated lasers. The typical material is Si_3N_4, but in our case, we want to study the possibility of using Al_2O_3, to evaluate the thermal annealing effect on the laser. To do that, the same procedure described in section 3.1 was used, but during a shorter deposition time (1 h) resulting in a film with approximately 100 nm of thickness (Fig. 5.5c). At this point, half of the samples were subject to the 800 °C thermal annealing.

To apply the electrical current, ohmic contacts need to be formed on top (and bottom) of the laser waveguides. Thus, a new etching step is necessary, to form 5 µm

wide windows on the Al_2O_3 layer. After the pattern is marked on the photoresist by optical lithography, the etching is performed via reactive ion etching (RIE). The plasma chamber pressure is 30 mTorr, containing $SiCl_4$ and Ar at flow rates of 10 sccm and 5 sccm, respectively (Fig. 5.5d).

Finally, another (wider) photoresist window is created, and a Ti/Pt/Au alloy is deposited via electron-beam deposition on top of the sample to form the p electrical contacts. Using the lift-off technique, part of the metallic film between the lasers (and thus outside the photoresist window) is simultaneously removed with the photoresist, due to the specific relationship between its height and those of the photoresist and waveguides (Fig. 5.5e).

To form the n (bottom) electrical contact, the sample is trimmed to 100 µm, and an Au/Ge/Ni alloy is deposited on the bottom part (Fig. 5.5f). A rapid thermal annealing (RTP) at 420 °C for 30s finishes this ohmic contact. The metallic depositions and trimming were performed by the Device Research Lab's (LPD) technician Antônio Augusto von Zuben.

The last fabrication step is to cleave each sample, so the resulting facets are perfectly smooth mirrors and a thorough characterization can then be performed. This procedure also defines laser cavity length, ranging between 250 µm and 1350 µm. Microscopy and scanning electron microscopy (SEM) photos of a completed laser are shown in Fig. 5.6.

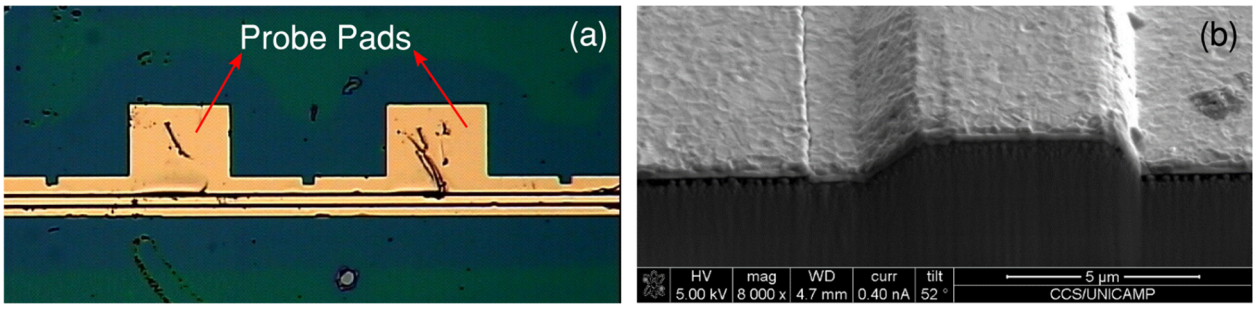

Fig. 5.6: Top-view microscopy photo (a) and SEM picture of the facet (b) of a completed laser. The large squares are pads to assist the electrical probe contact.

5.4 Laser characterization

Before the main characterization of the fabricated lasers, unprocessed InGaAs/GaAs QW samples were subject to annealing at different temperatures for 30 min, with the intent of measuring the photoluminescence of the material for each temperature. For values of 600 °C and below, no visual change was observed, but at 800 °C the sample was severely damaged. A second attempt was made, but the Al_2O_3 film was deposited on these samples before the thermal annealing. No visible damage was observed, and the PL results, acquired using the setup from Fig. 3.2a, are shown in Fig. 5.7.

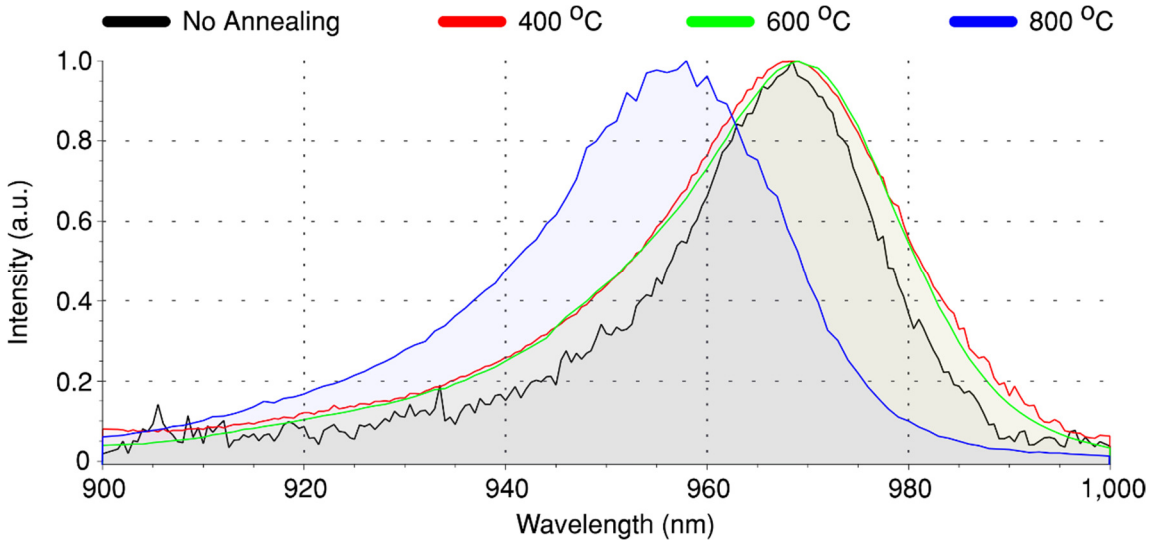

Fig. 5.7: Photoluminescence spectra for unprocessed InGaAs/GaAs QW samples subject to thermal annealing at different temperatures.

The unnormalized amplitude for each measurement is different, which can be verified by the different noise amplitudes on the graph, but it can be mainly attributed to small alignment differences. There are, however, two major characteristics that changed considerably. The first, is that the spectrum is broadened after the annealing, and the FWHM increases from 21 nm to 28 nm. The second, is that the peak emission wavelength suffers a blueshift for the procedure at 800 °C, going from 967 nm to 958 nm, evidence of an alteration at the quantum well structure.

To characterize the fabricated lasers, the experimental setup shown in Fig. 5.8 was used.

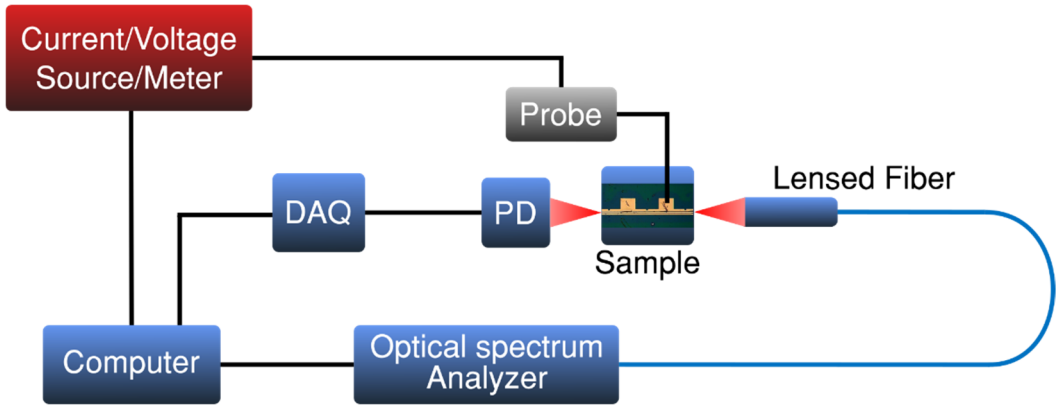

Fig. 5.8: Experimental setup used in the lasers' characterization measurements.

The first measurement performed was the electrical current value in function of the applied voltage (also called the I x V curve). Using a Keithley 2400 Sourcemeter as both the voltage source and current meter, one of its terminals is connected to an electrical probe, aligned to touch one of the pads from Fig. 5.6a (p contact) using a microscope. The bottom (n contact) is in direct contact with a gold-coated metallic sample holder, which is in turn connected to a second terminal on the Keithley 2400. By sweeping the applied voltage and measuring the resulting current, the I x V curves for various samples are obtained, shown in Fig. 5.9.

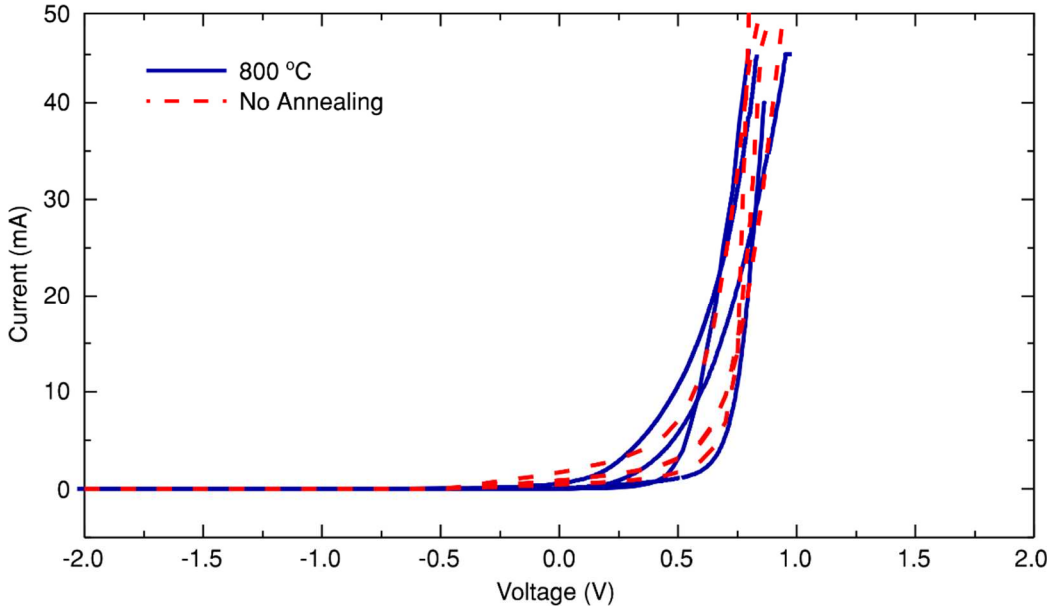

Fig. 5.9: I x V curves for various annealed (800 °C) and non-annealed laser samples,

Since the samples are composed of a double heterostructure, the I x V curves are expected to be similar to a diode (p-n junction). From the results, we can see that this behavior is confirmed, and there are no significant differences between the annealed and non-annealed curves. A simplified diode characterization model consists of a series and a parallel resistance connected to an ideal diode. These values can be obtained by the respective linear sections slopes on the I x V curve. For the series resistance (positive voltage slope) the average value for the non-annealed samples is (4 ± 2) Ω, which increased to (8 ± 3) Ω. For the parallel resistance (negative voltage slope), the average value is 500 kΩ for both cases. Although the series resistance increased for the annealed samples, it is not a cause for concern, since it is still within typical values.

The next measurement to be analyzed is the output spectrum. The optical output from one side of the laser is collected by a lensed fiber, connected to a HP 70951A optical spectrum analyzer. By setting different current values on the Keithley 2400, the output spectra shown in Fig. 5.10 have been measured for one annealed sample.

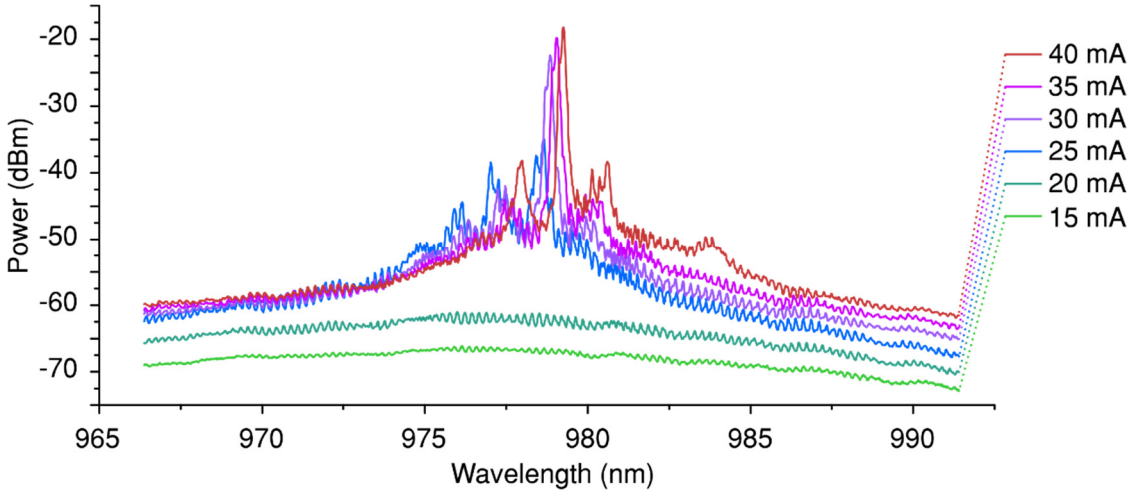

Fig. 5.10: Laser output spectra for different values of electrical current applied.

We can see that as the applied current increases, so does the output power. Between 20 mA and 25 mA, there is an abrupt increase and narrow peaks are defined, indicating that the threshold current is in this range. The peak wavelength suffers a small redshift, mainly due to thermal effects. Small oscillations are present on every spectrum, a common characteristic of Fabry-Perot laser cavities.

If we compare the above-threshold spectrum from one annealed sample to the output from a non-annealed one, the results in Fig. 5.11 can be obtained.

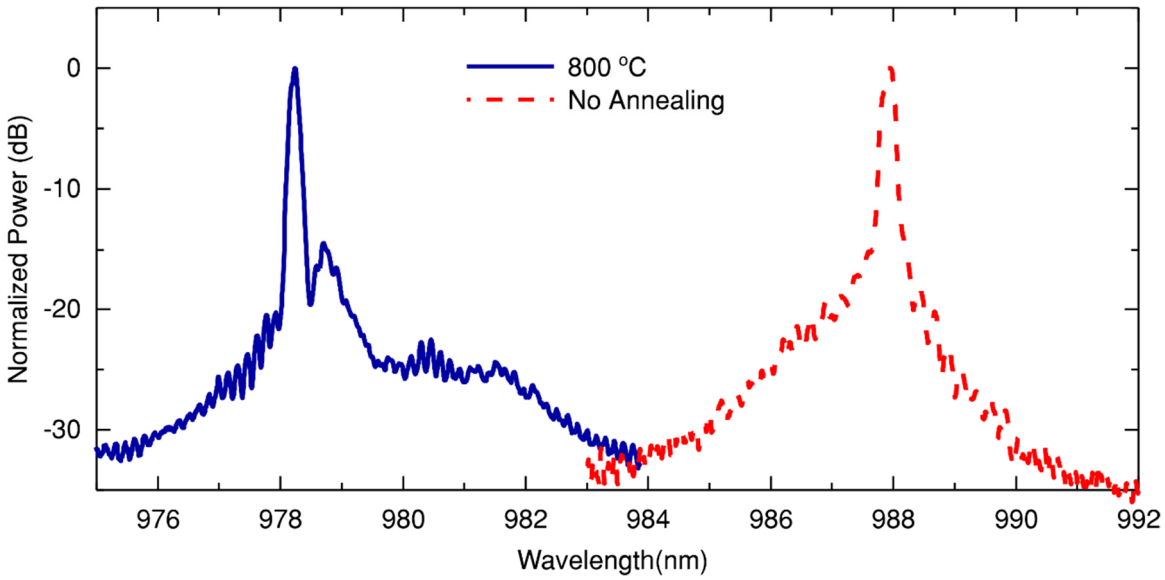

Fig. 5.11: Comparison between the spectra from annelaed and non-annealed samples.

These curves behave similarly to the photoluminescence measurements and show a blueshift from 988.1 nm to 978.4 nm when the annealing at 800 °C is performed. Most of the laser samples presented peak emissions well above 980 nm, thus we can affirm that, at least in this respect, the thermal annealing has been beneficial to the laser characteristics, since the erbium absorption cross-section at the 980 nm region can decrease beyond a ±5 nm range.

The last measurements are the L x I curves for various samples with different cavity lengths. On this experiment, the applied current is swept from 0 to 45 mA, while a photodiode measures the output optical intensity from one side of the laser and sends the data to a National Instruments DAQ. To illustrate the difference between annealed and non-annealed samples, typical results for 250 μm cavities are shown in Fig. 5.12.

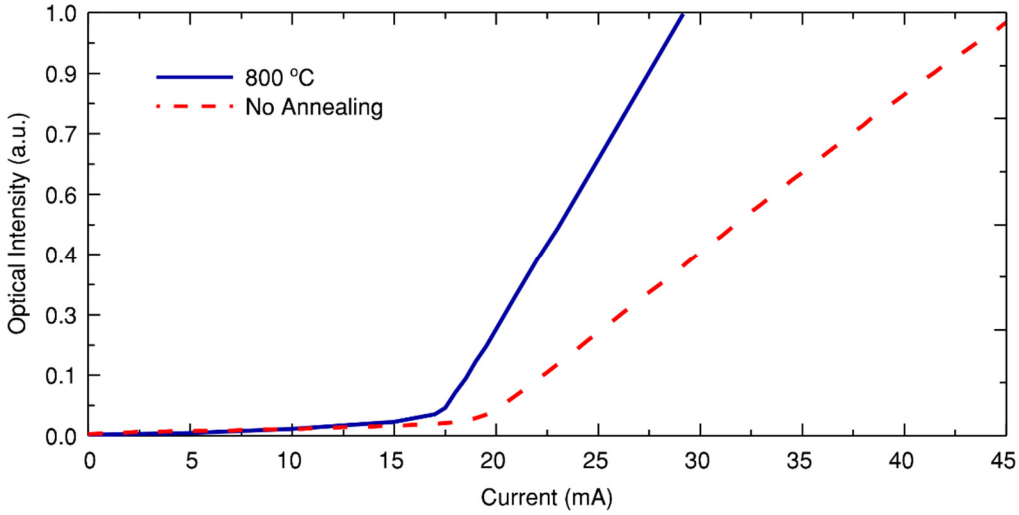

Fig. 5.12: L x I curves for annealed and non-annealed 250 μm cavity lasers.

It is clear that after the annealing not only the slope changed (higher quantum efficiency), but the threshold value also decreased. Before concluding that the laser benefited from the annealing, a more complete assessment is needed. To this end, the threshold currents from various samples with varying cavity lengths have been measured, and the graph from Fig. 5.13 was constructed.

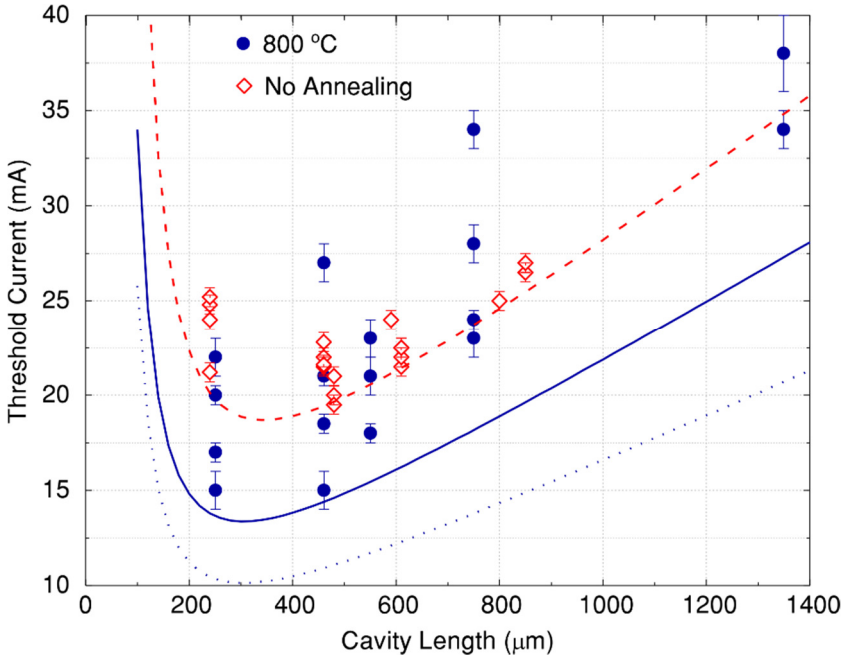

Fig. 5.13: Threshold current in function of cavity length for several samples. Only the lowest values are considered when the fitted curves are calculated.

The optimal cavity length (lowest threshold current) for the measured lasers is within the 300 μm – 400 μm range. For shorter cavities I_{th} increases, since the mirror losses are higher than the gain, which is limited by the cavity length. When the cavity is too long, however, intrinsic losses start to become significant. Once again, we observe that the threshold currents for annealed samples are generally lower, with a few exceptions.

From the L x I curves and Eqs. 5.10 and 5.11, the external and internal quantum efficiencies can be obtained, along with the laser intrinsic loss coefficients. For the non-annealed samples, $\eta_i \approx 43\%$ and $\alpha \approx 18$ cm^{-1}, while for the annealed ones, $\eta_i \approx 61\%$ and $\alpha \approx 15$ cm^{-1}. With these values determined, the lowest current values for each cavity length in Fig. 5.13 can be fitted by Eq. 5.9 and the material gain coefficients $g_0 =$ 70 cm^{-1} and $g_0 = 79$ cm^{-1} could be obtained for the non-annealed and annealed samples, respectively. The reason why only the lowest values are considered is that higher values are usually obtained from non-optimal samples or measurements, thus the real material properties cannot be satisfactorily determined. The probability of a lower threshold

current being measured by accident or poor experimental conditions is much lower than the measurement of a higher value.

On Fig. 5.13, the dashed red and dotted blue lines represent Eq. 5.9 plots with the obtained values considered. We can see that for the non-annealed case, the curve matches the lower threshold current values very well, while for the annealed case, there is a significant disagreement. Since the threshold currents deviation is higher for this case, it makes sense to change the calculated internal quantum efficiency value in order to obtain a better fit. The best fit, indicated by the solid blue line, is obtained for $\eta_i = 47\%$, still higher than the annealed case. A summary of the obtained values can be seen in Table 5-2.

Table 5-2: Summary of the characterization results from the fabricated lasers.

	Not Annealed	Annealed
Peak Wavelength (nm)	988.1	978.4
Diode Series Resistance (Ω)	4 ± 2	8 ± 3
Diode Parallel Resistance (kΩ)	500	500
Lowest Threshold Current (mA)	19	15
Calculated Internal quantum efficiency	43%	61%
Adjusted Internal quantum efficiency	43%	47%
Loss Coefficient (cm^{-1})	18	15
Gain Coefficient (cm^{-1})	70	80

These results show an overall improvement for the annealed lasers, and a possible explanation is the improvement of the insulating characteristics of the film after the annealing, since air pockets and impurities can be removed during this process. Additionally, the possible improvement of the internal quantum efficiency can indicate a reduction in the density of defects and current leakage.

Considering these results, and the fact that the sample was severely damaged during the thermal annealing when the Al_2O_3 film was not present, we can speculate that the most critical issue is group V elements evaporation. Our epitaxial structure contains GaAs, InGaAs and InGaP, and both As and P possess sublimation points near 600 °C, well below the annealing temperature (800 °C). When the sample is heated above the sublimation temperature, group V atoms start to deplete while group III atoms start to migrate, forming metallic clusters. When the alumina film is present, however, this effect is mitigated, since no vapor can exit the structure.

Therefore, a safe conclusion that can be made is that the high temperature annealing process necessary for the Er-doped films optimal performance does not have a negative impact in the behavior of III-V semiconductor lasers, demonstrating that alumina is a suitable material for insulating layers on lasers, able to replace the standard Si_3N_4. In addition, Al_2O_3 has the advantage of being an excellent material for Er-doping, and thus can bring new applications possibilities to III-V integrated photonics, such as compact integrated optical amplifiers.

5.5 Chapter Summary

In this appendix, a conceptual device involving the integration of a waveguide amplifier and the respective pump laser on III-V materials has been presented, along with the concern that the thermal annealing required to achieve the optimal Er-doped film absorption and emission properties may damage the delicate epitaxial structure present on semiconductor lasers. For this, the basic semiconductor laser theory was quickly reviewed, and the epitaxial design and subsequent laser fabrication procedure has been discussed. The characterization experiments were described, and the obtained results demonstrate that when the sample is covered by the Al_2O_3 film, there is no deterioration of the laser electrical and optical characteristics. This study, in fact, hints on the opposite of that.

6. Conclusion

In this thesis, the relevant studies, ideas, experiments, results and conclusions of the application of erbium-doped Al_2O_3 films to integrated photonics have been described in detail. The work has been executed in two main fronts: the application of these films on devices based on silicon ring resonators, and the evaluation of the possibility of a monolithic III-V optical amplifier. Both fronts yielded important scientific contributions to the integrated photonics field.

Regarding the application of Er-doped Al_2O_3 films on Si devices, a method to reduce insertion losses originated on ring resonators has been proposed. It consists of the employment of the films on top of Si photonics devices, and the only post-processing procedure required is the film deposition, being completely compatible with CMOS processes. Experimental results show signal enhancement of 1 dB for single rings, and 2.6 dB for photonic molecules. Although not an impressive result for an amplifier, it can crucially impact the feasibility of complex circuits where several of these devices are cascaded.

Not limited to loss reduction, this method can also be used to obtain devices with higher quality factors, without increasing the occupied area. The model developed shows that for most high-Q applications there is a trade-off between ring radius and loss, but when a gain media is considered, in this case the Er-doped cladding, this trade-off is minimized and very compact devices with high-Q and low insertion losses are possible. From the experimental results, for a device with Q = 50000 the effective loss reduction is more than 3 dB.

Considering the application of the developed films on III-V devices, which is described in detail in Chapter 5, a monolithic erbium-doped waveguide amplifier is an attractive idea. However, since some III-V epitaxial structures (especially those involved in lasers) can be very sensitive to high-temperatures, there is a concern of whether such

device is possible, since the $Al_2O_3:Er^{3+}$ film requires thermal annealing at 800 °C to optimize its optical absorption and emission characteristics. By fabricating and characterizing InGaAs/GaAs QW lasers emitting at 980 nm using annealed and non-annealed Er-doped alumina as the insulating material, it became clear that as long as there is a robust protective layer preventing group V (As and P) materials from evaporating, no negative impact on the laser characteristics will occur. Thus, this material can be safely used for light amplification on III-V devices, despite the high-temperature annealing process involved.

Overall, the work described in this thesis evidences the opening of many application possibilities in integrated photonics, from compact and efficient photonic filters/routers on Si, to monolithic optical amplifiers on III-V materials. Future work on the topics discussed here include, but are not limited to, the experimental study of the maximum Q-factor enhancement of a Si ring resonator and photonic molecule in function of the occupied area, the study of complex routing circuits based on resonators and the maximum concatenable number of devices before complete signal degradation, and finally the execution and characterization of a monolithic EDWA.

Publications

Conference papers/presentations:

- P. F. Jarschel, L. Barea, A. A. v. Zuben, R. B. Merlo and N. Frateschi, "Monolithic Erbium-Doped Al2O3 Waveguide Amplifier," in *Latin America Optics and Photonics Conference (LAOP),* Sao Sebastiao, SP, Brazil, 2012.
- P. F. Jarschel, L. A. M. Barea, M. C. M. M. Souza, F. Vallini, A. A. G. V. Zuben, A. C. Ramos, R. B. Merlo and N. C. Frateschi, "Erbium Doped Al2O3 films for integrated III–V photonics," in *Symposium on Microelectronics Technology and Devices (SBMicro),* Curitiba, PR, Brazil, 2013.
- P. F. Jarschel, M. C. M. M. Souza, A. A. G. V. Zuben, A. C. Ramos, R. B. Merlo and N. C. Frateschi, "Enabling III–V integrated photonics with Er-doped Al2O3 films," in *Symposium on Microelectronics Technology and Devices (SBMicro)*, Aracaju, SE, Brazil, 2014.
- P. F. Jarschel, M. C. Souza, R. B. Merlo and N. C. Frateschi, "Self-Amplified Filter Fabricated in a SOI Photonics Foundry," in *Conference on Lasers and Electro-Optics (CLEO)*, San Jose, CA, United States, 2017.

Publications on peer-reviewed journals:

- L. A. M. Barea, F. Vallini, P. F. Jarschel and N. C. Frateschi, "Silicon technology compatible photonic molecules for," *Applied Physics Letters,* vol. 103, no. 20, p. 201102, 2013.
- P. F. Jarschel, M. C. M. M. Souza, R. B. Merlo and N. C. Frateschi, "Loss Compensation in Microring-Based Si Photonics Devices via Er3+ Doped Claddings," *IEEE Photonics Journal,* vol. 10, no. 4, 2018.

Additional Publications:

- F. Vallini, D. S. L. Figueira, P. F. Jarschel, L. A. M. Barea, A. A. G. Von Zuben, and N. C. Frateschi, "Effects of Ga+ milling on InGaAsP quantum well laser with mirrors milled by focused ion beam", *Journal of Vacuum Science & Technology B*, vol. 27, no. 25, 2009.
- D. S. L. Figueira, L. A. M. Barea, F. Vallini, Paulo F. Jarschel, R. Lang, and N. C. Frateschi, "a-SiOx<Er> active photonic crystal resonator membrane fabricated by focused Ga+ ion beam", *Optics Express*, vol. 20, no. 17, 2012.
- O. Florez, P. F. Jarschel, Y. A. V. Espinel, C. M. B. Cordeiro, T. P. Mayer Alegre, G. S. Wiederhecker and P. Dainese, "Brillouin scattering self-cancellation", *Nature Communications*, vol. 7, 2016.
- P. F. Jarschel, L. S. Magalhaes, I. Aldaya, O. Florez, and P. Dainese, "Fiber taper diameter characterization using forward Brillouin scattering", *Optics Letters*, vol. 43, no. 5, 2018.

References

[1] J. M. Norman, From Gutenberg to the Internet, Norman Publishing, 2005.

[2] D. L. Hutt, K. J. Snell and P. A. Bélanger, "Alexander Graham Bell's Photophone," *Optics and Photonics News,* vol. 4, no. 6, pp. 20-25, 1993.

[3] J. Ballato and P. Dragic, "Glass: The Carrier of Light - A Brief History of Optical Fiber," *Applied Glass Science,* vol. 7, no. 4, pp. 413-422, 2016.

[4] H. Hopkins and N. S. Kapany, "A flexible fibrescope, using static scanning," *Nature,* vol. 173, pp. 39-41, 1954.

[5] J. Hecht, City of Light, Oxford University Press, 2004.

[6] G. P. Agrawal, "Optical Communication: Its History and Recent Progress," in *Optics in Our Time*, Springer, 2016, pp. 177-199.

[7] M. Abubakr, "Recession: Effects on Internet and Web performance," 26 October 2008. [Online]. Available: https://blogs.msdn.microsoft.com/perfdude/2008/10/26/recession-effects-on-internet-and-web-performance/. [Accessed 14 September 2017].

[8] D. J. Richardson, J. M. Fini and L. E. Nelson, "Space-division multiplexing in optical fibres," *Nature Photonics,* vol. 7, p. 354–362, 2013.

[9] G. E. Moore, "Cramming More Components onto Integrated Circuits," *Electronics,* pp. 114-117, 1965.

[10] F. Poletti, M. N. Petrovich and D. J. Richardson, "Hollow-core photonic bandgap fibers: technology and applications," *Nanophotonics,* vol. 2, no. 5-6, 2013.

[11] K. Saitoh, "Multicore Fiber Technology," *Journal of Lightwave Technology,* vol. 34, no. 1, pp. 55-66, 2016.

[12] D. Thomson, A. Zilkie, J. E. Bowers, T. Komljenovic, G. T. Reed, L. Vivien, D. Marris-Morini, E. Cassan, L. Virot, J. M. Fedeli, J. M. Hartmann, J. H. Schmid, D.-X. Xu, F. Boeuf, P. O'Brien, G. Z. Mashanovich and M. Nedeljkovic, "Roadmap on silicon photonics," *Journal of Optics,* vol. 18, no. 7, 2016.

[13] K. Wen, H. Guan, D. M. Calhoun, D. Donofrio and J. Shalf, "Silicon photonic memory interconnect for many-core architectures," in *High Performance Extreme Computing Conference (HPEC), IEEE*, Waltham, MA, USA, 2016.

[14] G. R. J. Brouckaert, J. V. Campenhout, D. V. Thourhout and R. Baets, "Heterogeneous Integration of III-V Active Devices on a Silicon-on-Insulator Photonic Platform," in *4th IEEE International Conference on Group IV Photonics*, 2007.

[15] M. Borselli and O. Painter, "High-Q Microresonators as Lasing Elements for Silicon Photonics," Caltech, 2010.

[16] Z. Fang and C. Z. Zhao, "Recent Progress in Silicon Photonics: A Review," *ISRN Optics,* vol. 2012, 2012.

[17] C. Husko, T. D. Vo, B. Corcoran, J. Li, T. F. Krauss and B. J. Eggleton, "Ultracompact all-optical XOR logic gate in a slow-light silicon photonic crystal waveguide," *Optics Express,* vol. 19, no. 21, pp. 20681-20690, 2011.

[18] Y. Fu, X. Hu and Q. Gong, "Silicon photonic crystal all-optical logic gates," *Physics Letters A,* vol. 377, no. 3-4, pp. 329-333, 2013.

[19] K. Li and A. Foster, "1.25-Gb/s All-Optical NAND/AND Logic Gates in a Hydrogenated Amorphous Silicon Waveguide," in *CLEO*, San Jose, 2017.

[20] F. Y. Gardes, D. J. Thomson, N. G. Emerson and G. T. Reed, "40 Gb/s silicon photonics modulator for TE and TM polarisations," *Optics Express,* vol. 19, no. 12, 2011.

[21] J.-H. Han, F. Boeuf, J. Fujikata, S. Takahashi, S. Takagi and M. Takenaka, "Efficient low-loss InGaAsP/Si hybrid MOS optical modulator," *Nature Photonics,* vol. 11, no. 8, p. 486–490, 2017.

[22] T. Hiraki, T. Aihara, K. Hasebe, K. Takeda, T. Fujii, T. Kakitsuka, T. Tsuchizawa, H. Fukuda and S. Matsuo, "Heterogeneously integrated III–V/Si MOS capacitor Mach–Zehnder modulator," *Nature Photonics,* vol. 11, no. 8, p. 482–485, 2017.

[23] W. Bogaerts, P. D. Heyn, T. V. Vaerenbergh, K. D. Vos, S. K. Selvaraja, T. Claes, P. Dumon, P. Bienstman, D. V. Thourhout and R. Baets, "Silicon microring resonators," *Laser & Photonics Reviews,* vol. 6, no. 1, pp. 47-73, 2012.

[24] S. Feng, T. Lei, H. Chen, H. Cai, X. Luo and A. W. Poon, "Silicon photonics: from a microresonator perspective," *Laser Photonics Rev.,* vol. 6, no. 2, p. 145–177, 2012.

[25] G. T. Reed, G. Mashanovich, F. Y. Gardes and D. J. Thomson, "Silicon optical modulators," *Nature Photonics,* vol. 1, no. 65, p. 660, 2010.

[26] G. Li, A. V. Krishnamoorthy, I. Shubin, J. Yao, Y. Luo, H. Thacker, X. Zheng, K. Raj and J. E. Cunningham, "Ring Resonator Modulators in Silicon for Interchip Photonic Links," *IEEE Journal of Selected Topics in Quantum Electronics ,* vol. 19, no. 6, pp. 95 - 113, 2013.

[27] Y. Tian, L. Zhang, R. Ji, Y. L., P. Zhou, H. Chen, J. Ding, W. Zhu, Y. Lu, L. Jia, Q. Fang and M. Yu, "Proof of concept of directed or/nor and and/nand logic circuit consisting of two parallel microring resonators," *Optics Letters,* vol. 36, no. 9, pp. 1650-1652, 2011.

[28] F. Xia, L. Sekaric and Y. Vlasov, "Ultracompact optical buffers on a silicon chip," *Nature Photonics,* vol. 1, p. 65, 2006.

[29] B. E. Little, S. T. Chu, P. P. Absil, J. V. Hryniewicz, F. G. Johnson, F. Seiferth, D. Gill, V. Van, O. King and a. M. Trakalo, "Very high-order microring resonator filters for wdm applications," *IEEE Photonics Technology Letters,* vol. 16, no. 10, p. 2263–2265, 2004.

[30] A. N. Tait, A. X. Wu, T. F. d. Lima, E. Zhou, B. J. Shastri, M. A. Nahmias and P. R. Prucnal, "Microring Weight Banks," *IEEE Journal of Selected Topics in Quantum Electronics,* vol. 22, no. 6, p. 5900214, 2016.

[31] M. Dasic and M. A. Popovic, "Minimum Drop-Loss Design of Microphotonic Microring-Resonator Channel Add-Drop Filters," in *20th Telecommunications Forum TELFOR, IEEE*, 2012.

[32] A. Vorckel, M. Monster, W. Henschel, P. H. Bolivar and H. Kurz, "Asymmetrically coupled silicon-on-insulator microring," *IEEE Photonics Technology Letters,* vol. 15, no. 7, pp. 921-923, 2003.

[33] R. Mears, L. Reekie, I. Jauncey and D. Payne, "Low-noise erbium-doped fibre amplifier operating at 1.54μm," *Electronics Letters,* vol. 23, no. 19, pp. 1026-1028, 1987.

[34] Z. Li, A. Heidt, J. Daniel, Y. Jung, S. Alam and D. Richardson, "Thulium-doped fiber amplifier for optical communications at 2μm," in *OFC/NFOEC*, 2013.

[35] S. Saini, J. Bowser, R. Enck, V. Luciani, P. Heim and M. Dagenais, "A semiconductor optical amplifier with high saturation power, low noise figure and low polarization dependent gain over the C-band," in *The 17th Annual Meeting of the IEEE Lasers and Electro-Optics Society*, Rio Grande, Puerto Rico, 2004.

[36] G. N. v. d. Hoven, R. J. I. M. Koper, A. Polman, C. v. Dam, J. W. M. v. Uffelen and M. K. Smit, "Net optical gain at 1.53 μm in erdoped al2o3 waveguides on silicon," *Applied Physics Letters,* vol. 68, no. 14, pp. 1886-1888, 1996.

[37] J. D. B. Bradley, L. Agazzi, D. Geskus, F. Ay, K. Wörhoff and M. Pollnau, "Gain bandwidth of 80 nm and 2 dB/cm peak gain in Al2O3:Er3+ optical amplifiers on silicon," . *Opt. Soc. Am. B,* vol. 27, no. 2, pp. 187-196, 2010.

[38] S. A. Vázquez-Córdova, M. Dijkstra, E. H. Bernhardi, F. Ay, K. Wörhoff, J. L. Herek, S. M. García-Blanco and M. Pollnau, "Erbium-doped spiral amplifiers with 20 dB of net gain on silicon," *Optics Express,* vol. 22, no. 21, pp. 25993-26004, 2014.

[39] G. N. v. d. Hoven, E. Snoeks, A. Polman, C. v. Dam, J. W. M. v. Uffelen and M. K. Smit, "Upconversion in Er-implanted Al2O3 waveguides," *Journal of Applied Physics,* vol. 79, no. 3, 1996.

[40] A. Polman, "Exciting erbium-doped planar optical amplifier materials," in *Proc. SPIE 3942, Rare-Earth-Doped Materials and Devices IV*, San Jose, CA, United States, 2000.

[41] L. Wang, R. Guo, B. Wang, X. Wang and Z. Zhou, "Hybrid Si3N4-Er/Yb/Y silicate waveguide amplifier with 1.25dB/cm internal gain," in *IEEE 9th International Conference on Group IV Photonics (GFP)*, San Diego, CA, United States, 2012.

[42] L. Agazzi, J. D. B. Bradley, M. Dijkstra, F. Ay, G. Roelkens, R. Baets, K. Wörhoff and M. Pollnau, "Monolithic integration of erbium-doped amplifiers with silicon-on-insulator waveguides," *Optics Express,* vol. 18, no. 26, pp. 27703-27711, 2010.

[43] A. Tengattini, D. Gandolfi, N. Prtljaga, A. Anopchenko, J. M. Ramírez, F. F. Lupi, Y. Berencén, D. Navarro-Urrios, P. Rivallin, K. Surana, B. Garrido, J.-M. Fedeli and L. Pavesi, "Toward a 1.54 m Electrically Driven Erbium-Doped Silicon Slot Waveguide and Optical Amplifier," *Journal of Lightwave Technology,* vol. 31, no. 3, pp. 391-397, 2013.

[44] C. A. Barrios and M. Lipson, "Electrically driven silicon resonant light emitting device based on slot-waveguide," *Optics Express,* vol. 13, no. 25, 2005.

[45] D. Korn, M. Lauermann, S. Koeber, P. Appel, L. Alloatti, R. Palmer, P. Dumon, W. Freude, J. Leuthold and C. Koos, "Lasing in silicon–organic hybrid waveguides," *Nature Communications,* vol. 7, 2016.

[46] A. Biberman, M. J. Shaw, E. Timurdogan, J. B. Wright and M. R. Watts, "Ultralow-loss silicon ring resonators," *Optics Letters,* vol. 37, no. 20, pp. 4236-4238, 2012.

[47] P. F. Jarschel, L. Barea, A. A. v. Zuben, R. B. Merlo and N. Frateschi, "Monolithic Erbium-Doped Al2O3 Waveguide Amplifier," in *Latin America Optics and Photonics Conference (LAOP)*, Sao Sebastiao, SP, Brazil, 2012.

[48] P. F. Jarschel, L. A. M. Barea, M. C. M. M. Souza, F. Vallini, A. A. G. V. Zuben, A. C. Ramos, R. B. Merlo and N. C. Frateschi, "Erbium Doped Al2O3 films for integrated III–V photonics," in *Symposium on Microelectronics Technology and Devices (SBMicro)*, Curitiba, PR, Brazil, 2013.

[49] P. F. Jarschel, M. C. Souza, R. B. Merlo and N. C. Frateschi, "Self-Amplified Filter Fabricated in a SOI Photonics Foundry," in *Conference on Lasers and Electro-Optics (CLEO)*, San Jose, CA, United States, 2017.

[50] P. F. Jarschel, M. C. M. M. Souza, R. B. Merlo and N. C. Frateschi, "Loss Compensation in Microring-Based Si Photonics Devices via Er3+ Doped Claddings," *IEEE Photonics Journal,* vol. 10, no. 4, 2018.

[51] P. F. Jarschel, M. C. M. M. Souza, A. A. G. V. Zuben, A. C. Ramos, R. B. Merlo and N. C. Frateschi, "Enabling III–V integrated photonics with Er-doped Al2O3 films," in *Symposium on Microelectronics Technology and Devices (SBMicro)*, Aracaju, SE, Brazil, 2014.

[52] R. Maurer, D. Keck and P. Schulz, "Optical Waveguide Fibers". United States of America Patent 3.711.262, 1970.

[53] Cisco, "Fiber Types in Gigabit Optical Communications," 4 April 2008. [Online]. Available: https://www.cisco.com/c/en/us/products/collateral/interfaces-modules/transceiver-modules/white_paper_c11-463661.html. [Accessed 9 September 2017].

[54] W. S. Mallory, "The Distribution of Energy in the Spectrum of Erbium Oxide," *Physical Review,* vol. 14, no. 54, 1919.

[55] R. Paschotta, "Erbium-doped Gain Media," [Online]. Available: https://www.rp-photonics.com/erbium_doped_gain_media.html. [Accessed 19 September 2017].

[56] L. R. Tessler, J. L. Coffer, J. Ji and R. A. Senter, "Erbium environment in silicon nanoparticles," *Journal of Non-Crystalline Solids,* Vols. 299-302, pp. 673-677, 2002.

[57] D. S. L. Figueira and N. C. Frateschi, "Estruturas fotônicas baseadas em Silício," UNICAMP, Campinas, SP, Brazil, 2013.

[58] R. Paschotta, Field Guide to Lasers, SPIE, 2008.

[59] R. Paschotta, "Tutorial on Fiber Amplifiers," [Online]. Available: https://www.rp-photonics.com/tutorial_fiber_amplifiers1.html. [Accessed 19 September 2017].

[60] G. N. v. d. Hoven, J. A. v. d. Elsken, A. Polman, C. v. Dam, K. W. M. v. Uffelen and M. K. Smit, "Absorption and emission cross sections of Er3+ in Al2O3 waveguides," *Applied Optics,* vol. 36, no. 15, p. 3338–3341, 1997.

[61] O. Heaviside, in *Electromagnetic Theory*, London, Benn, 1893, p. 399.

[62] J. J. Thomson, in *Notes on Recent Researches in Electricity and Magnetism*, Oxford, Clarendon, 1893, pp. 344-347.

[63] J. Larmor, "Electric vibrations in condensing systems," *Proc. London Math Soc.,* vol. 26, p. 119, 1894.

[64] L. Rayleigh, "On the passage of electric waves through tubes, or the vibrations of dielectric cylinders," *Phil. Mag.,* vol. 43, pp. 125-132, 1897.

[65] D. J. Griffiths, "Electromagnetic Waves," in *Introduction to Electrodynamics, 3rd Edition*, Prentice Hall, 1999, pp. 405-408.

[66] D. Hondros and P. Debye, "Elektromagnetische Wellen an dielektrischen Draehten," *Ann. Physik,* vol. 32, p. 465, 1910.

[67] E. A. J. Marcatili, "Dielectric rectangular waveguide and directional coupler for integrated optics," *Bell Syst. Tech. J.,* vol. 48, p. 2071–2102, 1969.

[68] J. Heebner, R. Grover and T. Ibrahim, "Optical Dielectric Waveguides - Coupling," in *Optical Microreonators: Theory, Fabrication and Applications*, London, Springer, 2008, pp. 26-35.

[69] B. Little, S. Chu, H. Haus, J. Foresi and J.-P. Laine, "Microring resonator channel dropping filters," *Journal of Lightwave Technology,* vol. 15, no. 6, pp. 998-1005, 1997.

[70] A. Yariv, "Universal relations for coupling of optical power between microresonators and dielectric waveguides," *Electronics Letters,* vol. 36, no. 4, pp. 321-322, 2000.

[71] J. Heebner, R. Grover and T. Ibrahim, Optical Microresonators: Theory, Fabrication and Applications, Springer, 2008.

[72] L. Zhang, M. Song, T. Wu, L. Zou, R. G. Beausoleil and A. E. Willner, "Embedded ring resonators for microphotonic applications," *Optics Letters,* vol. 33, no. 17, pp. 1978-1980, 2008.

[73] S. V. Boriskina, I. Chremmos, O. Schwelb and N. Uzunoglu, Photonic Molecules and Spectral Engineering, Springer, 2010.

[74] Y. Hu, X. Xiao, H. Xu, X. Li, K. Xiong, Z. Li, T. Chu, Y. Yu and J. Yu, "High-speed silicon modulator based on cascaded microring resonators," *Optics Express,* vol. 20, no. 14, pp. 15079-15085, 2012.

[75] X. Zhou, L. Zhang, A. M. Armani, R. G. Beausoleil, A. E. Willner and W. Pang, "Power enhancement and phase regimes in embedded microring resonators in analogy with electromagnetically induced transparency," *Optics Express,* vol. 21, no. 17, pp. 20179-20186, 2013.

[76] L. A. M. Barea, F. Vallini, G. F. M. d. Rezende and N. C. Frateschi, "Spectral Engineering With CMOS Compatible SOI Photonic Molecules," *IEEE Photonics Journal,* vol. 5, no. 6, 2013.

[77] L. A. M. Barea, F. Vallini, P. F. Jarschel and N. C. Frateschi, "Silicon technology compatible photonic molecules for," *Applied Physics Letters,* vol. 103, no. 20, p. 201102, 2013.

[78] M. C. M. M. Souza, L. A. M. Barea, F. Vallini, G. F. M. Rezende, G. S. Wiederhecker and N. C. Frateschi, "Embedded coupled microrings with high-finesse and close-spaced resonances for optical signal processing," *Optics Express,* vol. 22, no. 9, pp. 10430-10438, 2014.

[79] M. Smit and G. A. Acket, "Al2O3 films for integrated optics," *Thin Solid Films,* vol. 38, no. 2, pp. 171-181, 1986.

[80] J. Schmidt, F. Werner, B. Veith-Wolf, D. Zielke, R. Bock, V. Tiba, P. Poodt, F. Roozeboom, T. A. Li, A. Cuevas and R. Brendel, "Industrially Relevant Al2O3 Deposition Techniques for the Surface Passivation of Si Solar Cells," in *EU PVSEC*, Valencia, 2010.

[81] K. Worhoff, J. D. B. Bradley, F. Ay, D. Geskus, T. P. Blauwendraat and M. Pollnau, "Reliable Low-Cost Fabrication of Low-Loss Al2O3:Er3+ Waveguides

With 5.4-dB Optical Gain," *IEEE Journal of Quantum Electronics ,* vol. 45, no. 5, pp. 454-461, 2009.

[82] Q.-Y. Tong and U. Gösele, SemiConductor Wafer Bonding: Science and Technology, Wiley-Interscience, 1998.

[83] V. R. Manfrinato, J. Wen, L. Zhang, Y. Yang, R. G. Hobbs, B. Baker, D. Su, D. Zakharov, N. J. Zaluzec, D. J. Miller, E. A. Stach and K. K. Berggren, "Determining the Resolution Limits of Electron-Beam Lithography: Direct Measurement of the Point-Spread Function," *Nano Letters,* vol. 14, no. 8, pp. 4406-4412, 2014.

[84] L. A. M. Barea and N. C. Frateschi, "Moléculas Fotônicas para aplicações em Engenharia Espectral e Processamento de Sinais Ópticos," UNICAMP, Campinas, 2014.

[85] M. Rothschild, "Projection optical lithography," *Materials Today,* vol. 8, no. 2, pp. 18-24, 2005.

[86] A. Arbabi and L. L. Goddard, "Dynamics of self-heating in microring resonators," *IEEE Photonics Journal,* vol. 4, no. 5, p. 1702–1711, 2012.

[87] M. C. M. M. Souza, G. F. M. Rezende, L. A. M. Barea, A. A. G. v. Zuben, G. S. Wiederhecker and N. C. Frateschi, "Spectral engineering with coupled microcavities: active control of resonant mode-splitting," *Optics Letters,* vol. 40, no. 14, pp. 3332-3335, 2015.

[88] P. G. Kik and A. Polman, "Cooperative upconversion as the gain-limiting factor in Er doped miniature Al2O3 optical," *Journal of Applied Physics,* vol. 93, no. 9, pp. 5008-5012, 2003.

[89] J. D. B. Bradley and E. S. Hosseini, "Monolithic erbium- and ytterbium-doped microring lasers on silicon chips," *Optics Express,* vol. 22, no. 10, pp. 12226-12237, 2014.

[90] Y. A. Vlasov and S. J. McNab, "Losses in single-mode silicon-on-insulator strip waveguides and bends," *Optics Express,* vol. 12, no. 8, p. 1622–1631, 2004.

[91] S. Sze and K. K. Ng, Physics of Semiconductor Devices, Wiley, 2006.

[92] C. L. A., C. S. W. and M. L. Masanovic, Diode lasers and photonic integrated circuits, Wiley, 2012.

[93] M. Ohkubo, T. Ijichi, A. Iketani and T. Kikuta, "Aluminium free InGaAs/GaAs/InGaAsP/InGaP GRINSCH SL-SQW lasers at 0.98um," *Electronics Letters,* vol. 28, no. 12, pp. 1149-1150, 1992.

[94] E. Yablonovitch and E. Kane, "Reduction of lasing threshold current density by the lowering of valence band effective mass," *Journal of Lightwave Technology,* vol. 4, no. 5, pp. 504-506, 1986.

[95] G. Zhang, M. Pessa and D. Awn, "Gain Characteristics of Strained-Layer InGaAs/GaAs Quantum Well Lasers," *Physica Status Solidi (b),* vol. 176, pp. K75-K79, 1993.